University Degree in Aerospace Engineering
Academic Year 2017-2018

BACHELOR THESIS

FLUIDIC SIMULATION OF A MAGNETO-MECHANICAL ACTIVE SURFACE

UNIVERSIDAD CARLOS III DE MADRID

Eva María Cancela Rodríguez

Tutor: Andrés Campos Galera

Madrid, 19th June 2018

Acknowledgements

Once the bachelor thesis has been finished I would like to thank several people for their support throughout these years.

First of all, I would like to thank my tutor Andrés Campos for giving me the chance of writing this project and always helping me when needed.

Thinking on my years on this university, there is plenty of people which come to my mind: classmates, professors, colleagues from my internship, flatmates, all the people from the FAM… They all have made me grow up and they were my family during my stay in Madrid. I have to say a huge 'THANKS' to Crispis and Cris, these girls are the best friends anyone could ask for.

Last two years I have had the chance of participating on two exchange programs. Firstly, I could not be more thankful for all the people that I have met during my two semesters in Milano. You all made of this time an awesome experience and one of the best years so far. Finally, thanks to everyone I have met in Brisbane, you have made, from a short period, such a huge and intense adventure.

Besides the university, I obviously have to mention my friends from Galicia, they have really taught me that the distance means nothing and that real friendships are those which remain along the years even after months without talking. Also, going back on the time, I really appreciate the support of my professors from my high school who really encouraged me to fight for what I really want, specially my Physics professor.

And as I like to keep the best for the end, I really have to thank my parents, Manuel and Angeles, and my sister, Ana. Thank you for always being there, thanks for the admirable and incessant support and love, thank you for always understanding me and never letting me give up. You have always known how to guide me and I could not be more proud of the family I have. I love you.

Thanks a lot

Contents

List of figures

List of tables

1. Abstract

The aim of this project is to perform a fist analysis of artificial cilia, a material recently introduced in the engineering field. This material, which is a reproduction of cilia filament present in the nature, has special properties when subjected to the influence of a magnetic field. This properties may have many applications in different engineering fields. The purpose of this study is to analyse how this material behaves when imposing a fluid flow around it under defined properties. Different geometries and element configurations will be assessed in order to find the design that optimizes the fluid performance in terms of mixing optimization.

The project is divided into two range of scales. On one hand, elements of the order of micrometres are analysed. On the other hand, models in millimetric scale are analysed. Along this report a detailed explanation of the simulation procedure and the results obtained is show. The choices are always made in terms of velocity (represented by the Reynolds number) and, therefore, the results are shown in terms of this parameters. A final conclusion states the design which optimizes the fluid behaviour, for both cases.

2. State of art

2.1 Introduction

Natural cilia is present in many organisms and it can only be appreciated at microscopic level. Its geometry might be defined as small flexible rods that may move following a specific pattern. They cover large surfaces in contact with any fluid environment. Due to the combined movement of all these minuscule structures, an induced fluid flow is created. This procedure can be observed in different contexts, the human body is a very suitable example. As shown in the images below (Figures 1-2), cilia is present on intestine walls, fallopian tubes, lung walls, spermatozoa, etc.

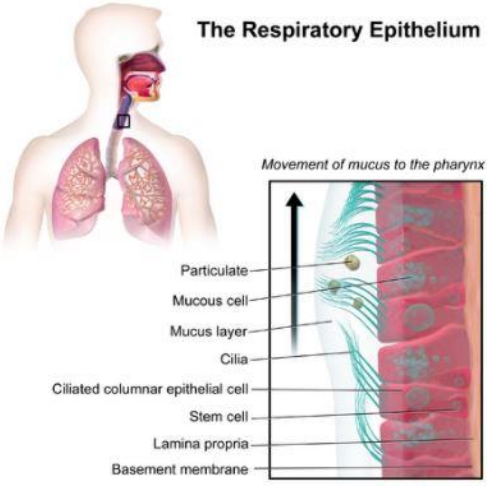

Figure 1.Respiratory system functioning.

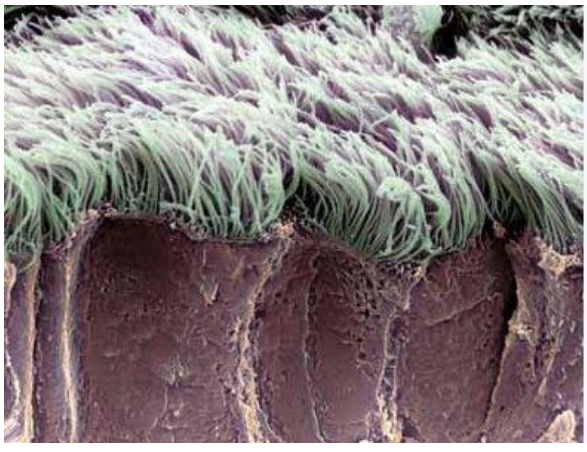

Figure 2.Fallopian tube wall

As it previously mentioned, those small filaments, when combined, can effectively produce a fluid stream. For this reason, this bio-inspired model is being used in order to fabricate magneto/electro-mechanical active surfaces, i.e. Surfaces that induce a fluid movement in volumes as micro-reactors chambers, microfluidic channels, microchips heat dissipaters, etc. Nowadays, artificial cilia is becoming very relevant on the development of lab-on-chip devices where fluid need to be transported through microchannels, mixed in less time as possible and other kinds of fluid manipulation.

The main objective of this project is to analyse the geometry of this manufactured material under different fluid flow rates, evaluating how relevant parameters, such as velocity and pressure given to the fluid, vary as a function of different inputs. Other relevant topics such as the regulatory framework and the socio-economic environment are included in coming sections (section 6).

2.2 Theoretical background

Cilia rods, which have a typical length between 1 μm and hundreds of micrometres, are capable of either undulating or rotational movement. In the case of forward and backward motion, when analysing each individual cilia filament, it can be seen that it follows an asymmetric established movement as it can be seen in Figure 3.

Not all the filaments move simultaneous; crosswise cilia move all at a time however, lengthwise rods move in a sequential way. That is the so called Metachronous rhythm. [1]

Back and forward motions are also called effective and recovery stroke, respectively (figure 3). It is a three dimensional movement in which the cilium moves the fluid parallel to the surface where it is attached. Fluid movement forms 90^0 with the cilium longitudinal axis. During the back motion, the cilia goes against the water producing, therefore, the body to move ahead while the liquid is directed rearwards. When the forward motion is happening, as it name indicates, the filaments recover their original position without any impediment.

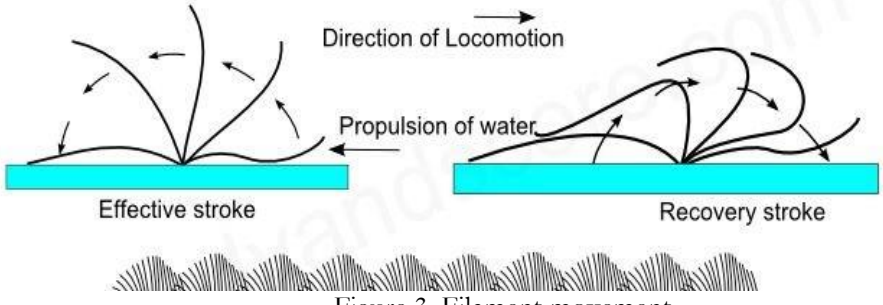

Figure 3. Filament movement

As mentioned in the previous point, natural cilia has been recently brought to the artificial field and it is mainly used to generate fluid flow in lab-on-a-chip devices. Artificial cilia are mechanical actuators that simulate the movement of these natural filaments.

The main ways of activating artificial cilia are light, electric fields and magnetic fields. During this experiment, it will be simulated the behaviour of a cilium rod under the presence of fluid flow. It is intended to capture the interaction of the material (by defining all its properties) with the performance of the fluid (in terms of velocity and pressure). Focusing on the actuation of a single filament of cilia, it is possible to analyse the orientation and displacement in terms of the applied magnetic field. Powerful magnetic dipole moments are induced by a magnetic field. Dipoles are parallel aligned in the direction of the dipole and, therefore, the filaments also adjust aligned with the field. If the actuated magnetic field is moderately pivoted, so will do the solid filament. If the rotation velocity is increased above a defined limit, the cilium rod will bend due to hydrodynamic fluid friction. [2]

Briefly going through electromagnetism, it is defined as a branch of physics that studies the interaction between electric and magnetic phenomena and unifies them in a single theory firstly formulated by James Clerk Maxwell. Basically, it states that every electric charge in motion generates, in addition to an electric field, a magnetic field.

In this field, it is remarkable the relevance of Biot–Savart law, [3], which describes the magnetic field generated by a stationary electric current. It relates the magnetic field to the magnitude, direction, length, and proximity of the electric current with the following equation:

$$B(r_2) = \frac{\mu_0}{4\,\pi} I_1 \oint_1 \frac{dl_1 \times (r_2 - r_1)}{|r_2 - r_1|^3}$$

It represents the magnetic density due to the electric intensity I_1 of one element acting on each length differential of the other, as it can be observed in the figure below. [4]

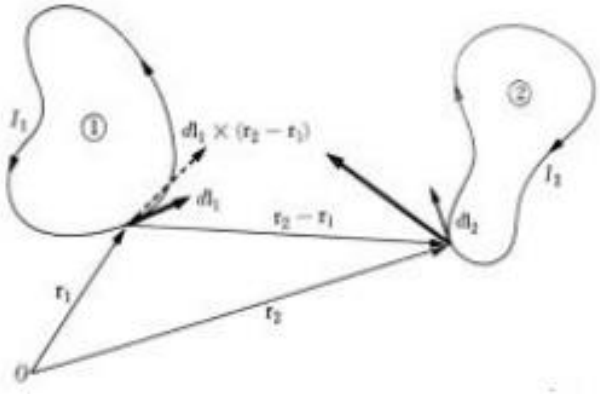

Figure 4. Electromagnetic interaction

3. Experimental methods and simulation procedure

Simulation

In order to analyse the interaction of the fluid with the magneto-mechanical active surface (MMAS), a FEM simulation was performed. This task was carried out with Ansys Fluent software.

Ansys Fluent is a computational fluid dynamics (CFD) tool which helps to easily reproduce complex models optimizing, therefore, different phases of product development.

The simulation process consists in, firstly, modelling the geometry of the problem. This geometry might be lately modified in order to improve different properties. Subsequently, a mesh has to be created. The more refined is the mesh, the more accurate will be the results. However, very refined meshes lead to long processing and computation times. One of the most challenging phases of the simulation was to obtain sufficiently accurate results but optimizing the computation time so that a higher number of studies could be made. Finally, the setup phase is carried out and all the different parameters and materials are configured. Once those stages are completed, a wide range of results can be obtained.

During this process a balance between processing time and accurate results was searched. In order to find an optimal process different models were tried.

The starting point was a 2D model representing a silicone-nanomagnetite beam clamped on the lower wall of a rectangular channel, as shown in Figure 5. Aluminium is the chosen material for the channel walls whereas the beam is made of the mentioned polymeric nanocomposite.

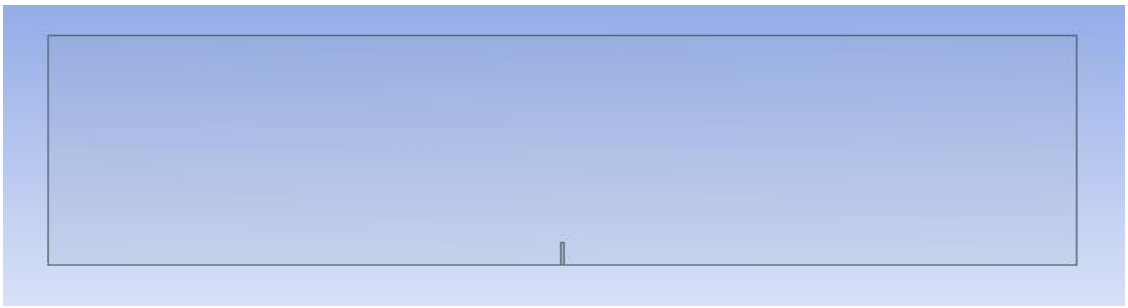

Figure 5. 2D channel

Water was used as working fluid and the input variable at the entrance of the channel was the fluid velocity. Under these conditions, the evolution of the fluid, modifying the input magnitude, was analysed along the channel. Obtaining, therefore, different distributions of velocity and pressure. Walls were placed far enough from the analysed rod in order to avoid their influence in the evaluated fluid.

Different geometries were studied by the performance of a parametric study of the rectangular geometry in order to obtain the best possible combination between length and thickness. The aim is to maximize the pressure and velocity obtained in the fluid withstanding the same input energy.

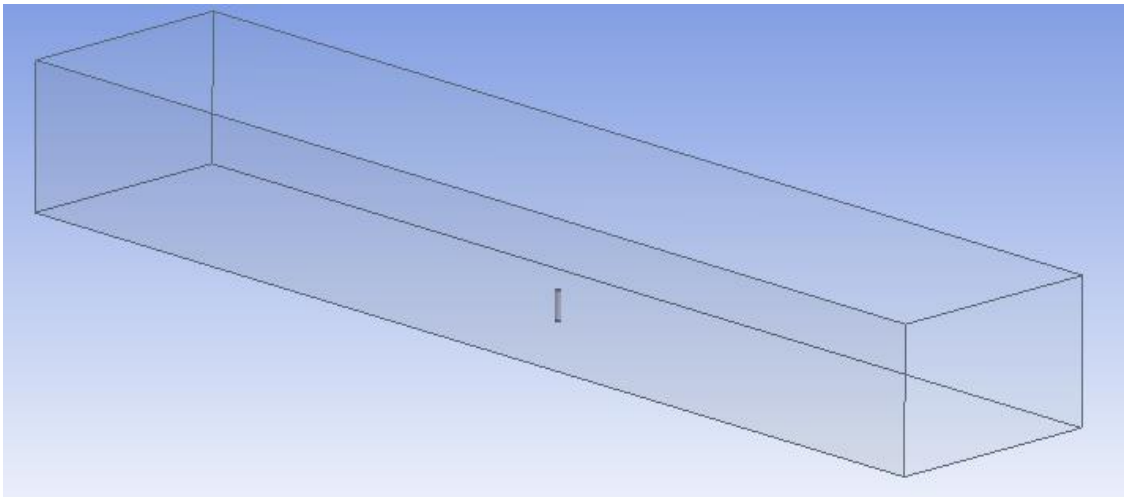

Figure 6. 3D channel

Afterwards, the previous model was moved to the next level implementing a 3D channel as shown in the figure above. Again the varying input was the velocity, and the fluid performance was analysed. As in the previous case, the most efficient geometry configuration was searched.

Furthermore, for the 3D simulation additional parameters were assessed and optimized. Apart from dealing with variables such as the height and the section shape, other relevant parameters such as roughness, separation between elements (in the case of a configuration with many filaments) and corner's shape were also evaluated.

Fluent is a simulation software which allows to analyse the behaviour of a fluid in a defined environment and under certain conditions. Unfortunately, it does not allow to visualize the displacements produced due to fluid flow. Therefore, only the fluid behaviour will be evaluated.

3.1 FEM simulation

A well-known numerical method used to solve engineering problems is the finite element method (FEM). In general, partial differential equations are used to express the laws of physics that govern space and time dependent problems. When a case reaches certain degree of complexity, these differential equations cannot be solved using analytical methods. However, they can be approximated using discretization methods up to the point in which they can be solved using numerical methods. The finite element method is in charge of compute this approximation. The FEM problem formulation is seen as a system of algebraic equations which provides approximate solutions for a discrete number of points within a region.

The FEM technique is used for splitting the whole problem into simpler and minor parts known as finite elements. These simplified equations are next put together forming a more complex and larger equation system that represents the whole problem. Thus, FEM approximates the solution minimizing an associated error function. This error due to the adoption of the numerical model rather than the mathematical one, is known as truncation error. It is, therefore, denoted as the divergence of the solution from the mathematical model. The desired objective is that the numerical solutions converge to the one obtained with the mathematical model. That is, for a stable model, the truncation error tends to zero as so does the element size. This fact can be also determined by the order of accuracy; if it is positive, the achieved result is coherent. [5] [6]

As mentioned above, the full domain is separated into more elemental sections in order to simplify calculations. This process helps to get a more meticulous description of the complex geometry, by combining different material characteristics, it makes easier the representation of the whole solution and allow to analyse local effects.

FEM is usually explained as a special case of Galerkin method [7]. This technique removes, from the partial differential equations, the spatial derivatives. In the case of steady cases, it approaches the differential equations by the local use of a group of algebraic eqs. For the case of transient solutions, ordinary differential equations are used. Algebraic equations, coming from steady state problems, are determined through numerical linear algebra methods. At the same time, ordinary differential equations resulting from transient states come out by numerical integration with techniques such as Euler's method or the Runge-Kutta method. [8]

After this first phase, all the element equations are collected into an overall system through which the problem is passed from local nodes to global nodes. The change of coordinates is applied to each variable by FEM software through coordinate data generated from the subdomains.

The practical application of the FEM, used in the engineering field, is called finite element analysis (FEA). FEA uses a software program coded with FEM algorithm. This process performs the previously discussed divisions by generating a mesh. The aim of this analysis is to decrease the number of experimental tests and prototypes needed during the design process and so, optimizing time, costs and resources.

FEA software is governed by different conservation laws, in the simulation of artificial cilia only mechanics, fluids and magnetism laws would be used. In the structural mechanics field, the laws for the balance of forces and the constitutive relations that relate the stresses to strains describe the physics of the problem. In fluid flow, heat transfer, and mass transfer, the descriptions are based on the laws for conservation of momentum, mass, and energy. The precise form of the dissipation and diffusion is given by a constitutive relation, such as the viscous stress for Newtonian fluids, Fourier's law of thermal conduction, and Fick's law of diffusion. In addition, the relation between the magnetic field and electric currents is modelled using Ampere's law. Maxwell's equations introduce the dynamics of the problem, as it can be the induction on an electric field due to a time-varying magnetic field. [5] [6]

In this project, the FEA was performed with the computational fluid dynamics (CFD) tool Ansys Fluent. The procedure followed with this software will be explained in coming sections.

Recalling the history of the FEM, it is complicated to specify a date for its invention. It originally appeared in the civil and aeronautical field, as method to deal with complex elasticity and structural analysis problems. Its first success is dated on 1940 by A. Hrennikoff and R. Courant. Although Courant identified a large range of possible applications, this practice was not used in the structural mechanics field until several decades after. [9]

Ioannis Argyris and Leonard Oganesyan were also relevant characters in this environment. The last one helped introducing a practical application of this method in the URSS. Also, in China (1950s-60s), it is remarkable K. Feng who proposed the finite difference method based on variation principle. [10]

All those pioneers shared the common characteristic of including a mesh discretization of a continuous domain into several discrete subdomains, called elements.

FEM started being really accepted in the 1960s and 1970s thanks to open source finite element software programs. Also NASA promoted the original version of NASTRAN, and UC Berkeley made the finite element program SAP IV widely available.

Since those dates, this method has become a relevant component in any design process. Nowadays it is worldwide used in many different industries mostly of the engineering field.

3.1.2 2D Model

For the modelling in two dimensions, two optimization processes were performed, one for cilia with sizes in the range of micrometres, which will be called microfilament, and another for cilia sizes in the range of millimetres called as macrofilament.

For the microfilament simulation, the influence of the rod length and the thickness was evaluated. In order to cover a wide range of possibilities, a sweep with different values for those parameters was carried out. The length of the filament was varied between 15 and 100 μm. Simultaneously, its thickness was evaluated ranging from a maximum value of 20 μm to a lowest value of 1 μm. Every single combination of length and thickness was subjected to a collection of initial velocities varying between 1 and 10 m/s. All the tests were carried out in a channel as the one shown in figure 5. Its dimensions are 4200 μm of longitude and an altitude of 1000 μm. The table below sums up all the analysed combinations between thickness and length.

Microfilament (channel dimensions: longitude = 4200 μm and height=1000 μm)				
Analysed filament thickness/height	**15 μm**	**50 μm**	**80 μm**	**100 μm**
1 μm	1x15	1x50	1x80	1x100
5 μm	5x15	5x50	5x80	5x100
10 μm	10x15	10x50	10x80	10x100
20 μm	20x15	20x50	20x80	20x100

Table 1. Analysed, height (columns) and thickness (rows), dimensions for the microfilament.

The same procedure was repeated for the macrofilment, the length was varied between 100 and 15 mm and so did the thickness among 1 and 20 mm. Again, the model was evaluated under the influence of a range of velocities from 1 to 10 m/s. The working channel had a longitude of 4200 mm and its height was 1000 mm.

Microfilament (channel dimensions: longitude = 4200 mm and height=1000 mm)				
Analysed filament thickness/height	**15 mm**	**50mm**	**80mm**	**100mm**
1mm	1x15	1x50	1x80	1x100
5mm	5x15	5x50	5x80	5x100
10mm	10x15	10x50	10x80	10x100
20mm	20x15	20x50	20x80	20x100

Table 2. Analysed, height (columns) and thickness (rows), dimensions for the macrofilament.

The aim of this stage was finding out which are the dimensions and the input velocity that maximize the velocity and the pressure gradient of the fluid inside the channel. For this purpose, data from every simulation was collected and represented. Two size scales, micro- and macro-filaments, were simulated in order to obtain the behaviour of photolithography cilia (micrometre scale [table 1]) and mould pouring cilia (millimetre scale [table 2]). Maximum Reynolds number (analogously to the velocity) was analysed and compared with the input one. Likewise, the pressure gradient was evaluated.

For both cases the working fluid was liquid water. The rod was made of magnetic artificial cilia, using a density of 1003 kg/m^3, magnetic relative permeability of 50, specific heat equal to 1.46 kJ/KgK and a thermal conductivity of 0.15 W/mK. [11]

3.1.3 3D Model

For the 3D simulation, three procedures were approached. In the first section, two geometric parameters were modified. Individual cilia microfilaments were tested varying their length and their apothem. Afterwards, nine microfilaments were arranged together and the separation among them was analysed. A more precise explanation will be given in the following paragraphs.

In the second procedure, the design is changed into a rectangular prism where three variables are now modified and evaluated. Again, the most optimal design was chosen and then brought to a set of nine equal filaments. As in the previous case, the distances between columns was optimized. In section 3.1.3.2 the procedure will explained in more detail.

Lastly, in the third section, the best design from the second modelling was reshaped by adding artificial roughness.

3.1.3.1 Columns

The most efficient design from the 2D simulation was used as starting point for the 3D simulation. This simulation was performed in a channel with rectangular section. The channel measurements are 500 μm high, a crosswise length of 800 μm and a longitude of 4000 μm.

In order to find the most adequate design, different section geometries were approached: circular, triangular, squared, hexagonal and octagonal. The apothem (radius in the case of the circle) and the length of the filament were the parameters to be optimized.

Regarding the most efficient results from the 2D simulation, the length was varied between 80 and 100 mm and the apothem (or radius) between 5 and 10 μm. Every single combination of apothem and length was performed and numerous simulations were carried out, sweeping the input velocity between 5 and 10 m/s. This range of velocities was chosen because they lay on the turbulent region or in the transition for laminar to turbulent. The image on the right (Figure 7) shows the geometry of a single rod with hexagonal section and another rod with an octagonal section.

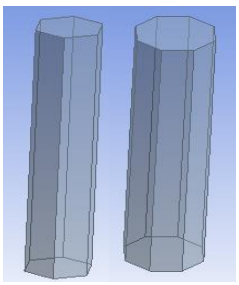

Figure 7. Rod designs

Table 3 is added to summarize and clarify the previous explanation.

Analysed section shapes and dimensions (Channel dimensions: height=500 μm, width=800 μm and longitude=4000 μm)			
Section shape	**Analysed filament radius(or apothem)/height**	**80 μm**	**100 μm**
Circular	**10 μm**	10x80	10x100
	20 μm	20x80	20x100
Triangular	**10 μm**	10x80	10x100
	20 μm	20x80	20x100
Squared	**10 μm**	10x80	10x100
	20 μm	20x80	20x100
Hexagonal	**10 μm**	10x80	10x100
	20 μm	20x80	20x100
Octagonal	**10 μm**	10x80	10x100
	20 μm	20x80	20x100

Table 3. Analysed column dimensions and section shapes

The most effective design, i.e. the rod geometry that produces the highest increment in the velocity magnitude and the largest pressure gradient, was chosen for the next step of the optimization process.

In this second stage, a collection of nine microfilaments are combined together. As previously mentioned, their geometry was selected from the most optimal design in the preceding procedure. The followed distribution is displayed in figure 8.

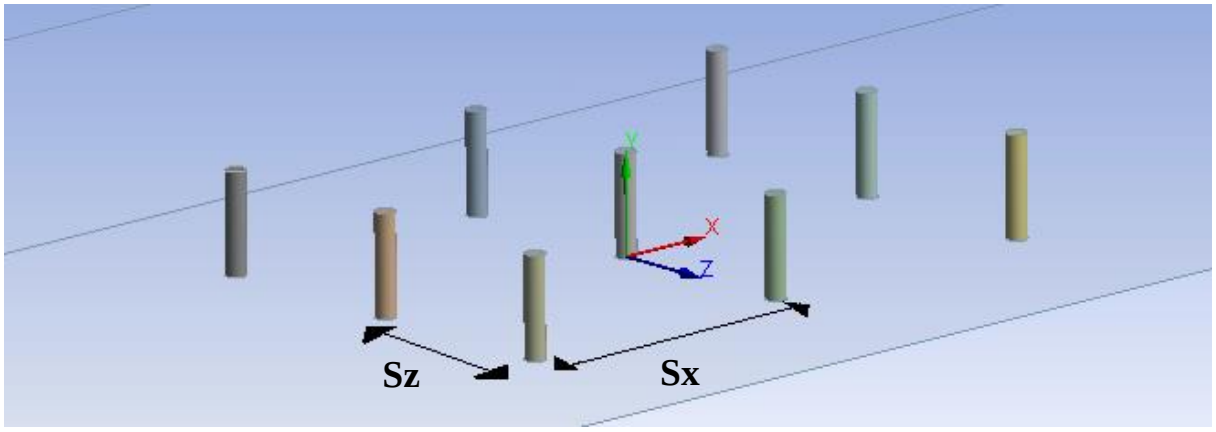

Figure 8. 3D filaments distribution

The aim of this simulation stage is to find the value for Sx and Sz that optimizes the results. Sx and Sz are the separations between filaments in the x and z directions, respectively.

The above represented arrangement was tested, sweeping Sx in a range of values between 100 and 300 micrometres and Sz between 100 and 200 micrometres. The analysed spectrum for Sz is smaller due to space limitations inside the channel.

Sz/Sx	100 µm	150 µm	200 µm	250 µm	300 µm
100 µm	100x100	100x150	100x200	100x250	100x300
150 µm	150x100	150x150	150x200	150x250	150x300
200 µm	200x100	200x150	200x200	200x250	200x300

Table 4. Combinations of filament separation that were analysed.

Every possible combination between Sz and Sx was evaluated (Table 4). As in the previous cases, the model which obtained the best performance in terms of velocity (Reynolds number) and pressure gradient was chosen.

The equation used to compute the Reynold number [12] is the following:

$$Re = \frac{v_s \, D_H}{\nu}$$

Where v_s is the velocity of the fluid for every case (in m/s), ν is the kinematic viscosity (1,007e-6 m/s) and D_H is the hydraulic diameter for channels with non-squared section (in meters). It is computed as follows:

$$D_H = \frac{4\,Area}{Perimeter} = 6.15\ 10^{-4}\ m$$

Area and perimeter are computed with the values given at the beginning of this section.

3.1.3.2 Flaps

From the previous part, where cilia filaments were analysed, the design is brought to a more complex level. For the preceding testing, just two parameters were varied in order to optimize the design, apothem of the section geometry and length of the 'column'. In the actual case, the geometry is transformed from '2D elements' to what it is called flaps (Shown on the image on the right). In this new assessed structure, three parameters were modified in order to obtain the most optimal design: Length, thickness and width of the flaps.

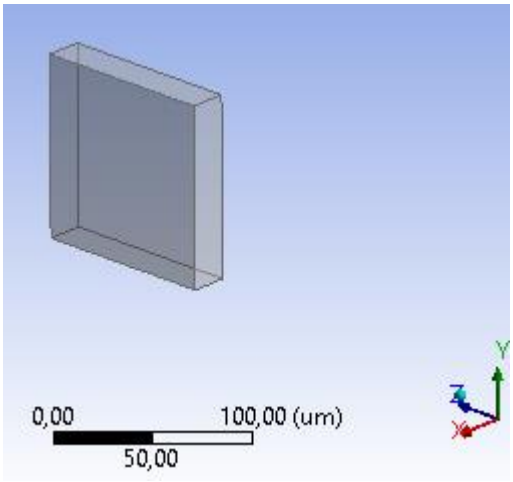

Figure 9. Flap design.

On this section, as in 3.1.2, a distinction between microflaps and macroflaps was made. Microflaps results will be used to make a comparison with all the previous 3D simulations, since they are of the same order of magnitude. On the other hand, macroflaps will be later compared with the results coming from the experimental data.

For both cases, as explained at the beginning of this section the followed procedure was the same. Firstly, one single element was analysed varying its parameters. From this analysis, the best design was chosen and it was put together with nine equal element. The second purpose was to find the best longitudinal and crosswise separation distance between elements.

3.1.3.2.1 Microflaps

As mentioned, this simulation was carried also in order to make a comparison with the columns previously simulated. For this case, in order to avoid walls influence, the channel measurements are 800 μm high, a crosswise length of 2400 μm and a longitude of 6000 μm.

The starting point was a flap with dimensions 100x100x20 μm (height x width x thickness), since those are the dimensions that allow manufacturing by photolithography [table 1]. Three different values were consider for each of the parameters (height, width and thickness), in order to have a general idea of the behaviour of the fluid due to every modification. Now, performing one simulation with every combination would not be approachable due to a lack of time for such an elevated number of combinations. For this reason nine different models, representing nine different combinations of height, width and thickness, were assessed and subjected to various velocities.

Starting from the original model, two thicknesses of 30 and 10 μm were evaluated. Under the primary condition, the height was changed to 200 and to 50 μm. The width was also replaced for 200 and 50 μm.

Table 5 represents all the different assessed combinations for the dimensions of the flap.

height x width x thickness [μm]			
Varying height	Varying width	Varying thickness	Varying width & height
50x100x20	100x50x20	100x100x10	50x50x20
100x100x20	100x100x20	100x100x20	100x100x20
200x100x20	100x200x20	100x100x30	200x200x20

Table 5. Dimension combinations that were simulated.

From the results of the preceding testing, the most optimal design was selected and placed together with other nine equal element inside the channel. Next step was to figure out which were the separations between flaps that obtain a better performance. The separation distances in the x and z axis are called Sx and Sz, respectively. They are shown in figure 8 and table 6.

Sz/Sx	**50 μm**	**100 μm**	**200 μm**
50 μm	50x50	50x100	50x200
100 μm	100x50	100x100	100x200
200 μm	200x50	200x100	200x200

Table 6. Analysed separations between flaps.

All the flaps designed have squared corners forming 90º. The last part of this section is to change the shape of the corners, making them rounded, and analyse the performance of the fluid under these changes. Two testing were performed with two different corner radius. Firstly, the radius length was half the flap width of the chosen design. The second length selected was one quarter of the flap width.

Reynolds number, variable used to analyse the fluid behaviour, was already defined in the previous section. In order to perform a proper comparison, the ratio between maximum Reynold achievable and inlet Reynolds number will be displayed.

3.1.3.2.2 Macroflaps

The procedure followed in this section is similar to the preceding one. However, the working channel used for this case has a semi-circular section in order to allow a more realistic comparison with the experimental results (carried out in a cylindrical channel, see section 6.4 future works). As for the experimental simulation, the channel section cannot be completely circular since a flat base is needed to place the flaps. The channel dimensions for this case are a radius of 100mm and a longitude of 3000mm. The previously stated formula for the Reynolds number has to be used again with the hydraulic diameter (D_H) since the section is not completely circular.

As before, different combinations of height, width and thickness were firstly analysed for a single flap. All the simulated arrangements are summed up in the following table.

height x width x thickness [mm]		
Varying height	Varying width	Varying thickness
2.5x15x0.5	5x10x0.5	5x15x0.25
5x15x0.5	5x15x0.5	5x15x0.5
10x15x0.5	5x120x0.5	5x15x1

Table 7. Dimension combinations that were simulated.

From the previous simulations, the combination giving a higher performance was chosen to simulate together with other eight identical macroflaps. The objective of this second step was to find the most suitable separation between

elements which optimizes the fluid performance. For this case, the dimensions of the channel section were augmented in order to avoid undesirable effects coming from the wall. This modification did not affect the analysis since the parameter evaluated is the ratio between maximum Reynolds number and inlet Reynolds number. The updated dimension for this case is a radius of 300mm, the length remained unchanged. All the separations assessed are displayed in table 8.

Sz/Sx	**10mm**	**20mm**	**30mm**
2.5mm	2.5x10	2.5x20	2.5x30
5mm	5x10	5x20	5x30
10mm	10x10	10x20	10x30

Table 8. Analysed separations between flaps.

Finally, after selecting the most optimal design together with the most optimal elements separation, the corners shape was evaluated. The initial shape formed 90º nevertheless, two more options were assessed. As in the previous case, simulations with rounded shape for the corner were also performed. One selection was using a radius equal to half of the flap width, the other alternative used a radius equal to quarter the flap width.

3.1.3.3 Roughness

The last step of the entire simulation process was to add artificial roughness to the flap surface. The aim was to, by using always the same amount of material, add different types of surface roughness. Figure 10 is added to clarify the proposed idea.

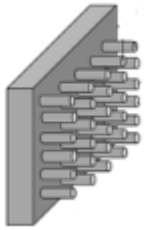

Figure 10. Roughness distribution.

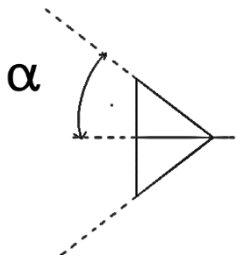

Figure 11. Side view of a conical element.

Mainly, two different types were evaluated: conical elements and cylindrical elements. Figure 10 represents the case of a cylindrical structure. Regarding conical elements, two different values for α were analysed as it can be seen in figure 11: α=30º and α=40º.

For every proposed configuration, an analysis varying the dimensions of every element was performed. Again, a distinction between microflap and macroflap was made. The flap dimensions used were selected from previous computations, that is, the ones giving the best performance regarding earlier analysis and simulations.

Regarding the microflap, for conical elements with an angle of 30º, the radius ranged from 2.1um to 4um. Using an angle of 45º, the radius varied between 2.5 µm and 5 µm. The relationship between the height of the cone and it radius can be easily obtained with trigonometry. For 45º elements, the radius equals the height. For the case of 30º, $r = \frac{\sqrt{3}}{3} h$, where h represents the height and r is the radius. For the cylindrical case, the altitude of the cylinder was set to twice the radius value. The radius values ranged from 1.5 µm to 2.5 µm.

As it was previously mentioned, the aim is to find out which is the configuration that optimizes the results by using always the same amount of material. With this purpose, the weight of the added material had to be conserved for every simulation. The density times the volume equals the weight times the number of elements, ($\rho = \frac{weight}{volume} * number\ of\ elements$). Regarding the previous equation and knowing that the weight and the density must be conserved, for each selected radius (variation in volume), the number of surface elements must be also modified. The separation between elements was changed in a uniform ways, trying always to optimize the space on the flap surface. A remarkable issue arisen during this simulation is the fact that, the academic version of Fluent, only allows the use of a limited number of 50 bodies. This restriction had to be taken in to account and it had forced the use of bigger elements.

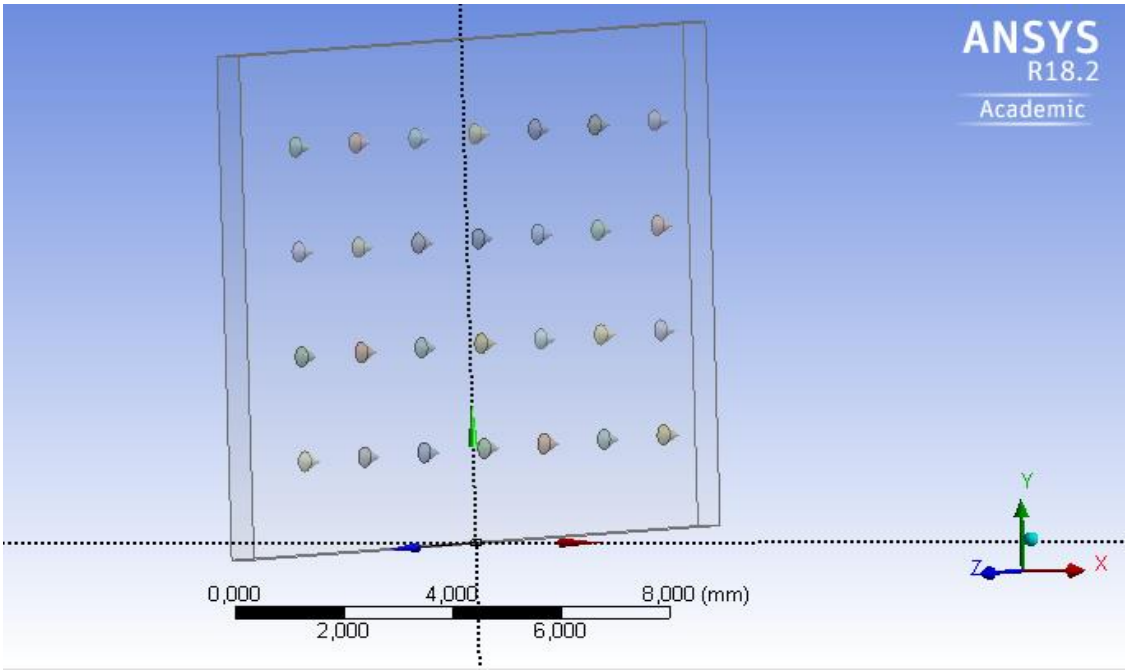

Figure 12. Roughness visual representation.

Although using different dimensions, the procedure followed for the macroflap was exactly the same. The best dimensions configuration from previous section was used. Subsequently, different configurations of roughness were assessed. The relations between the radius and the height are identical for conical and cylindrical elements. The evaluated radius values were between 0.25mm and 0.4mm for 45º cones, between 0.2mm and 0.4mm for 30º cones and ranging from 0.2 to 0.4mm for cylinders. The tables below summarise the preceding information. Sz represents the separation between elements on the z axis and Sy represent the vertical separation (y-axis).

Macroflap (Channel dimensions: radius 0.3m and length 3m														
30º					**45º**					**Cylinder**				
r [mm]	**h [mm]**	**Sz [mm]**	**Sy [mm]**	**Num. of elements**	**r [mm]**	**h [mm]**	**Sz [mm]**	**Sy [mm]**	**Num. of elements**	**r [mm]**	**h [mm]**	**Sz [mm]**	**Sy [mm]**	**Num. of elements**
0.2	0.34641	1.525	1.68	28	0.2	0.2	1.35	1	48	0.2	0.4	2.16	1.3	25
0.25	0.43301	2	1.25	15	0.25	0.25	1.4375	2.125	21	0.25	0.5	2.6	2.125	12
0.3	0.51961	2.52	2.9	8	0.3	0.3	2.52	2.05	12	0.3	0.6	2.52	2.93	8
0.4	0.69282	4.46	2.8	4	0.4	0.4	3.15	2.8	6	0.4	0.8	4.46	2.8	4

Table 9. Macroflap information.

Microflap (Channel dimensions: height 0.0005m, thickness 0.0008m and length 0.004m														
30º					**45º**					**Cylinder**				
r [um]	**h [um]**	**Sz [um]**	**Sy [um]**	**Num. of elements**	**r [um]**	**h [um]**	**Sz [um]**	**Sy [um]**	**Num. of elements**	**r [um]**	**h [um]**	**Sz [um]**	**Sy [um]**	**Num. of elements**
2.1	3.6373	15	30	40	2.5	2.5	25	20	42	1.35	2.7	39	14	44
2.5	4.33012	35	22	24	3	3	35	22	24	1.5	3	39	18	32
3	5.196152	63	18	14	3.5	3.5	45	21	15	1.75	3.5	37.2	30.42	20
3.5	6.062177	30	25	9	4	4	64	22	10	2	4	63	21.5	14
4	6.928203	62	44	6	5	5	64	50	5	2.5	5	63	36	7

Table 10. Microflap information.

A final comparison was made to find out in which face should the roughness be placed in order to get an optimal result. There were two possible options facing the inlet or facing the outlet.

3.2 Experimental methods

In order to check the reliability of the results obtained during the simulation process, some results were compared with experimental results. With this purpose a large research was performed and many scientific texts, papers and books were used.

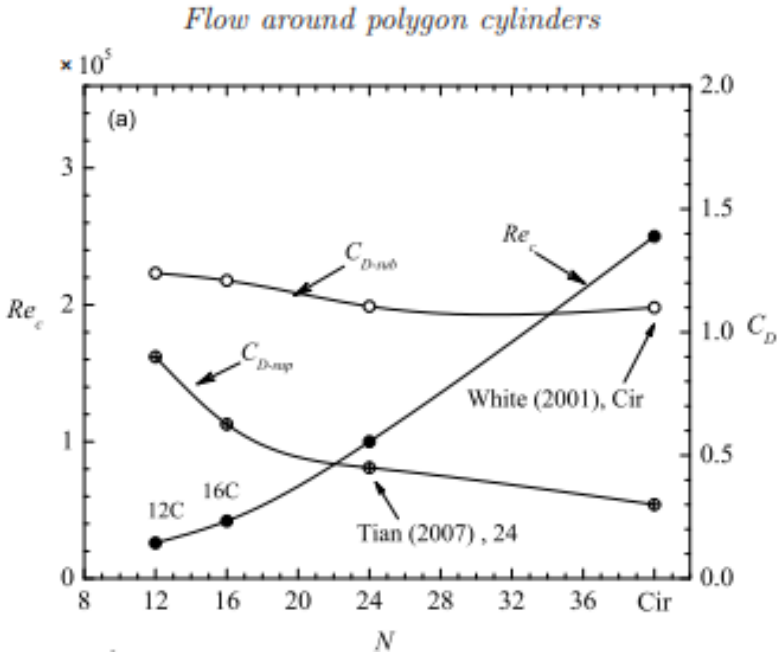

Figure 13. Influence of the polygon number of sides.

Regarding the influence of the column geometry on the flow around it, the following graph is displayed. N represents the number of sides. In Figure 13, [13], it can be observed how, as the polygon side number is increased, so it does the Re. Also the drag coefficient (Cd), which is used to quantify resistance of an object in a fluid environment [14], is represented on the same figure. It can be seen how it decreases as N is increased, i.e., the object resistance to the fluid flow is reduced and higher velocities are achieved.

The image on the right (Figure 14) shows the evaluated values for N. In the same article, the orientation of the polygon sides is assessed. Although this is out of the studied field in this report, it is remarkable that the orientation of the object (due to the location of its corners) influences the point where the boundary layer separates. Once the boundary layer is separated, Cd is severely increased, that is, the resistance to fluid flow is higher and the velocity downstream is reduced [15]. This fact means that, although larger values of N lead to higher velocities (and Re), a polygon with less sides may have induced a better performance than one with a greater N. This information is summed up in figure 15, obtained from the same study as the previous images. Every section view shown in figure 15 has a small circle on the edge, this circle represents the flow separation point. As it can be clearly observed, the point where the flow is detached from the wall is significantly influenced by the sides' orientation.

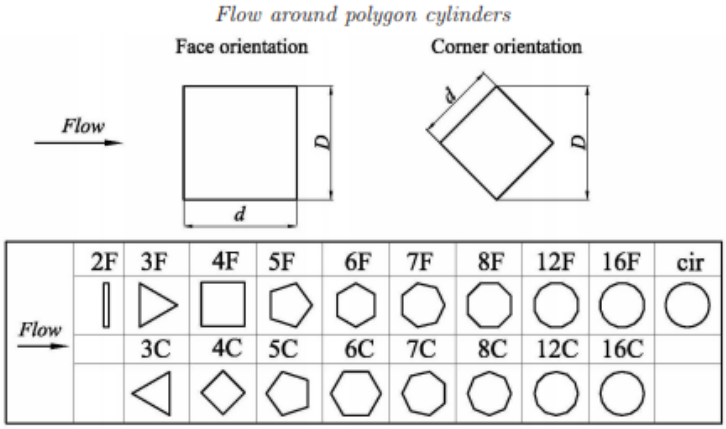

Figure 14. Analysed geometries.

Concerning the roughness on the flap surface, figure 16 [16] shows a comparison between experimental results and simulated outcomes. The experiment, measured by microPIV, takes into account the surface roughness however, the performed simulations consider an ideal smooth surface.

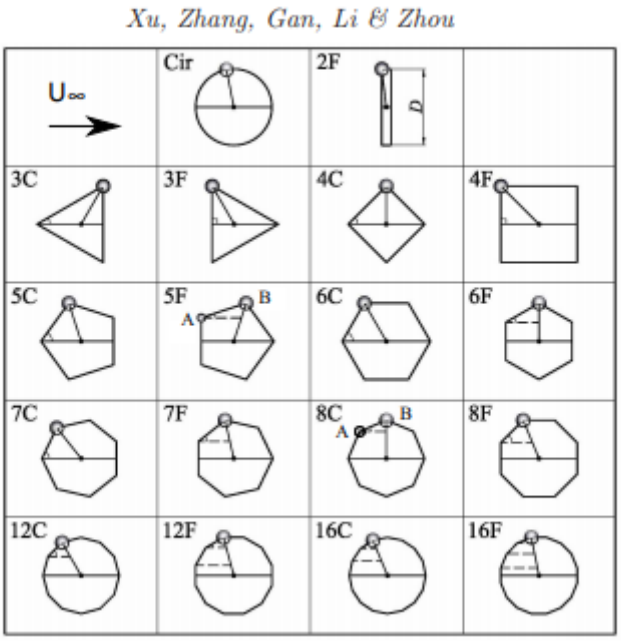

Figure 15. Orientation influence of the flow separation.

In the figure below four plots for different assessed heights are displayed, Z represents the measurement height (measured from the bottom). The fluid flows in the y-direction (same direction as the channel longitude) and the graph represents the velocity profile (u(y)) along the channel. The dark circle represents the experiment in the laboratory while the white square symbolises the CFD simulation. It can be seen how the rough surfaces reaches higher velocities than the smooth one.

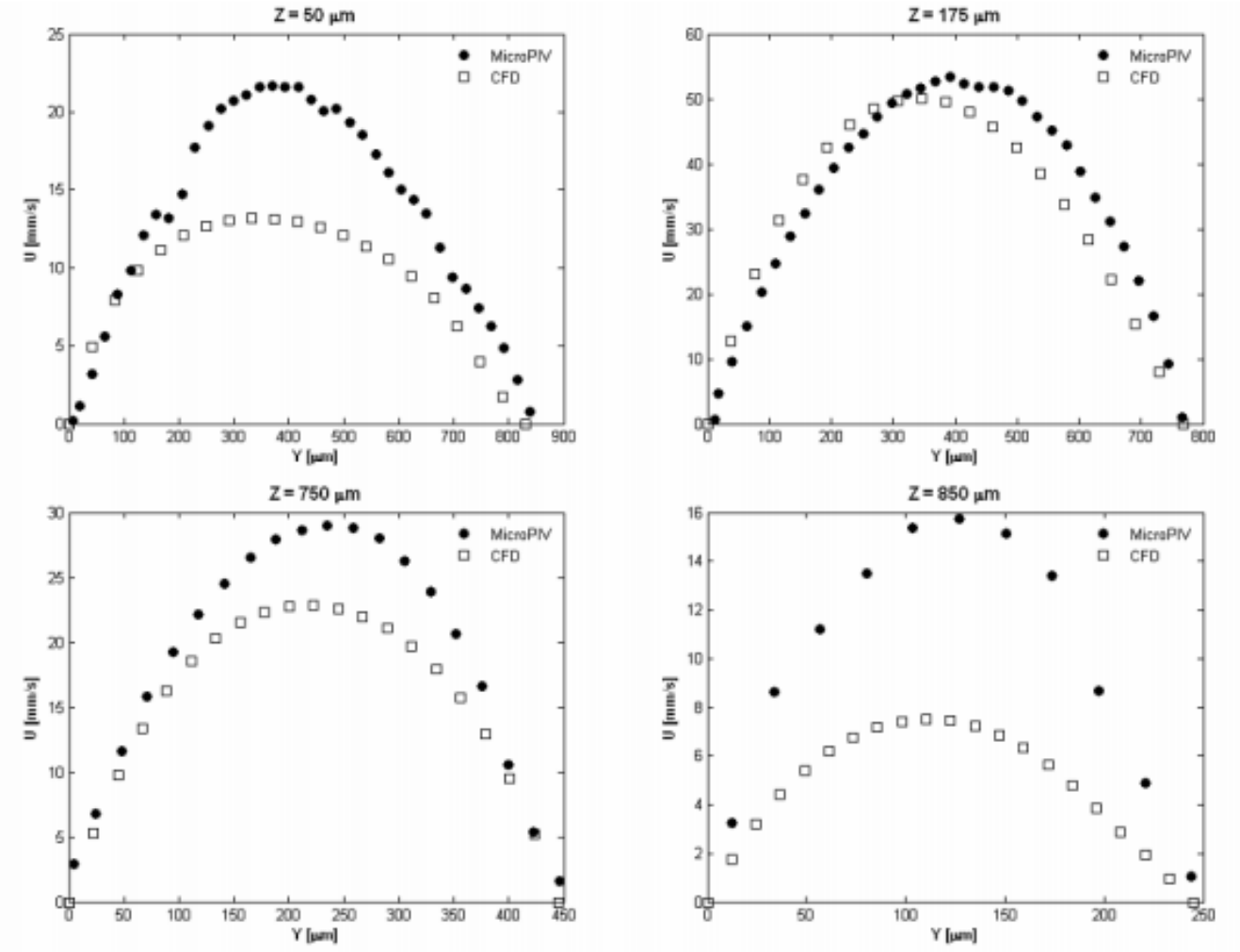

Figure 16. Comparison between rough and smooth surfaces. [16]

Regarding the roughness, it is also remarkable that in general the friction factor (f) is usually decreased as the fluid Re number is increased. [17].

4. Results and discussion

4.1 2D Model

4.1.1 Microfilament

As mentioned, the objective of this project was to figure out which is the disposition that helps the most to accelerate the working fluid. With that purpose, the maximum achievable Reynolds number was measured for every possible combination and compared with the Reynolds number at the inlet. For each assessed length of microfilament, all the evaluated radius were plotted as shown in the figures below.

This plot shows the evolution of the Reynolds number as the velocity is increased for every combination of height and radius. Each subplot represents an evaluated filament length and, in every subplot, all the analysed radius are compared.

For a better understanding and a clearer overview of all the obtained results, Figure 18 and Figure 19 are included. The slope of every line plotted in figure 17 was obtained. This slope represents the ratio between maximum Reynold achievable and inlet Reynolds number, for every combination of filament length and radius. In figure 18, these ratios where used to assess how the increment on the radius affects the performance of every proposed model. In the same image, this evolution is shown for every assessed height. Furthermore, using the ratios previously obtained, figure 19 represents the change in the fluid velocity as the rod height is increased. In addition, in the same graph, all the radius were assessed.

Another relevant parameter to optimize was the pressure. In order to compare the maximum pressure gradients obtained, figure 20 was included. Each subplot on figure 20 represents a fixed radius and, for every settled radius, all the filament lengths are valuated. As in the case of the Reynolds number, the larger the maximum pressure gradient, the better the performance of the design.

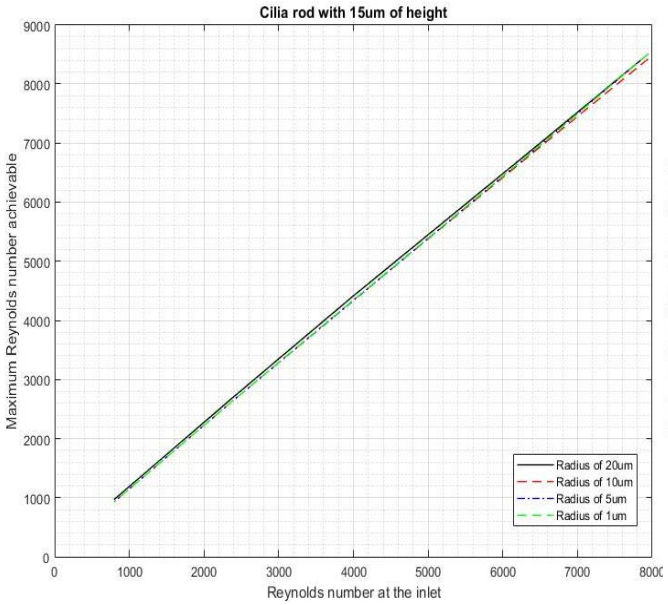

(a). Different radius comparison for a filament length of 15 μm

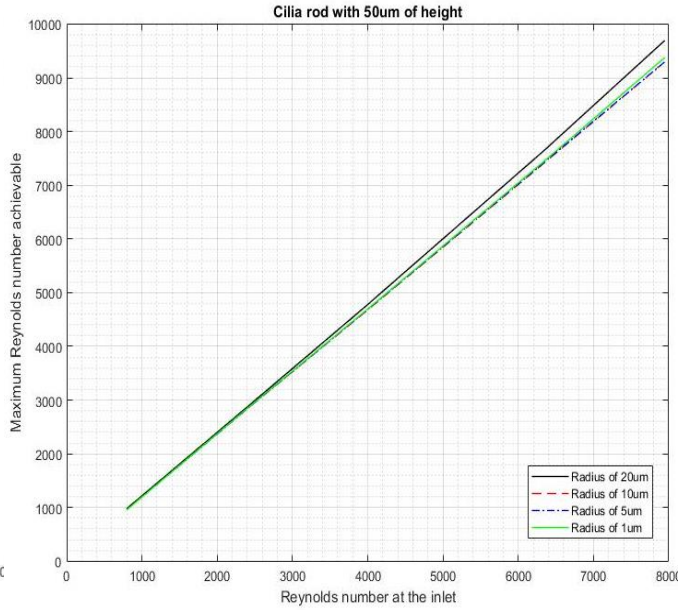

(b). Different radius comparison for a filament length of 50 μm

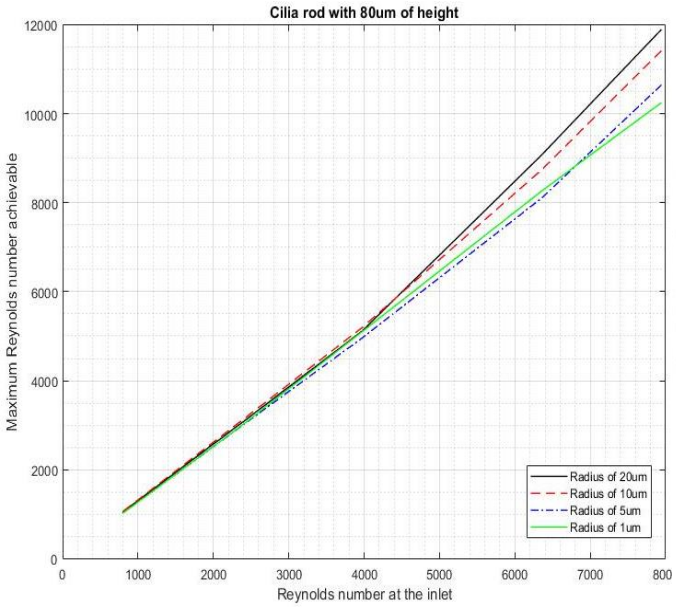

(c). Different radius comparison for a filament length of 80 μm

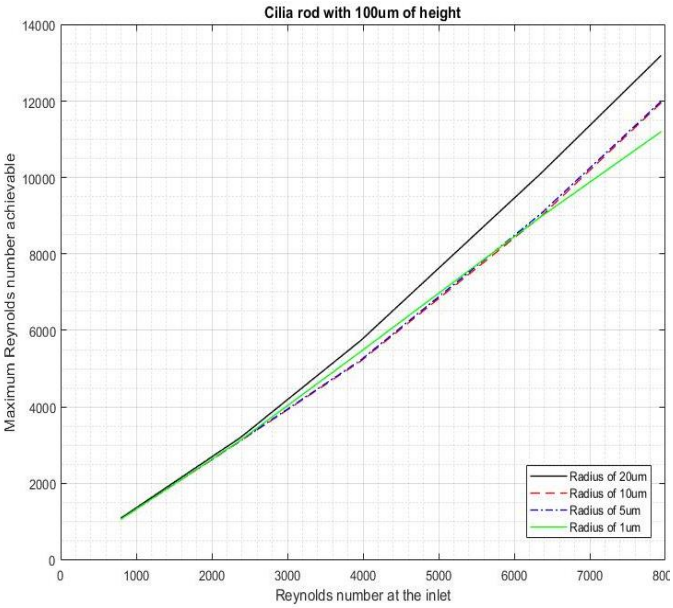

(d). Different radius comparison for a filament length of 100 μm

Figure 17. Maximum achievable Reynolds number vs inlet Reynolds number. Comparison for different radius and lengths.

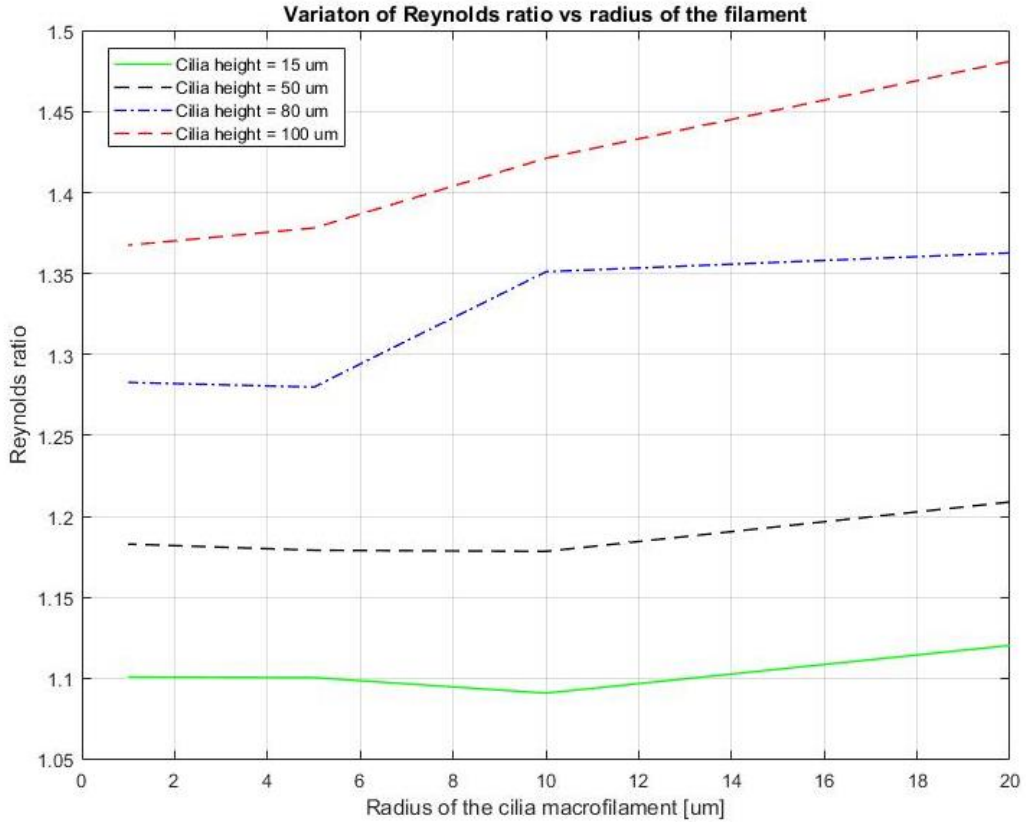

Figure 18. Comparison Reynolds number vs radius for every constant height.

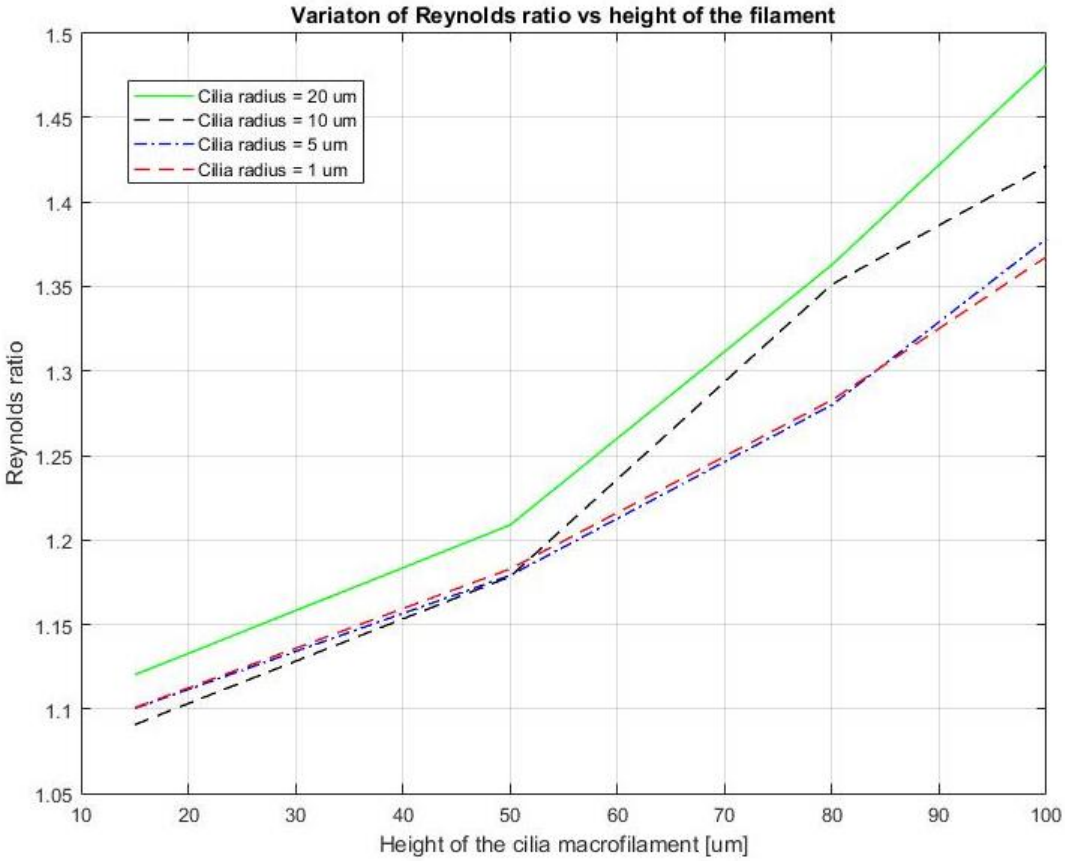

Figure 19. Comparison Reynolds number vs height for every constant radius.

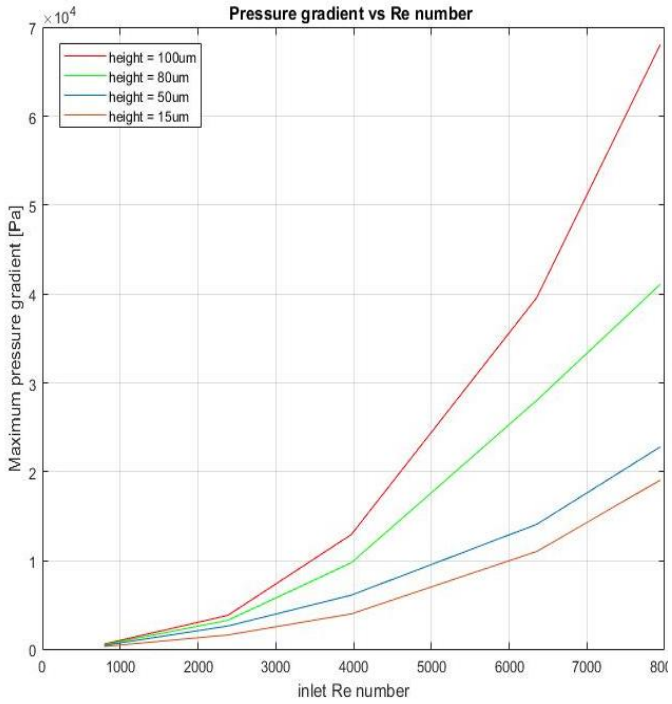

(a). Maximum pressure gradient vs inlet Re. For a constant radius of 1 μm

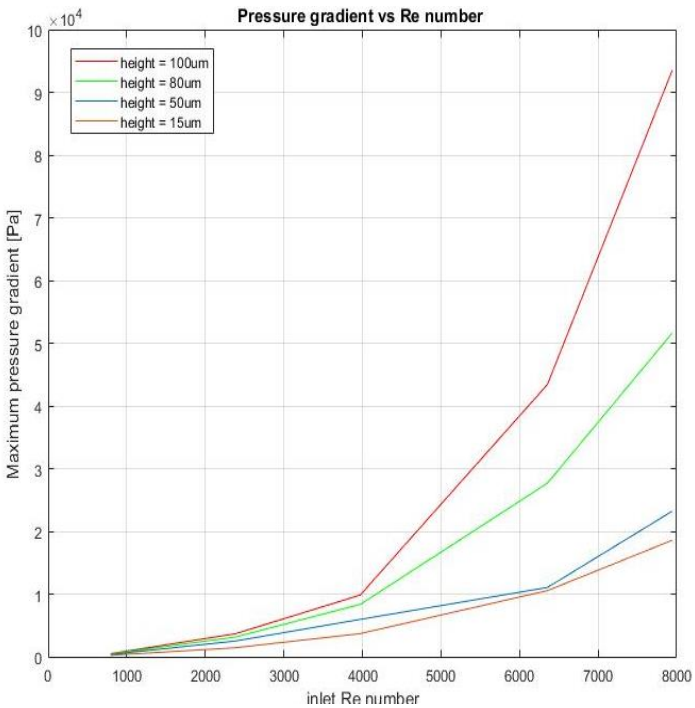

(b). Maximum pressure gradient vs inlet Re. For a constant radius of 10 μm.

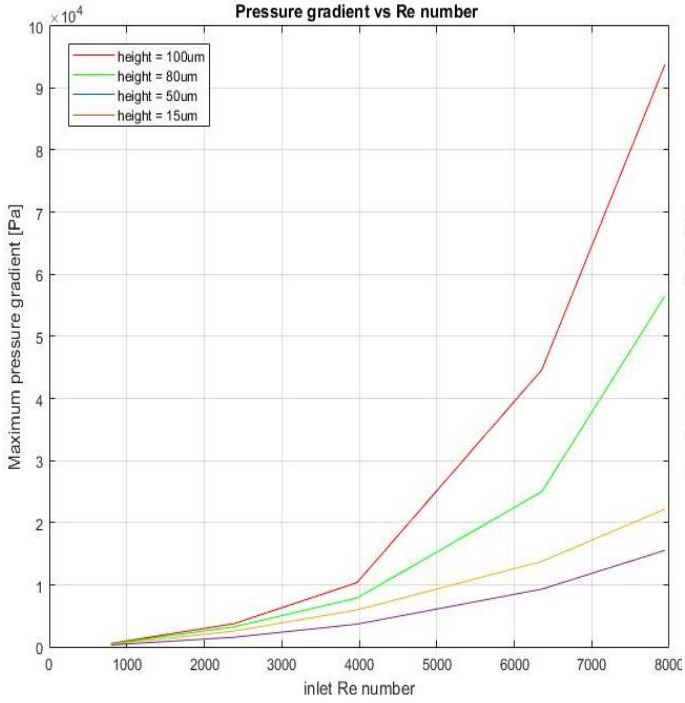

(c). Maximum pressure gradient vs inlet Re. For a constant radius of 5 μm

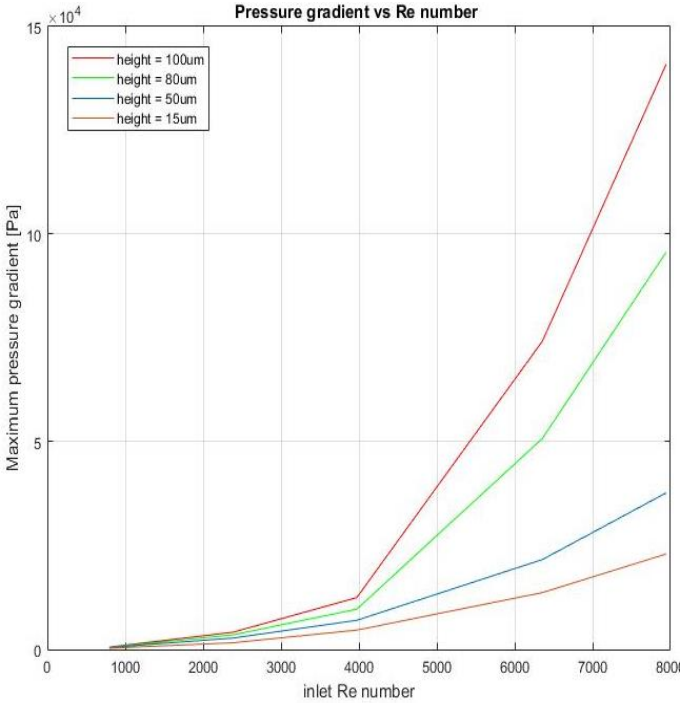

(d). Maximum pressure gradient vs inlet Re. For a constant radius of 20 μm.

Figure 20. Comparison of maximum pressure gradient vs inlet Reynolds number for every height with a constant radius.

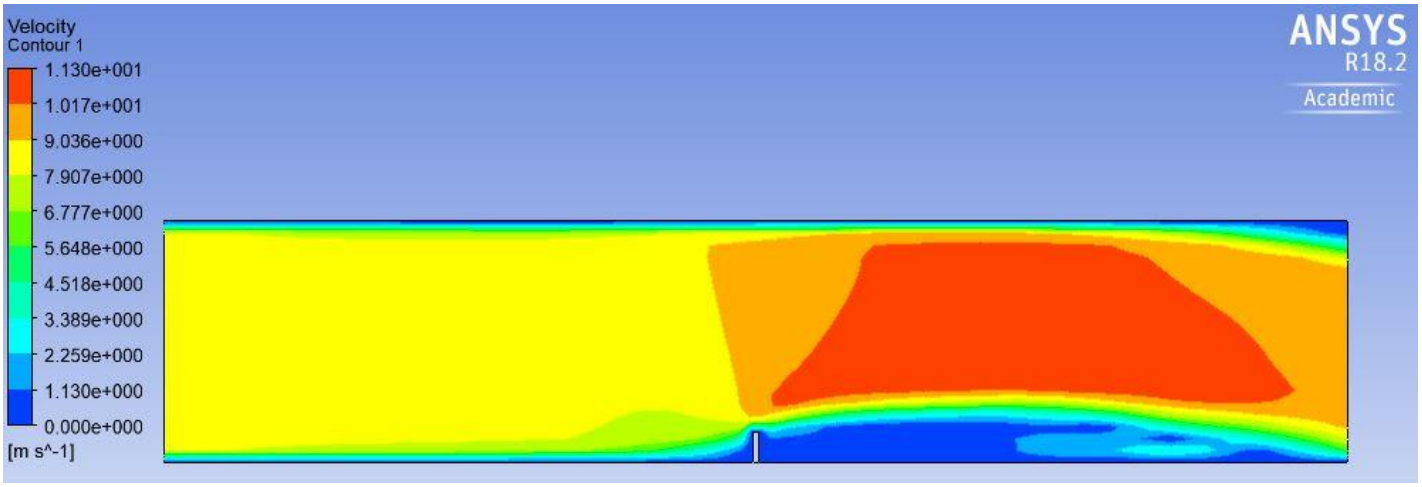

(a). Velocity contour.

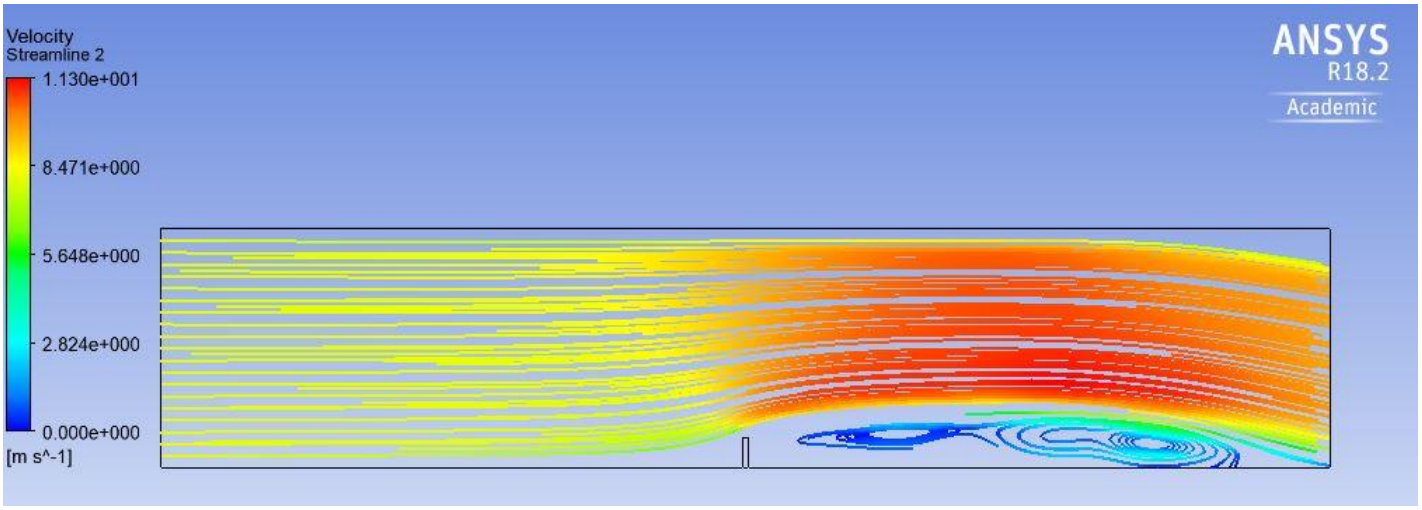

(b). Streamlines.

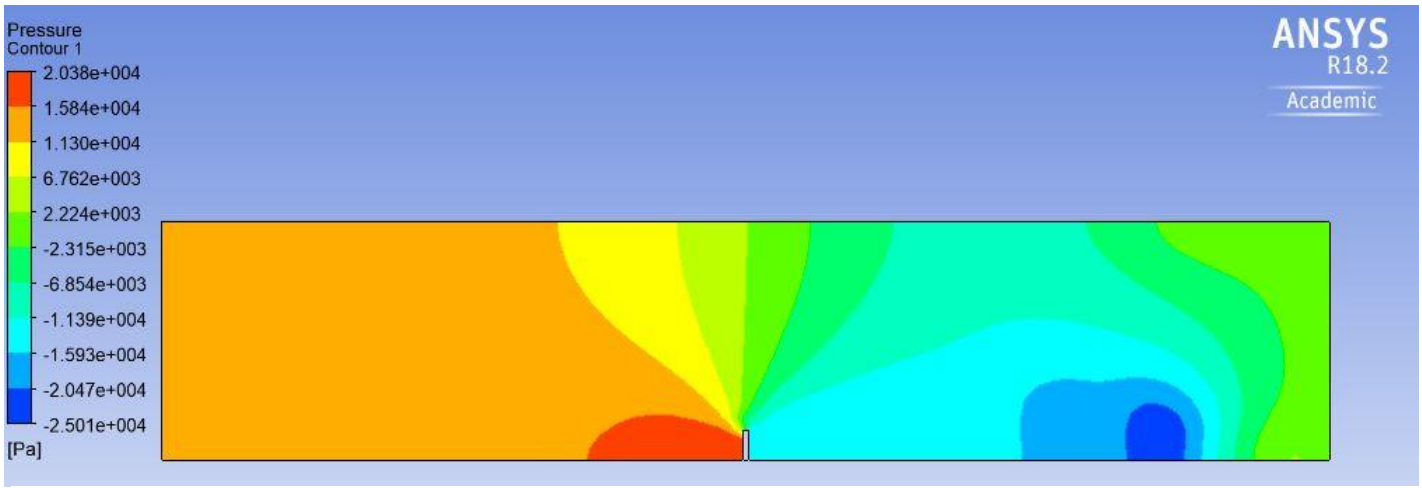

(c). Pressure contour

Figure 21. Ansys Fluent result (2D)

Previous pages mostly show numerical results of the maximum obtainable outcomes. This is a good approach in order to figure out which is the most optimal design. However, the images displayed figure 21 give a more visual view of the fluid evolution inside the channel.

Figures 21 (a), (b) and (c) display the velocity contour, streamlines and pressure contour, respectively. All the illustrations above were obtained by imposing an inlet velocity of 8m/s. They help to analyse the behaviour of the working fluid inside the channel, recognising which are the areas achieving a higher velocity and a larger pressure gradient.

As mentioned, the main parameter used to evaluate the result was the velocity of the fluid, represented by the Reynolds number.

Starting for the modelling in two dimensions, figure 17 represents maximum Reynolds number vs inlet Reynolds number. Each subplot shows the results for a different rod height and, inside that subplot, all the evaluated radius are compared.

Figure 17 (a) displays the results for the shortest filament height analysed. The maximum velocity obtained in this simulation is significantly lower than others. As it can be observed, all the lines roughly overlap each other since the variation in radius barely affects the results.

When the height is increased up to 50 μm (Figure 17 (b)) the effect of the radius starts to be noticeable for the highest velocities. The maximum Reynolds number is, in general, increased but it can be also seen how simulations performed with a radius of 20 μm reach higher velocities. It reaches, approximately, Re numbers 200 units larger than other assessed radius. However, for radius of 10, 5 and 1 μm the results cannot be really differentiated and they overlap.

For heights of 80 and 100 μm, displayed in figures 17 (c) and (d), the evolution is similar. For lower velocities there is no a considerable distinction between different radius. As the Reynolds number is increased, for both filament longitudes, it can be observed how a radius of 20um has the best performance. A radius of 1 μm (green line) does not obtain favourable outcomes for larger velocity magnitudes. Radius of 10 and 5 μm get coincident results for the highest length. However, for a height of 80um, the slenderness is high enough to make the results obtained with a radius of 10 μm surpass the ones obtained with 5 μm.

The previous discussion is summarized in figures 18 and 19. On these figures, it can be clearly observed that the best performance is obtained for a cilia length of 100 μm and a radius of 20 μm (slenderness = $\frac{\textbf{longitude}}{\textbf{raius}} = 5$), as it was expected from figure 17. The maximum Reynolds ratio obtained ($\frac{Maximum\ achievable\ Re}{Inlet\ Re}$) is 1.5 and the maximum Reynolds achieved (under an inlet velocity of 10m/s) is slightly higher than 13000.

Regarding the pressure (Figure 20), as it was expected, the design that optimizes the results coincides with the previous one. A microfilament with a length of 100 μm and a radius of 20 μm achieves a maximum pressure gradient

of the order of $15 \cdot 10^4$ Pa. Nevertheless, the worst performances derive from the lowest heights and radius, which coincide with the lowest slenderness.

From figure 21, it is perceived how the highest velocities arise immediately after the filament. The maximum pressure gradient occurs also next to the filament. The pressure downstream is negative since, due to the geometric imposition of the solid boundary, a pressure drop point is produced.

4.1.2 Macrofilament

The procedure followed in this section is similar to the preceding one. In this case the magnitude of the design was amplified from micrometric scale to millimetric one. The followed methodology was the same, the maximum Reynolds number was plotted vs the inlet Reynolds number. From those graphics, the Re ratios were obtained. In this case, 'Maximum achievable Reynolds number vs inlet Reynolds number' plots were not added in order to avoid excess of content. However the relevant results, where the most optimal designs can be easily identified, are shown below.

Analogous to passage 4.1.1, figure 22 represents the Reynolds ratio as a function of the height for each of the analysed radius. Figure 23 displays Reynolds ratio evolution as the radius is increased for every filament height. In both graphs, the fluid performance can be assessed while varying either the height or the radius. Consequently, the most efficient design combination can be identified.

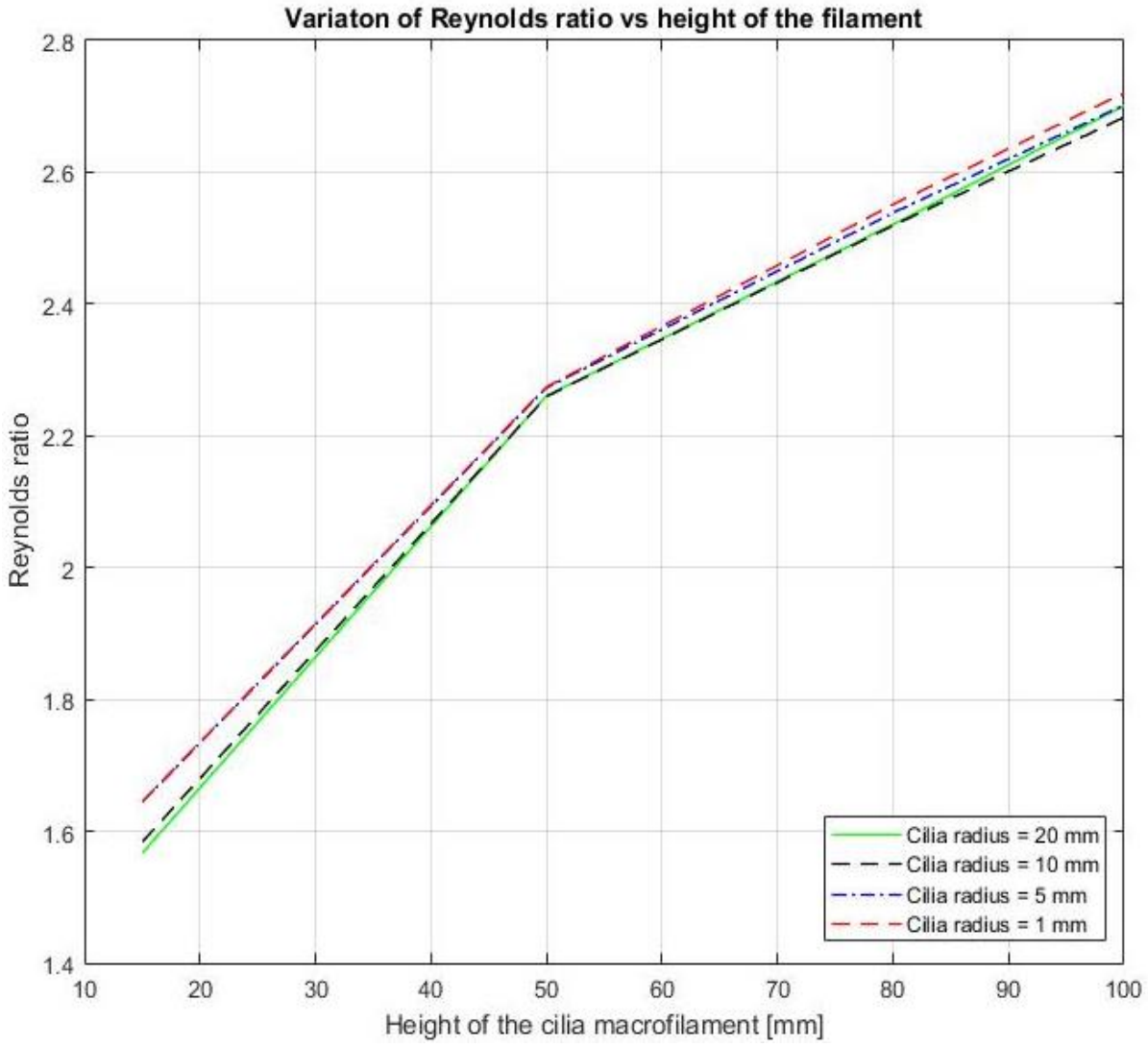

Figure 22. Comparison Reynolds number vs height for every constant radius.

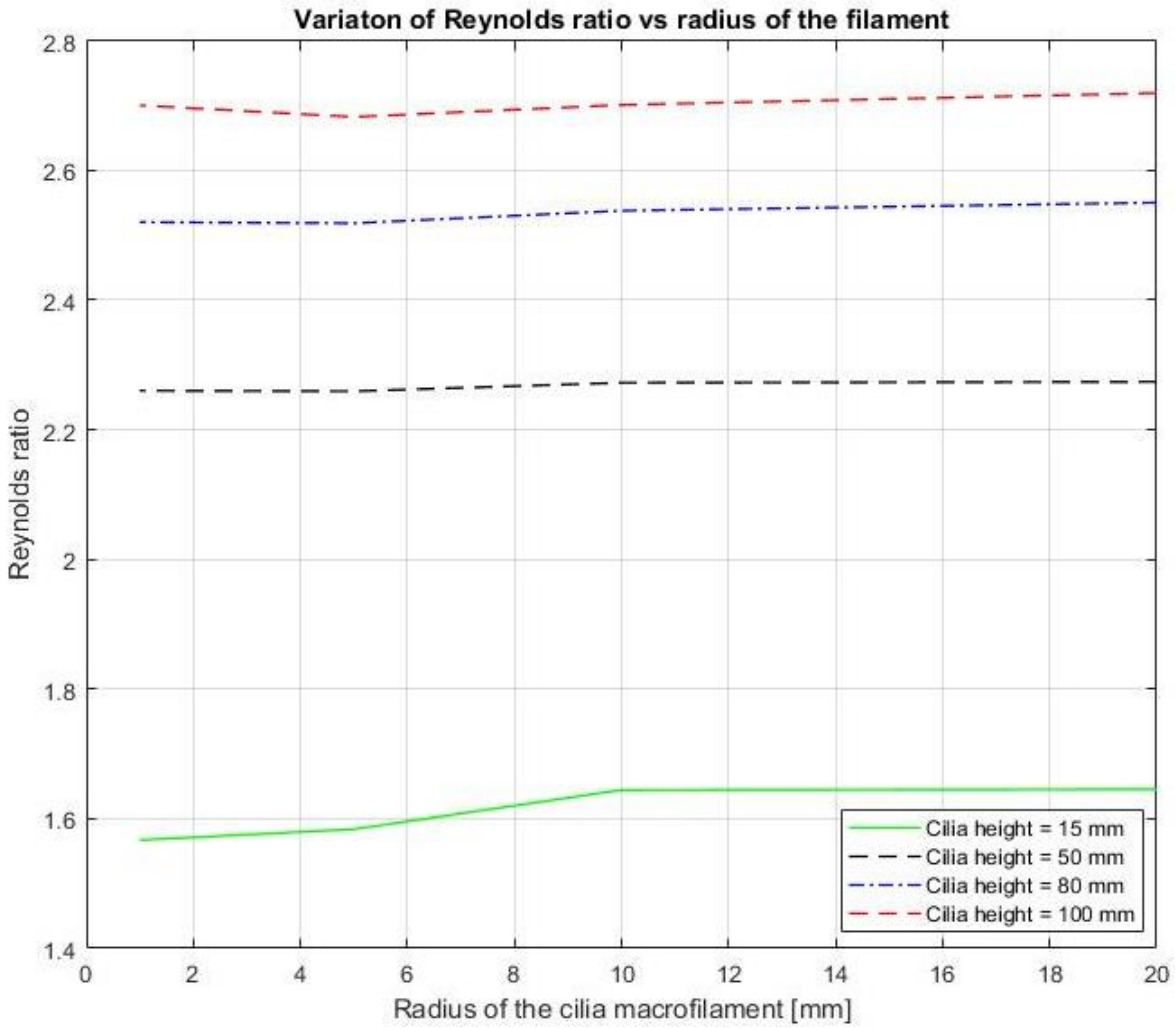

Figure 23. Comparison Reynolds number vs radius for every constant height.

Graphics below (Figure 24) allow to compare the maximum pressure gradient that can be achieved with every assessed solution. They display evolution of the pressure gradient as the inlet velocity is increased for every filament length. Each of the subplots represent one of the four radius evaluated.

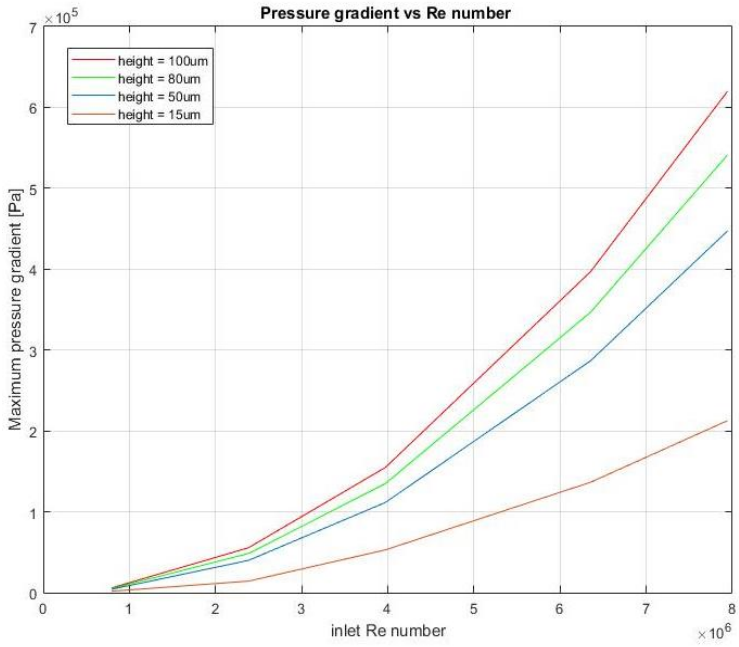

(a). Maximum pressure gradient vs inlet Re. For a constant radius of 1um

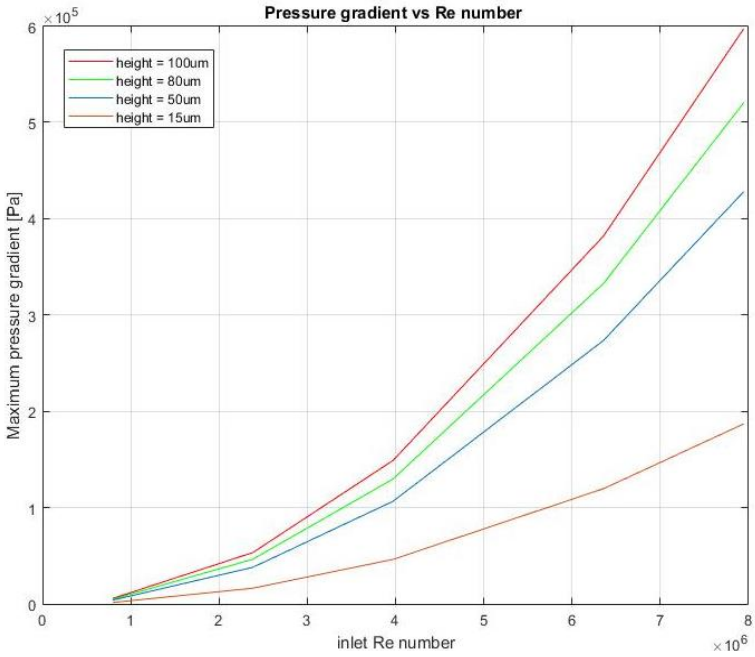

(b). Maximum pressure gradient vs inlet Re. For a constant radius of 10um

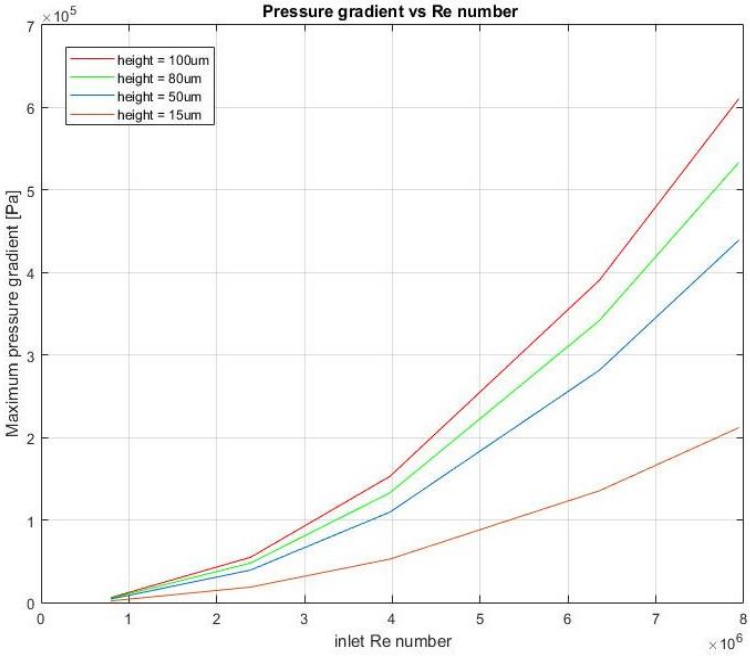

(c). Maximum pressure gradient vs inlet Re. For a constant radius of 5um

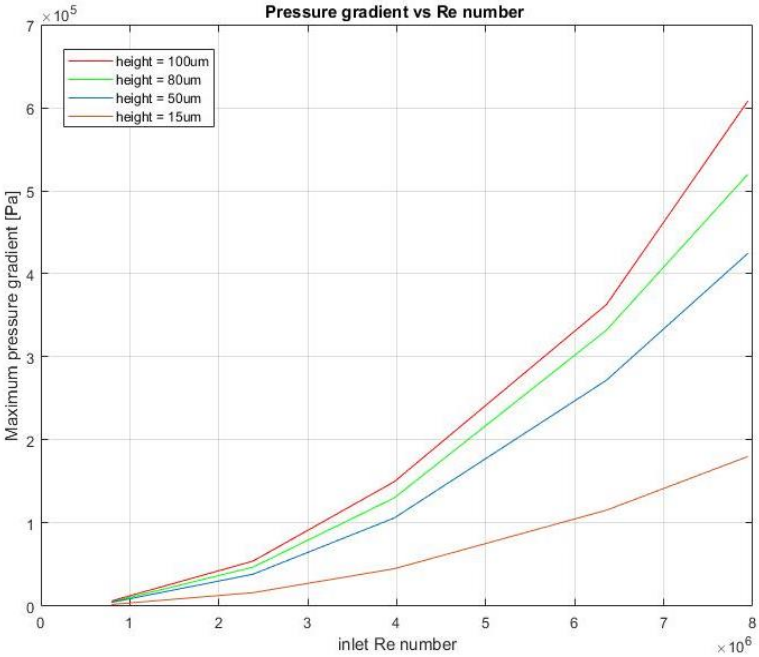

(d). Maximum pressure gradient vs inlet Re. For a constant radius of 20

Figure 24. Comparison of maximum pressure gradient vs inlet Reynolds number for every height with a constant radius..

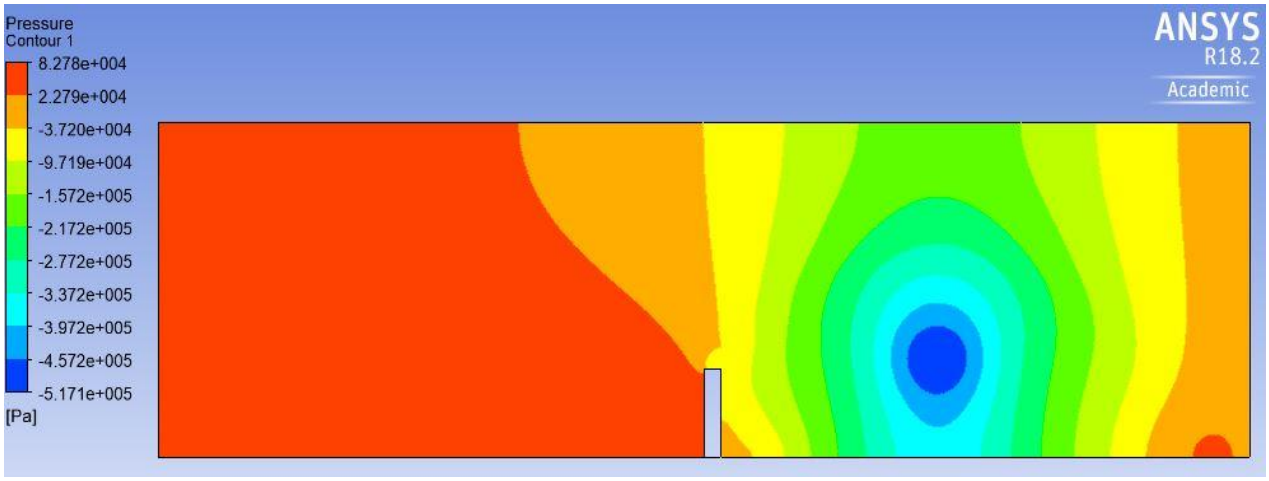

(a). Pressure contour.

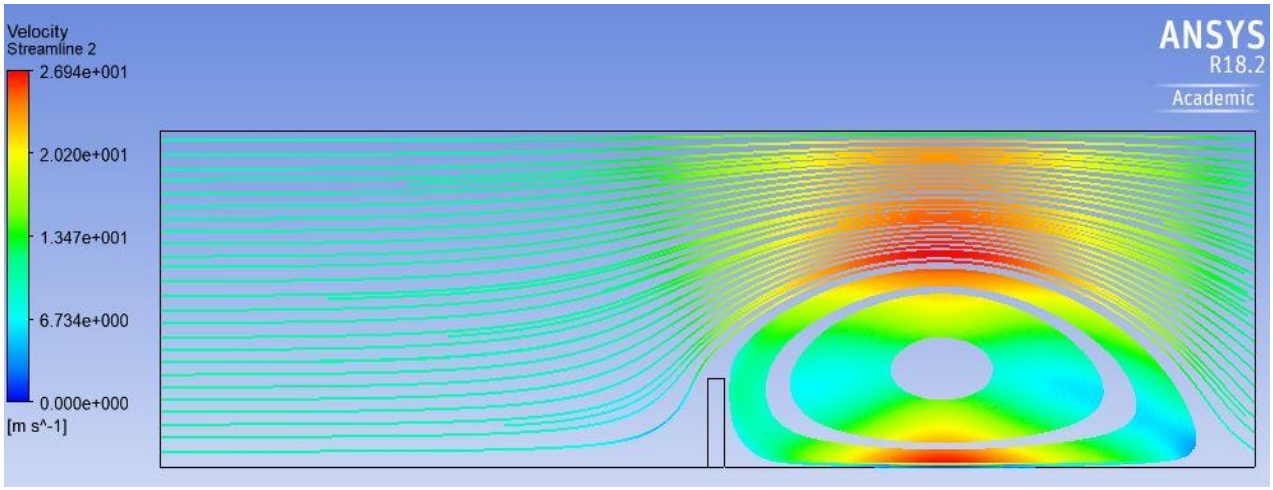

(b). Streamlines.

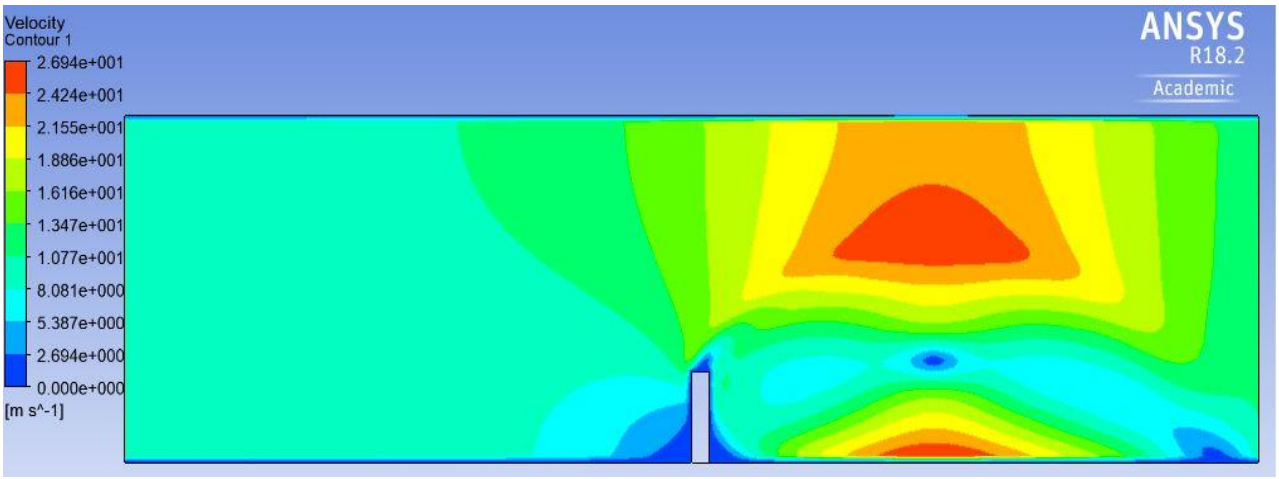

(c). Velocity contour.

Figure 25. Ansys Fluent results

As in the preceding section, a more visual representation of the working fluid through the channel is displayed on Figures 25. Images (a), (b) and (c) above show the pressure contour, stream lines and velocity contour, respectively. All of them result from an imposed initial velocity of 10m/s.

Figure 25 (a) allows to detect the area where the maximum pressure difference is present. 25 (b) represents a group of fifty streamlines. The lines are instantaneously tangent to the velocity vector of the flow. They show the direction in which the fluid travel at every point. Lastly, 25 (c) recognizes the regions where the fluid stands a higher acceleration.
These plots are especially useful to visually connect the performance of the designed material with its main purpose: to help and to ease the mixing of substances or to improve the transportation of fluids through microchannels.

As mentioned, the procedure followed for the simulation of the macrofilament was very similar to the one adopted in the section before. The same parameters were analysed and the results were plotted into graphs for a better comprehension. Since the figures of 'Reynolds ratio vs height' or 'Reynolds ratio vs radius' were enough to identify the most optimal design, 'maximum achievable Reynolds vs inlet Reynolds' was not displayed, in this case, for any filament height.

From figure 22 and 23, it can be seen that the best performance is clearly obtained with a length of 100mm. Also, under this conditions, the chosen radius for the simulation does not seem to affect substantially to the results. However, smaller radius like 1 and 5 mm appear to give more optimal results.

Regarding the pressure (Figure 24), best efficiencies are obtained for larger microfilaments reaching values of the order of $6 \cdot 10^5$ Pa. Equivalently to the velocity analysis, the length of the radius does not really influence the outcomes. Nevertheless, small radius reach slightly better performances.

Figure 25 shows the behaviour of the fluid inside the channel. As before, the pressure immediately after the filament is negative. The velocity is highly increased after the rod reaching values of 26.94 m/s when an input velocity of 10m/s was imposed. Streamlines clearly show the direction followed by the fluid velocity.

4.2 3D Model

4.2.1 1D Columns

As it was explained in section 3.1, after performing a 2D simulation, the model was brought to a three dimensions field. This part of the optimization process was subdivided into two sections. Firstly, a geometry optimization procedure was carried out. This operation, whose results are shown in section 4.2.1.1, consisted in finding the section geometry, together with the cilia column length, that optimizes the behaviour of the fluid.

The second stage, displayed in 4.2.1.2, dealt with the separation, longitudinal and crosswise, between filaments. The aim was to find the distances Sx and Sz, shown in figure 8, that induce the best performance. The length Sx is equal between all the longitudinal elements in the same row, Sz remains also the same for all the transversal columns in the same line. Both separations had been changed and analysed in every simulation with the purpose of finding the most suitable disposition.

4.2.1.1 Geometry optimization

Taking into consideration that the variables to be optimized are velocity and pressure, the same proceeding as for the 2D simulation was carried out.

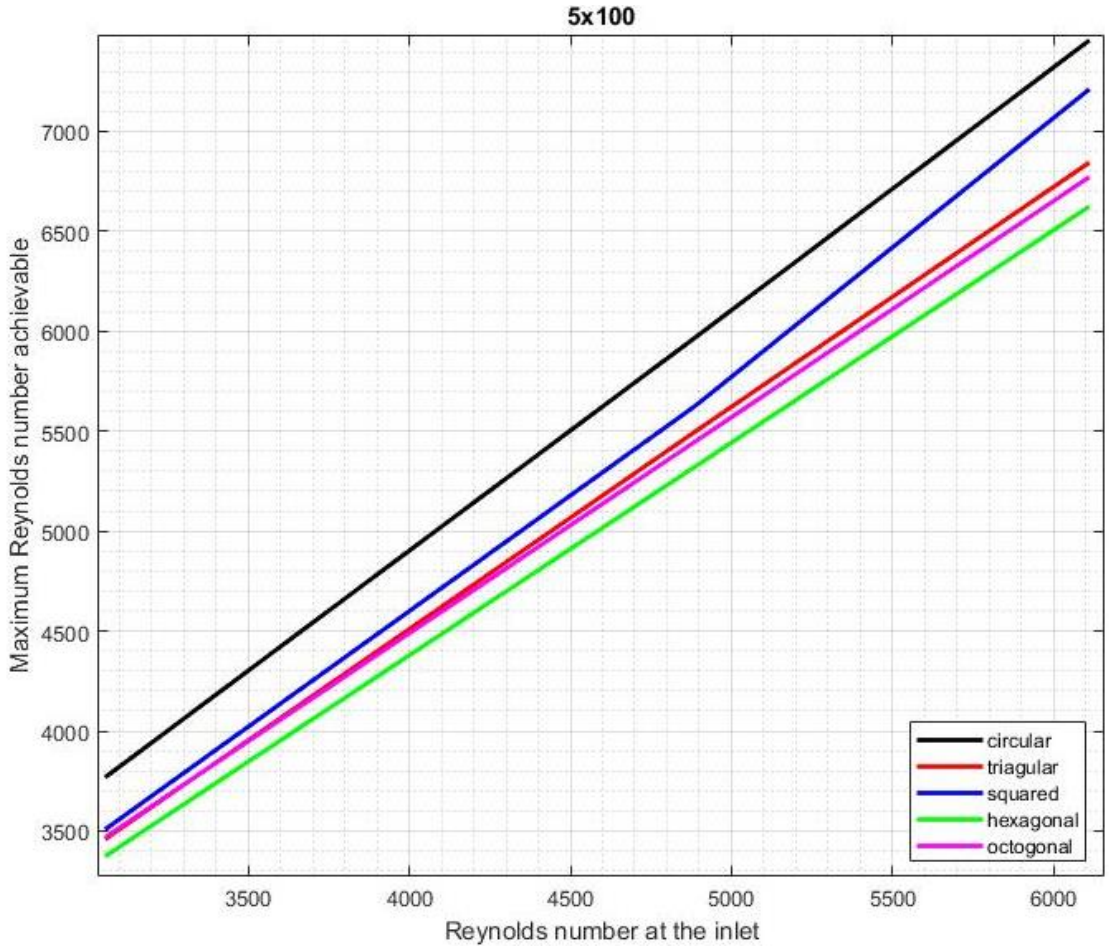

Figure 26.Maximum Re achievable vs inlet Re. Height 100 μm and apothem 5 μm. Different sections.

In first place, the maximum achievable Reynolds number was compared with the inlet one. These results are displayed in figures 26, 27, 28 and 29. All these graphs represent how different section geometries with a defined apothem length (or radius for the circular section) and using the same filament length affect the fluid. They allow to determine the structure geometry and length that optimizes the results.

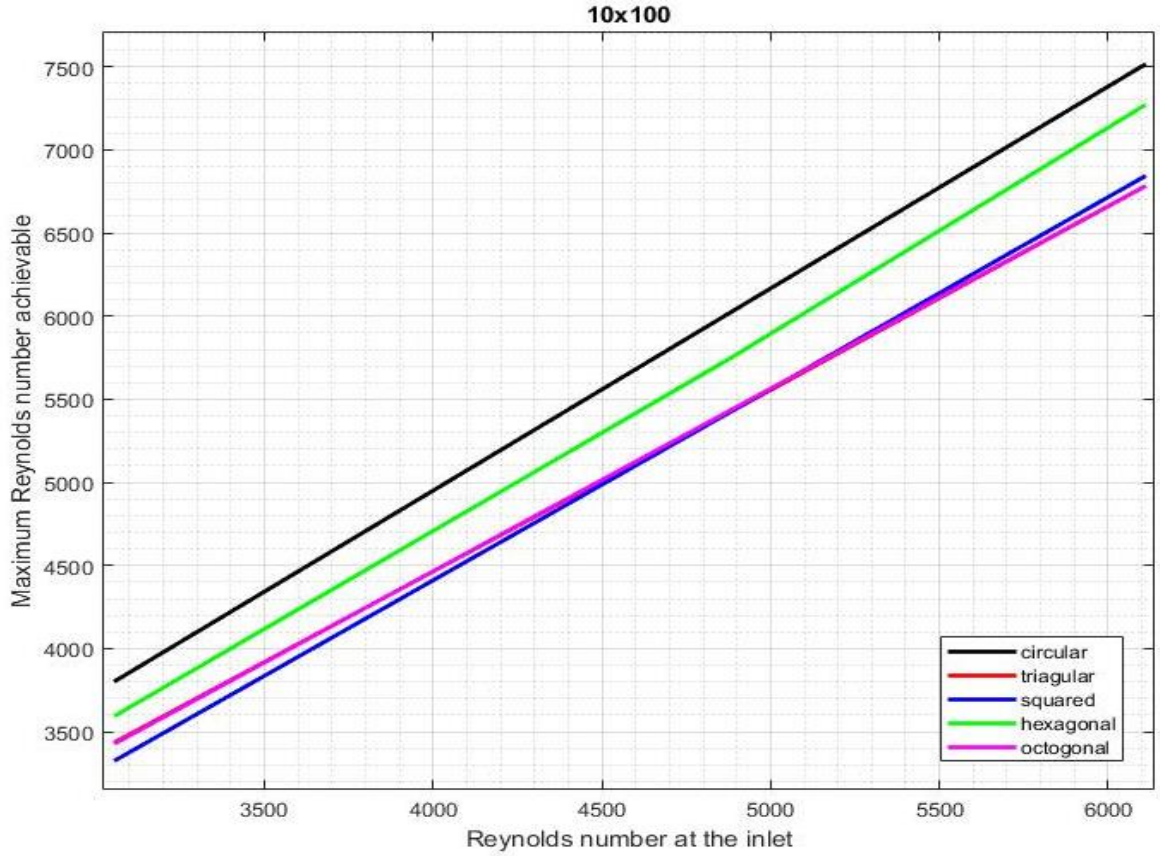

Figure 27. Maximum Re achievable vs inlet Re. Height 100 μm and apothem 10um. Different sections

Figure 26 present outcomes for a section apothem of 5um together with a filament height of 100um, figure 27 displays the same height but with an apothem of 10 μm.

Figure 28 shows the results of a filament with an apothem of 10 μm together with a rod length of 80 μm. Meanwhile, the design represented in figure 29 has the same height but varies the section apothem to 5 μm.

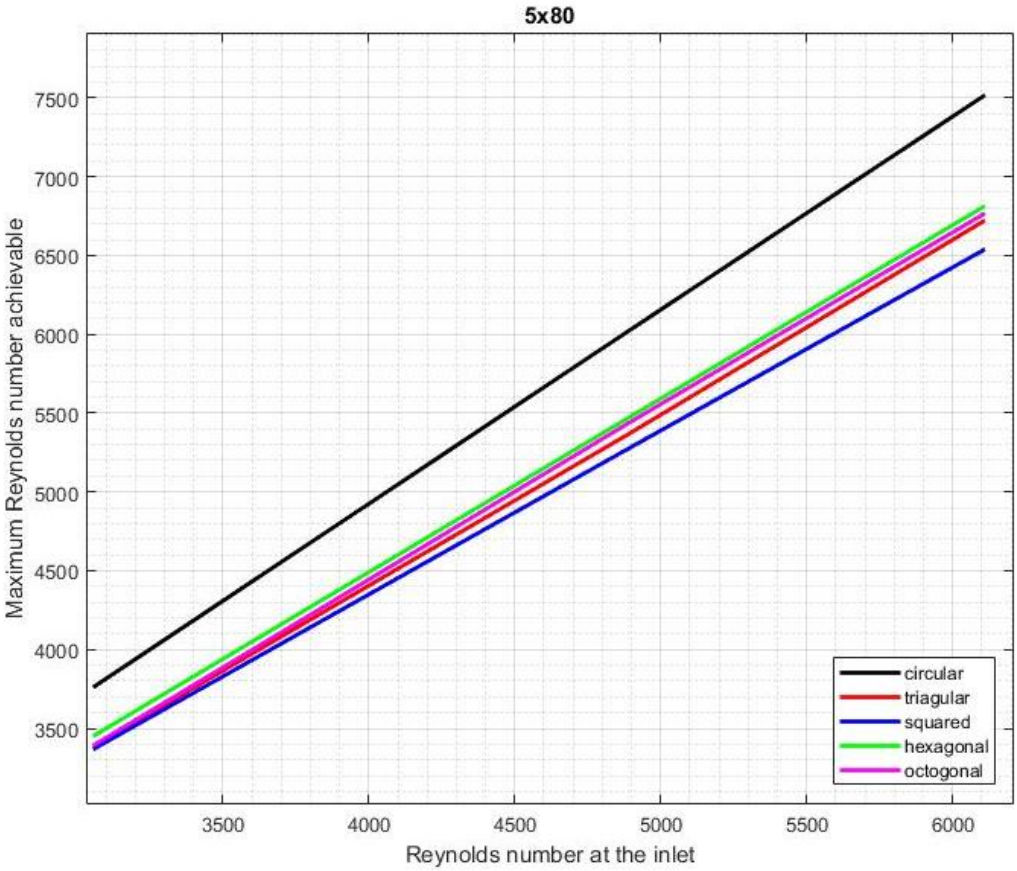

Figure 29. Maximum Re achievable vs inlet Re. Height 80 µm and apothem 5 µm Comparison among different sections

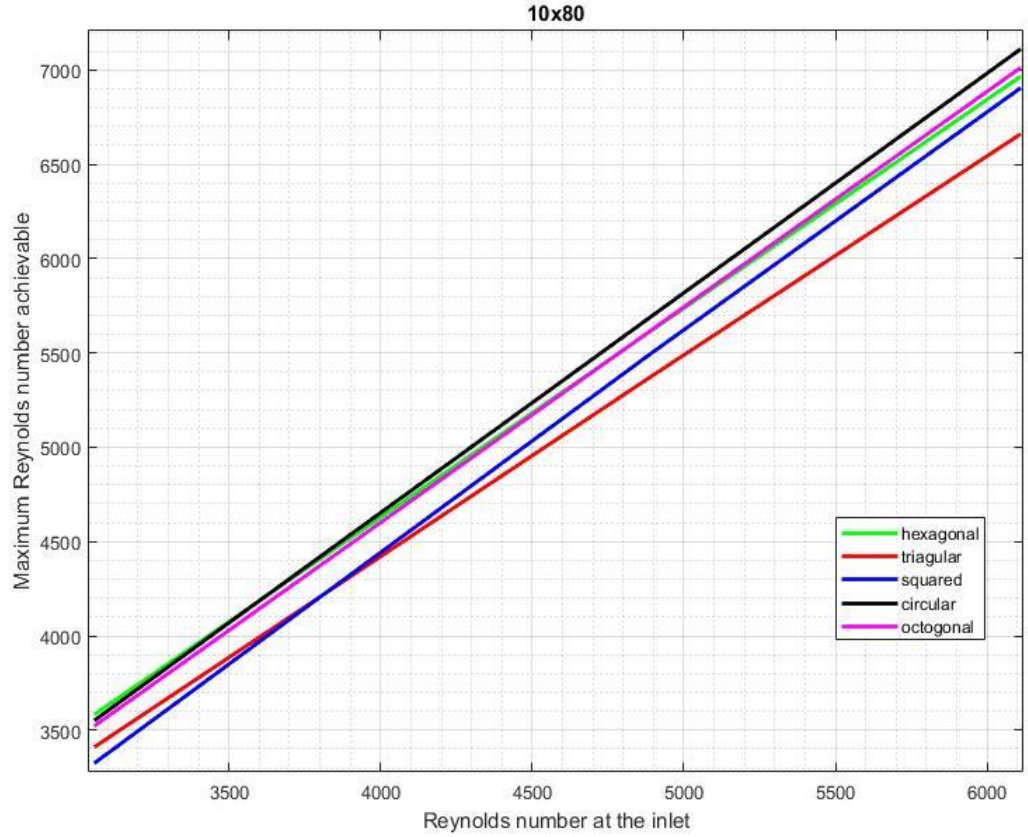

Figure 28. Maximum Re achievable vs inlet Re. Height 80 µm and apothem 10 µm Comparison among different sections

As it will be explained, the results above gave two potential filaments geometry which could be eligible. Since the pressure is another relevant parameter linked to the velocity, the maximum achievable pressure gradient for those results was plotted against the Reynolds number at the inlet (representing the velocity). These results are shown in figure 30.

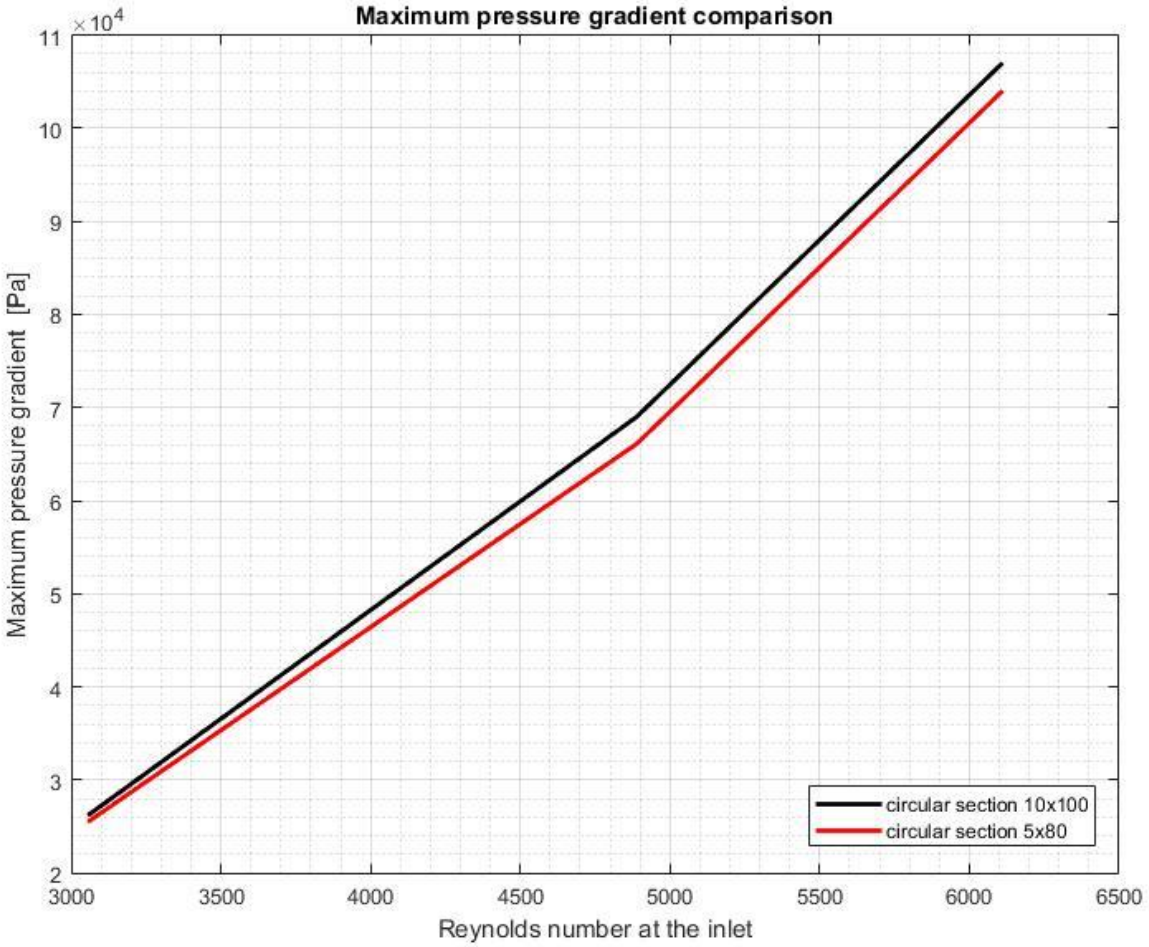

Figure 30. Maximum pressure gradient comparison for the most optimal designs.

The first optimization step on this section was dealing with the geometry of the section. As it was explained, different length and apothems were evaluated and combined between them. Figure 26, representing a height of 100 μm and an apothem of 5 μm, shows that the circular section clearly optimizes the result. It can be observed that the worst performance, in this case, is accomplished by the hexagonal section. Triangular and octagonal sections obtain similar outcomes. The squared section achieves also a good performance, only surpassed by the circular one which obtains values for the Re number of around 7500. The fact that the circular section achieved the best outcomes coincides was expected regarding the experimental results shown in figure 13. Although the expected result would be higher achievable Re for an octagonal or a hexagonal section (due to larger N), the graphic shows a better performance for the squared section. This may be due to the previously explained issue of the flow separation. As explained in section

3.2 and in figure 15, depending on the side orientation and the section size, the flow separation may occur earlier or later and this may alter the estimated results.

In figure 27, under the same height as the preceding one, the apothem is increased up to 10 μm. Once more, the section which optimizes the outcome is the circular one. It is followed by the hexagonal section. Lastly, octagonal, squared and triangular sections overlap each other, giving all of the poorer results. The maximum Re achieved, for the circular section, is around 7500. This value is around 700 units higher than the worst one obtained for the same input velocity. For this case, the outcomes follow a more similar behaviour to the expected regarding figure 13. The circular section provides the most optimal performance followed by the other geometries ordered by decreasing N. Juts the orthogonal section follows an unexpected tendency since it was predicted to surpass the hexagonal outcomes.

Figure 28 displays the results for a height of 80um together with an apothem of 10um. In this plot the results are slightly different than in previous cases. Best performances are obtained with a circular section, followed closely by the octagonal and the hexagonal ones. The squared section gets the worst result for lower inlet velocities however, it gets closer to the hexagonal one for larger input Reynold numbers. Triangular section, in general, obtains the lowest maximum achievable velocities for this configuration. With this design, the maximum Re obtained is 7100, approximately. This graph follows exactly the behaviour that would be expected from the researched experimental results displayed in figure 13.

In figure 29, again, circular section achieves much higher results reaching Re of the order of 7500. For triangular, hexagonal and octagonal sections the results are pretty similar, especially for lower inlet velocities. Squared section gets lower values for the Re number.

From the discussion above, it can be concluded that the section that optimizes the result, from the analysed range, is the circular one. However, there are two combinations of radius and length that get similar Reynolds numbers. The most efficient designs are a radius of 10 μm together with a length of 100 μm and a radius of 5um with a filament height of 80 μm, both of them with circular sections.

In order to identify the best design, the maximum pressure gradient achievable is plotted for those two final candidates (Figure 30). From this image, the model with a 10 μm radius and a height of 100 μm can be chosen as the most optimal result.

4.2.1.2 Separation distance optimization

As it was previously indicated, the second part was to find a suitable distance between elements. The obtained results are shown below.

Figure 31 shows the velocity performance (represented with the Reynolds number) for a constant crosswise distance between elements Sz equal to 100 micrometres. In the same graph, the results for different separation lengths on the x direction are displayed in order to easily compare.

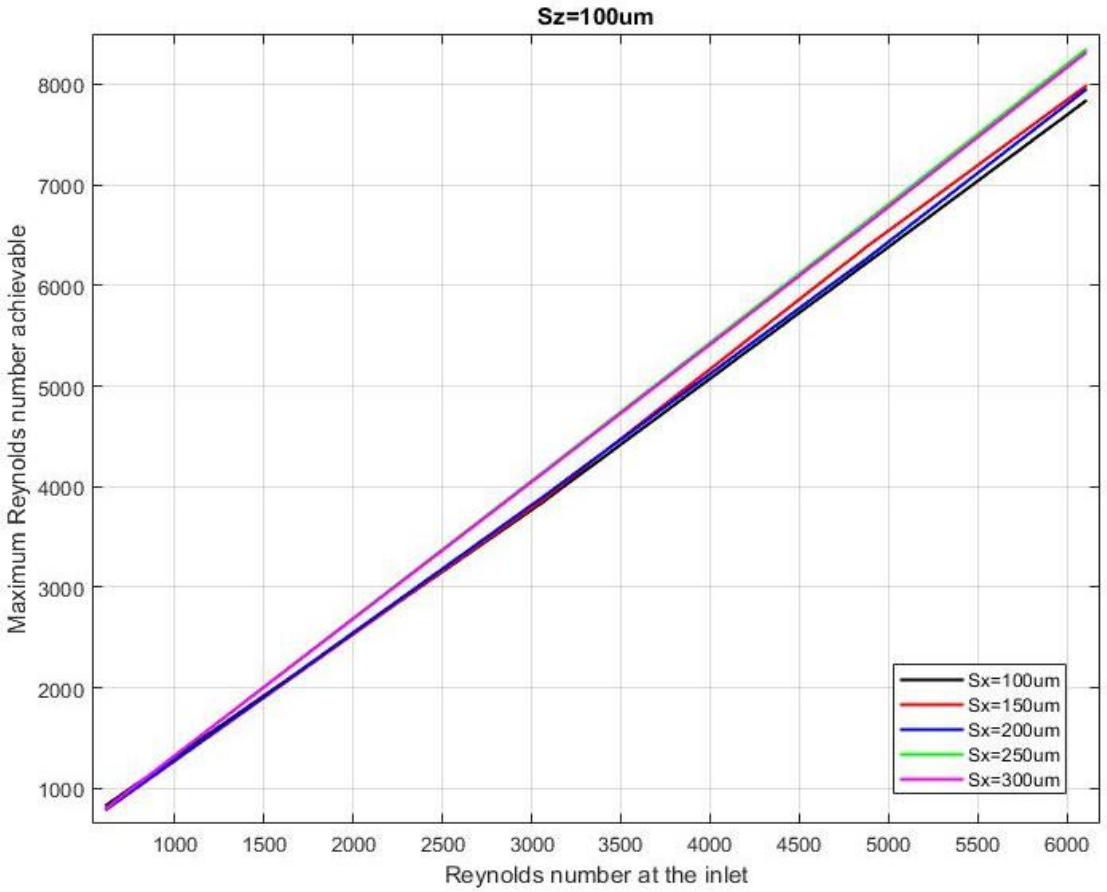

Figure 31. Comparison of 'maximum Re achievable vs inlet Re' for deferent distance values Sx under a constant Sz=100 μm

The region where the obtained results diverge more from one from the other was under the imposition on higher inlet velocities. For this reason and in order to easily distinguish outcomes and compare, figure 32 is added.

Figure 32 displays the results obtained in figure 31 but zoomed in. This allows to easily see the evolution for larger velocity magnitudes.

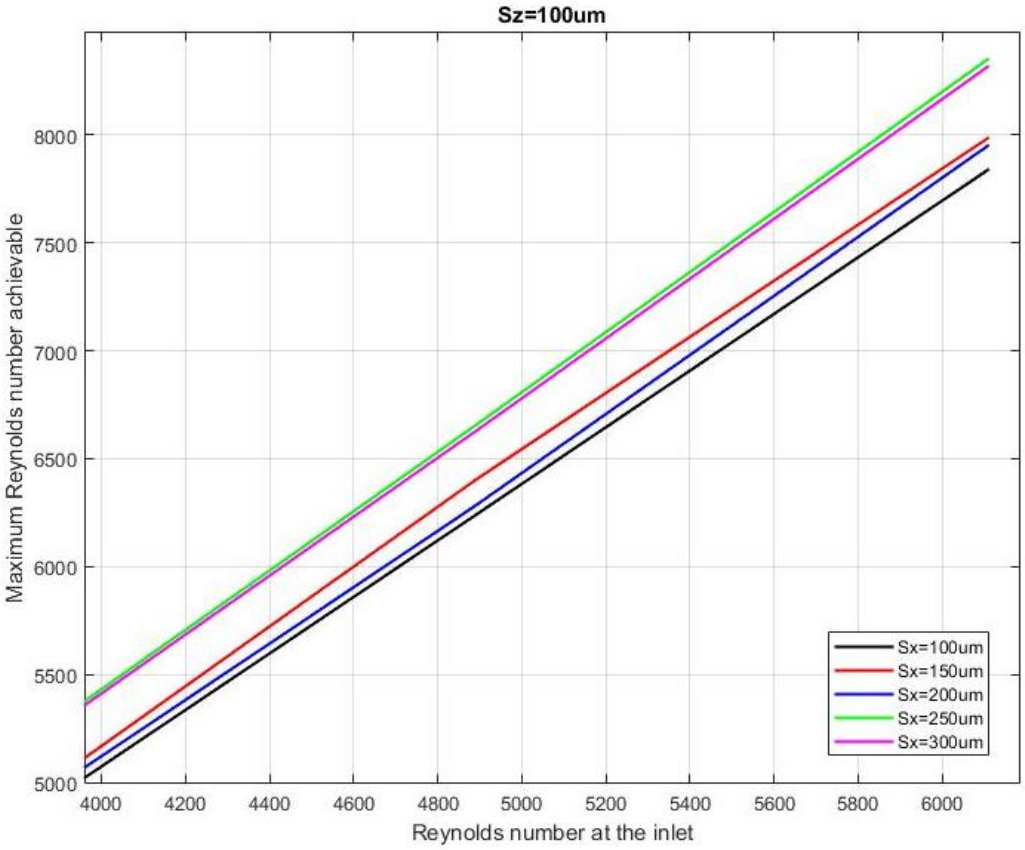

Figure 32. Figure 31 zoomed for higher velocities.

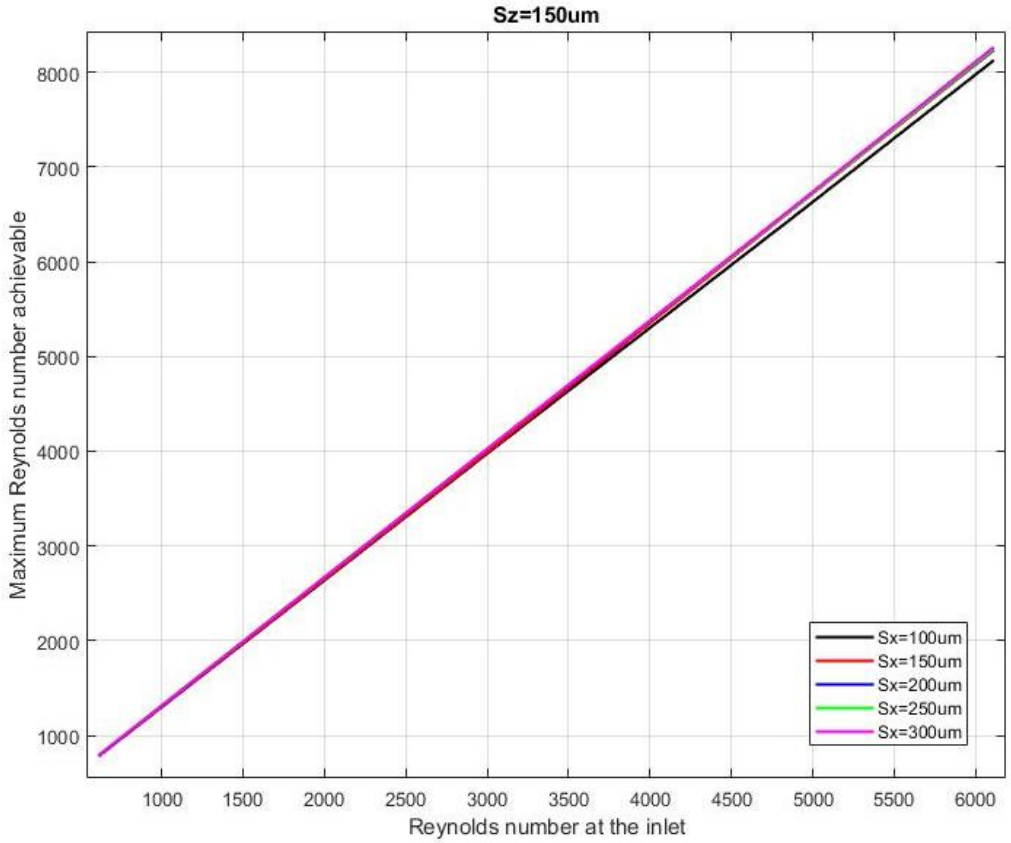

Figure 33. Comparison of 'maximum Re achievable vs inlet Re' for deferent distance values Sx under a constant Sz=150 μm

Figures 33 shows the same results as figure 31 but now the separation on the z direction was moved to 150um. Again, under the same Sz, a comparison between all the Sx evaluated distances was performed.

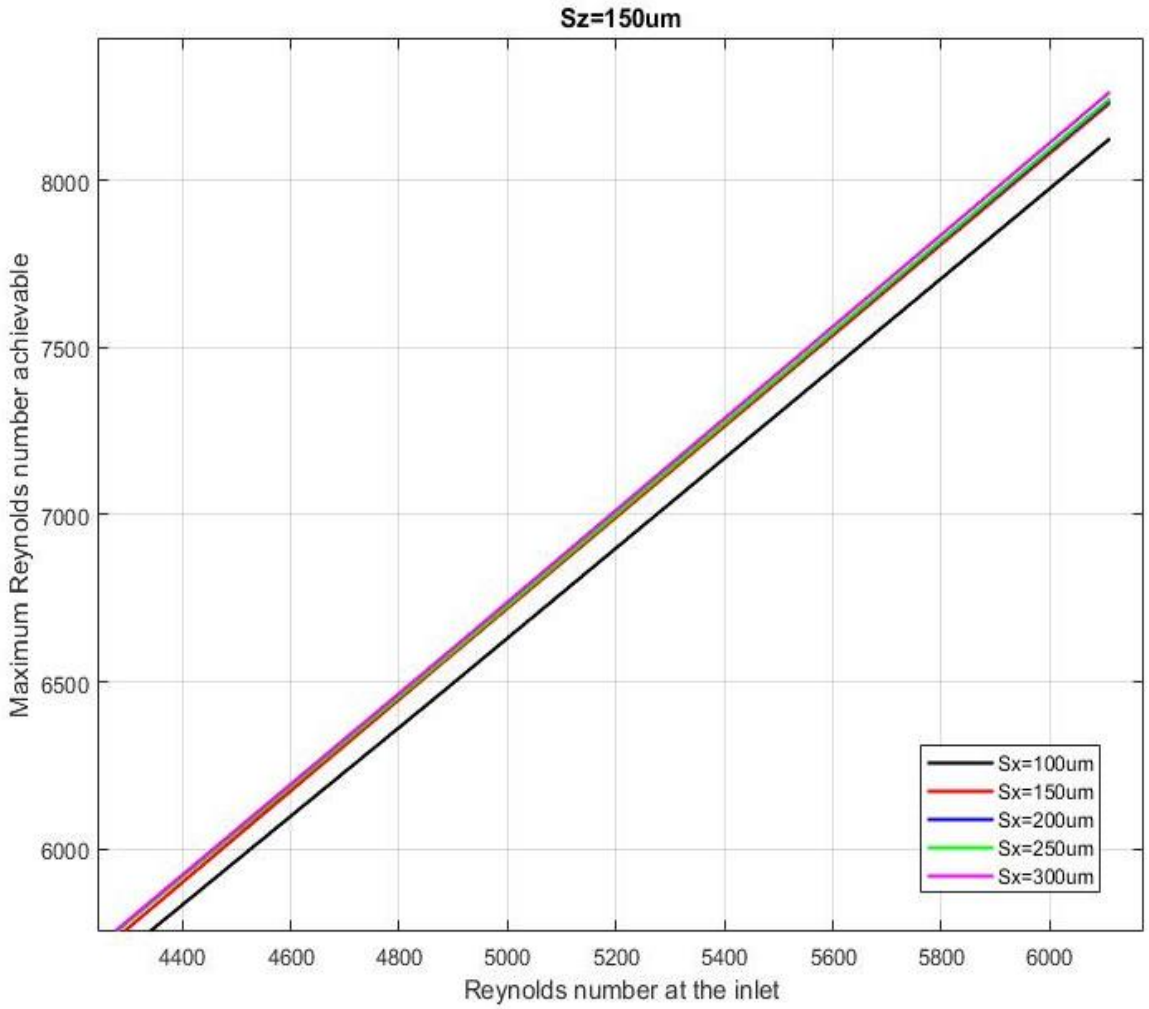

Figure 34. Figure 33 zoomed for higher velocities

Again, figure 33 just shows an overall result and the distinction between the different lines representing Sx outcomes becomes difficult. For this reason, figure 34 is included. On figure 34 the results for elevated velocities can be clearer identified.

Exactly the same procedure is followed in figure 35, an overall view is displayed but, in this case, the distance Sz is changed to 200 μm. One more time, figure 36 amplifies the area where the divergence between lines becomes more important. As in previous cases, this region coincides with larger velocities.

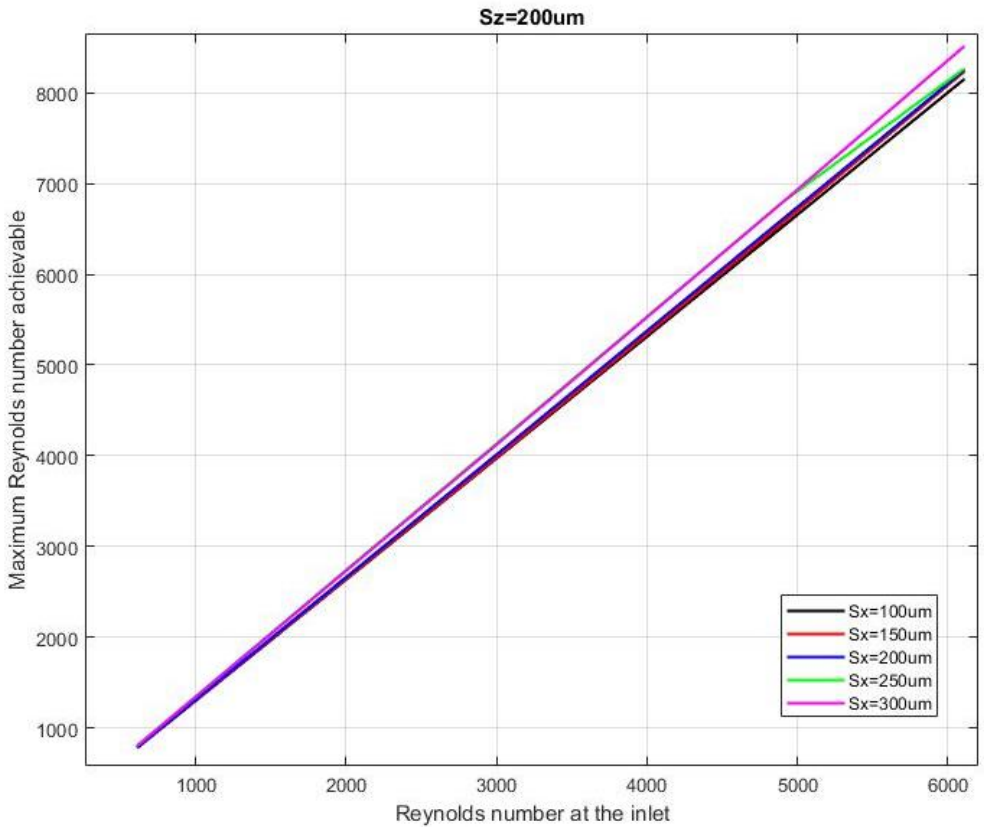

Figure 35. Comparison of 'maximum Re achievable vs inlet Re' for different distance values Sx under a constant Sz=200 μm

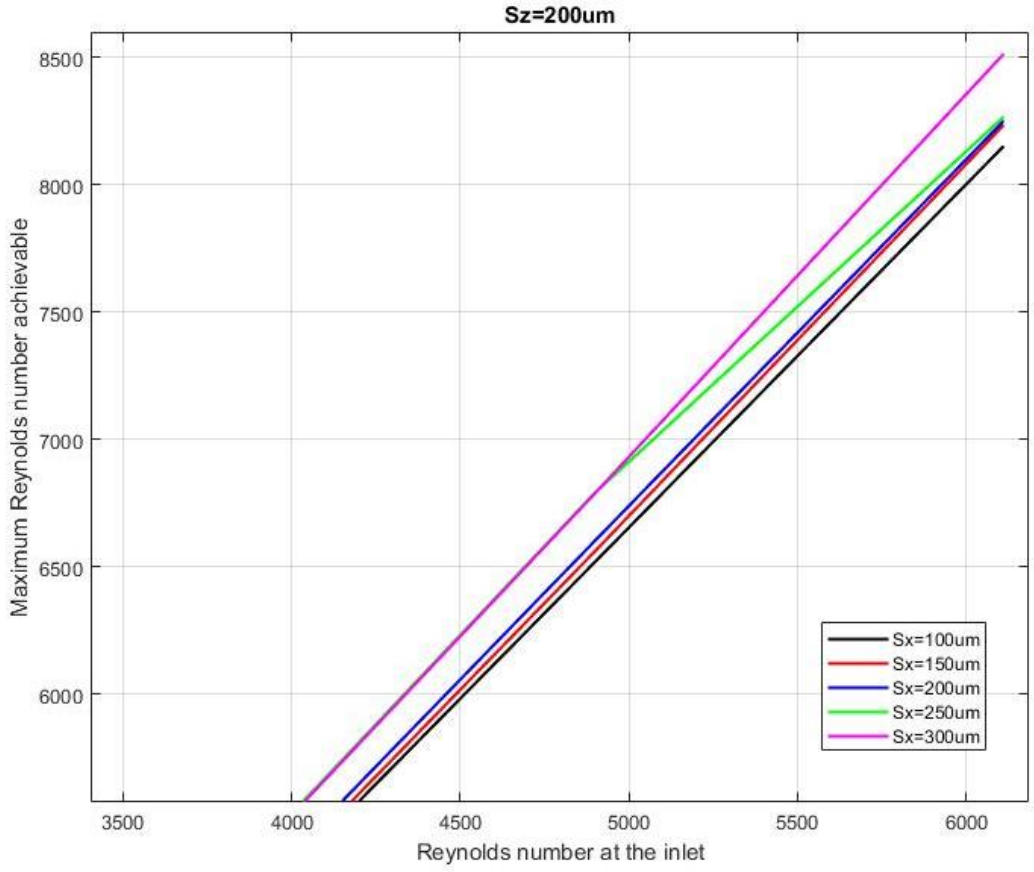

Figure 36. Figure 35 zoomed.

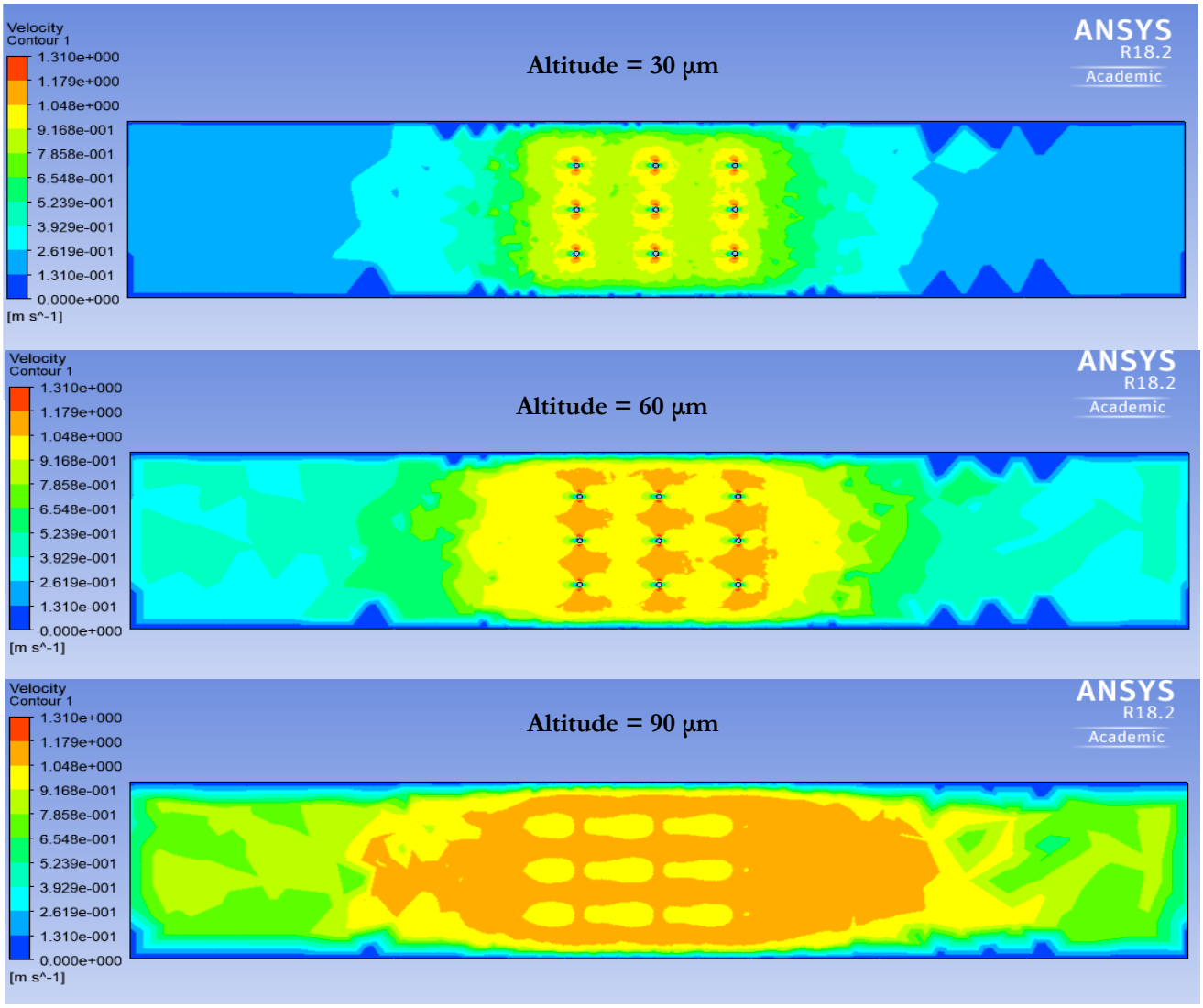

Figure 37. Set of nine columns (10x100 µm) Velocity contour evolution as height is increased

Figures 37 and 38 display the velocity contour of the fluid inside the channel seen from above. Captures were made from different altitudes. There, it can be analysed the areas where the flow is accelerated taking into account also de y-direction. Considering the bottom of the channel as 0um. These images represent altitudes of 30, 60, 90 µm in Figure 37 and 120, 200, 350 and 400 µm in Figure 38, starting from above.

It is also remarkable that, even though the reference axis is not shown, the fluid direction goes from right to left.

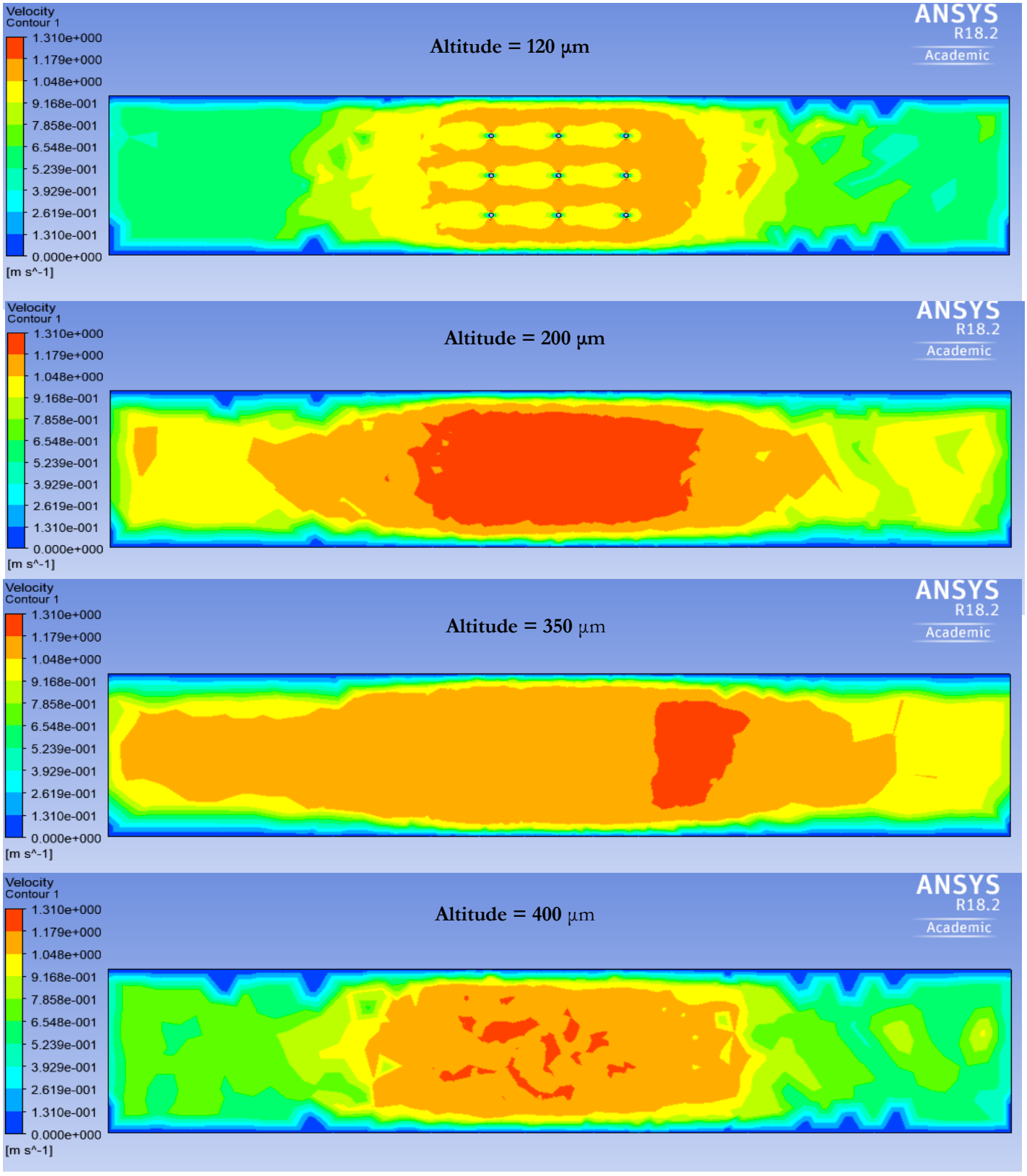

Figure 38. Velocity contour evolution as height is increased

4.2.2.1.1 Geometry optimization

As explained in section 3.1.3.2.1, different values for the height, thickness and width were assessed. The figure below shows how the fluid performance is affected by the flap height variation, under a constant width and thickness of 200 μm and 20 μm, respectively. It is perceptible that, for lower velocities, there is not any remarkable difference. However, as the inlet velocity is increased, it can be easily observed how the best performance is obtained with a height of 200 μm. The maximum achievable Reynolds number is reduced as so does the height if the flap (Figure 39).

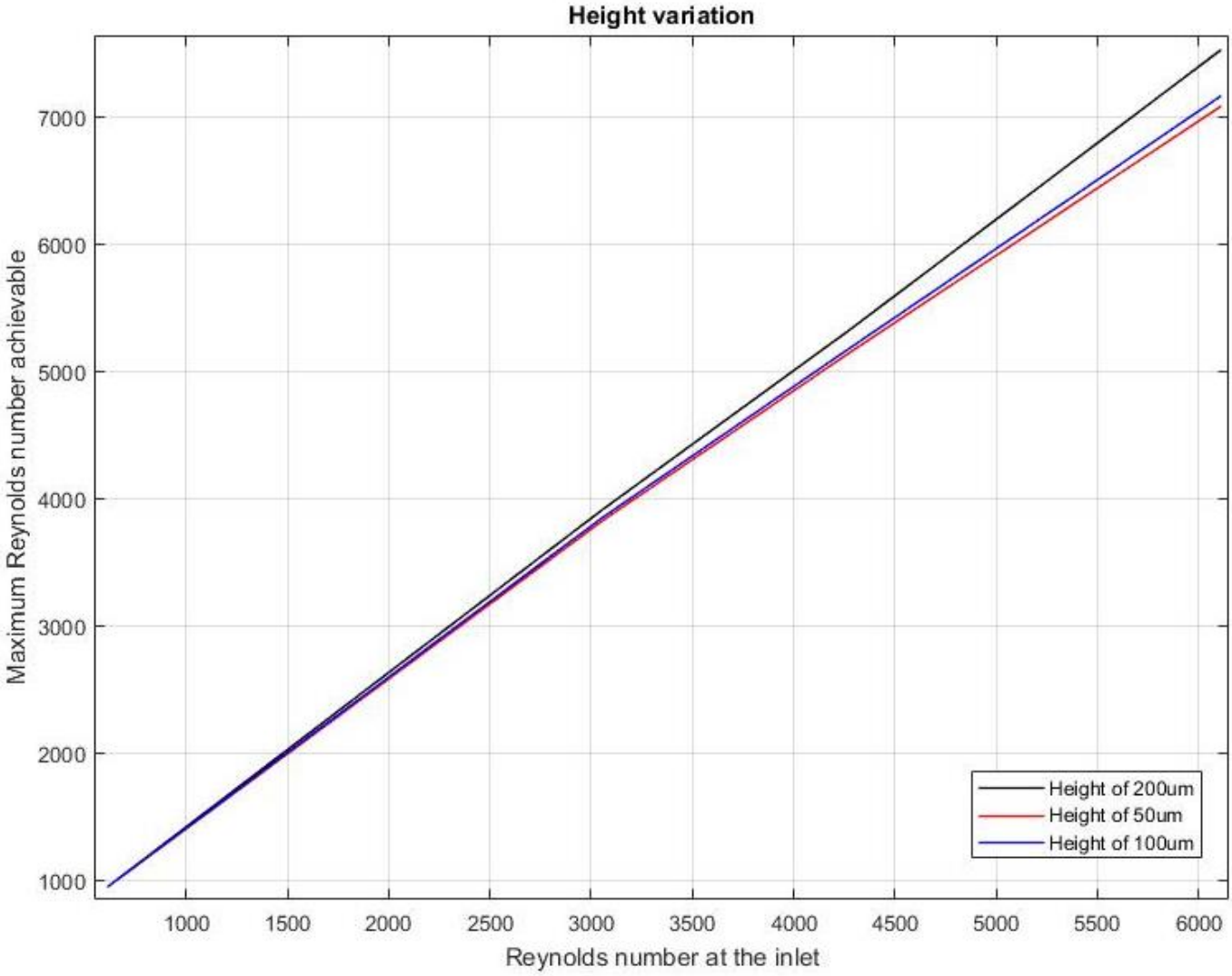

Figure 39. Height influence on the maximum achievable Reynolds number.

In the graph below (Figure 40), it can be seen how the variation in thickness does not cause significant changes in the fluid performance. Figure 42 amplifies the results for higher velocities since that is the area where some variations can be slightly perceived. Although there are not significant differences, smaller thicknesses seem to obtain a lightly better behaviour.

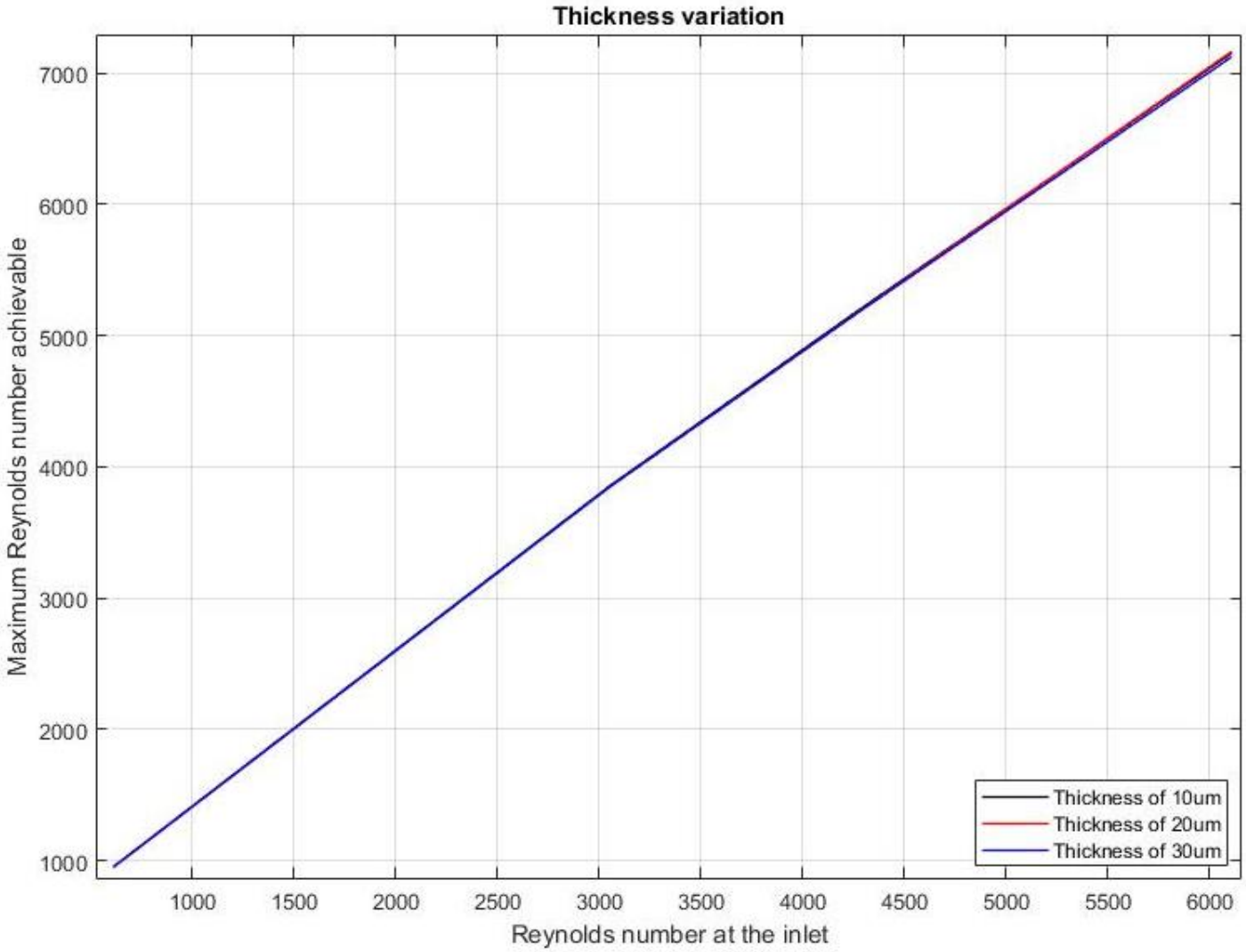

Figure 40.Thickness influence in maximum Re achievable.

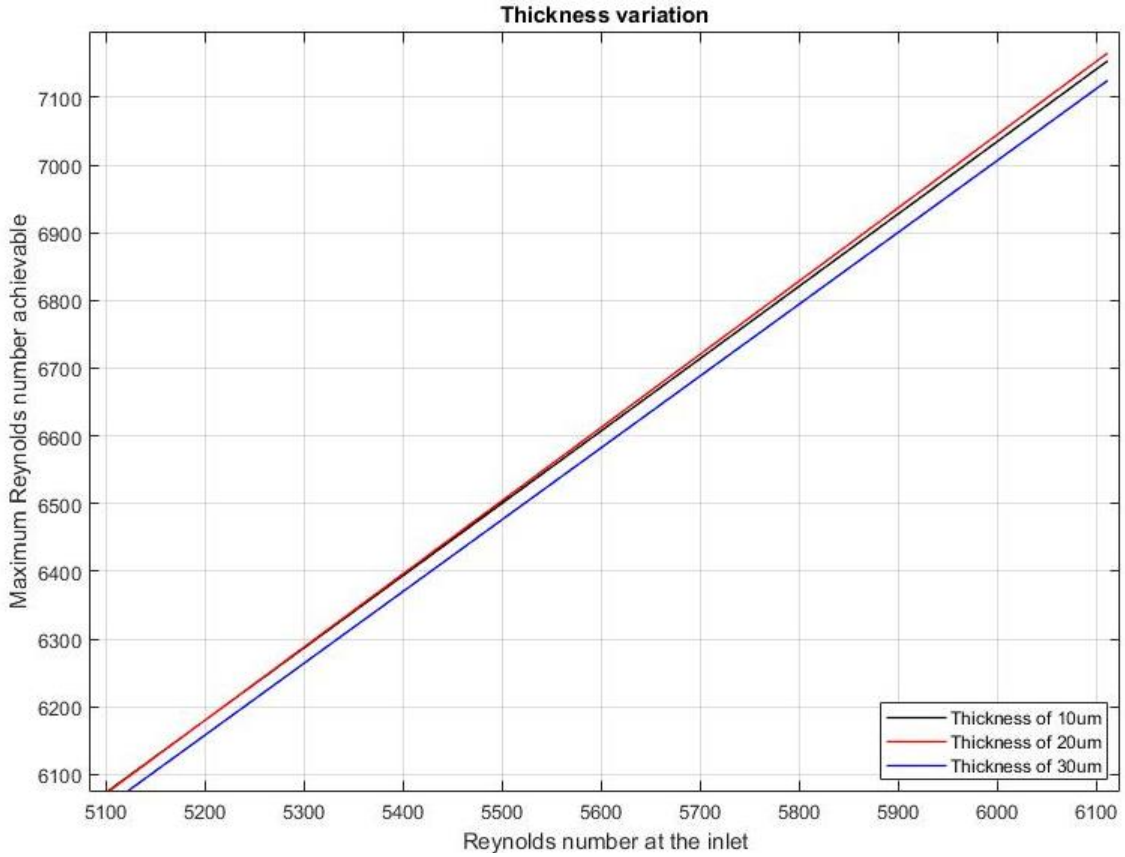

Figure 42. Thickness influence in maximum Re achievable (zoomed in)

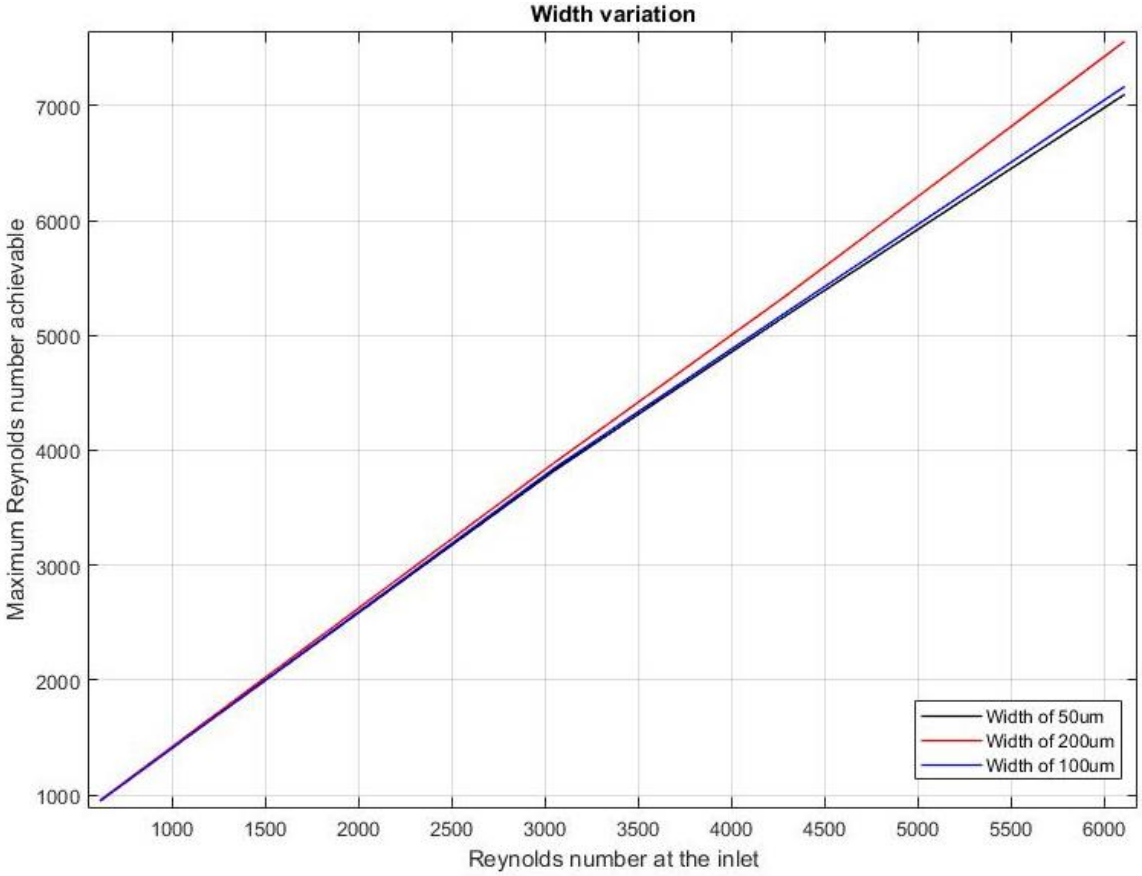

Figure 41. Width influence in maximum Re achievable

The graph shown above (Figure 41) displays the maximum Reynolds achievable for different analysed flap widths. As it was previously stated, the height and the thickness remained now constant with values of 100 μm and 20 μm, respectively. It can be clearly observed how the width that optimizes the fluid is the largest one. As the width is decreased, the performance also gets lower values.

From previous results it can be said that the parameters that had a highest influence in the fluid behaviour are the flap height and width. As seen in figures 40 and 42, the thickness does not cause a high impact on the fluid performance. Due to this fact, the influence of varying height and width simultaneously was analysed and displayed in figure 43. As it was expected, the most optimal combination is obtained by using a value of 200 μm for both, height and width. These magnitudes correspond with the largest assessed values. The thickness remained unchanged with a value of 20 μm.

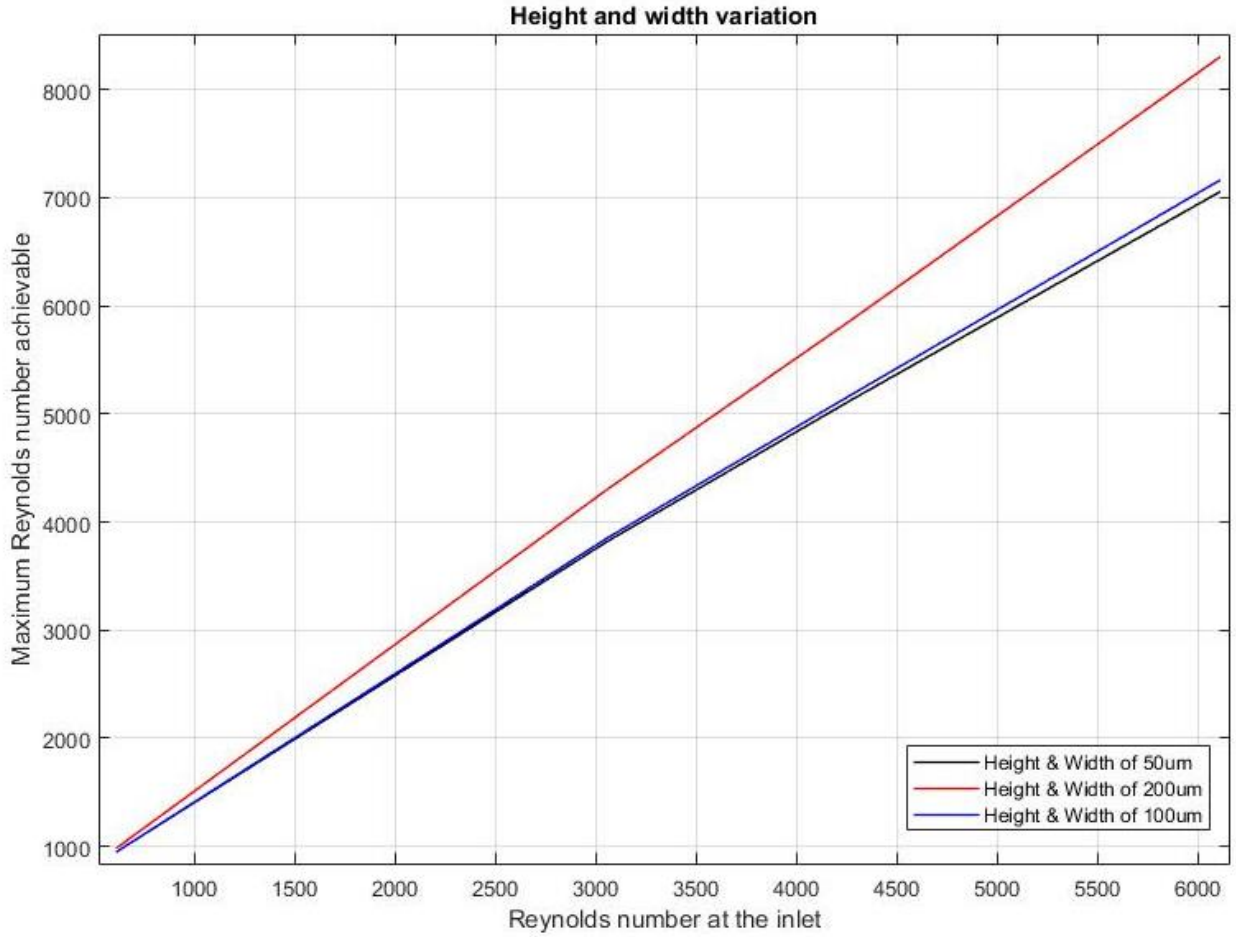

Figure 43. Maximum Re achievable variation due height and width.

Among the analysed set of parameters, the geometry that optimizes the results is 200 μm high, has a width of 200 μm and its thickness is 20 μm. This was the selected combination and it will be analysed in the next section, together with other eight identical flaps, in order to obtain the best most optimal flaps distribution.

4.2.2.1.2 Separation optimization

As it was explained before, the next step was to optimize the separation between a set of 9 identical flaps. The flap dimensions used were selected from the previous section, where the most optimal flap configuration was chosen. Under a constant value for Sz (crosswise separation), different values for Sx (longitudinal distance between flaps) were evaluated. This process was repeated for three different values of Sz.

The image below (Figure 44) shows the variation of maximum Reynolds number regarding three different values of Sx, under a constant Sz equal to 50 μm. It can be observed that there is not any perceptible difference between different values of Sx.

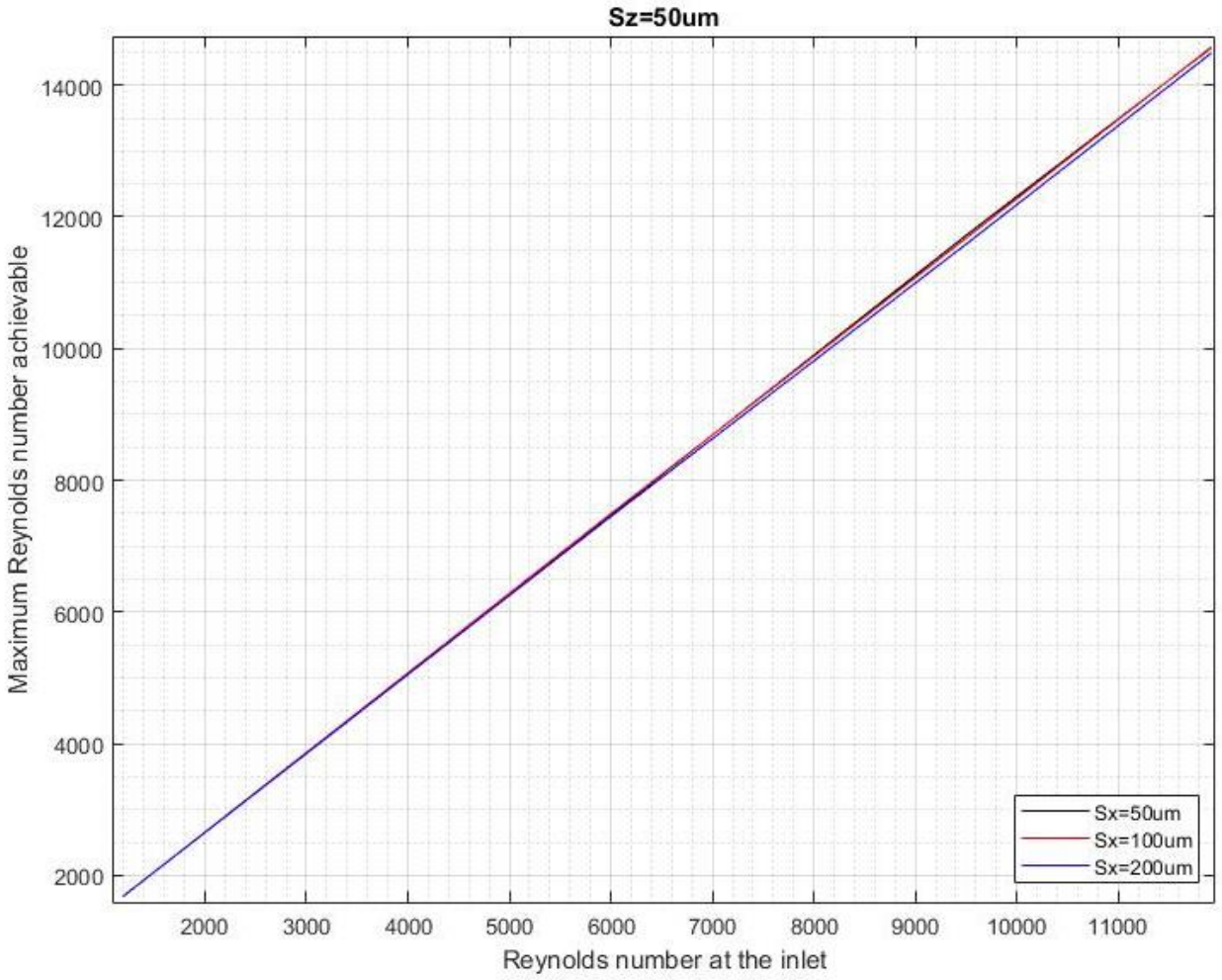

Figure 44. Comparison of maximum Re vs inlet Re for different values of Sx.

The same behaviour is seen in figure 45, for a constant Sz of 100 μm. However, zooming in for higher velocities (Figure 46), it is perceptible how larger values for Sx obtain slightly greater Reynolds numbers.

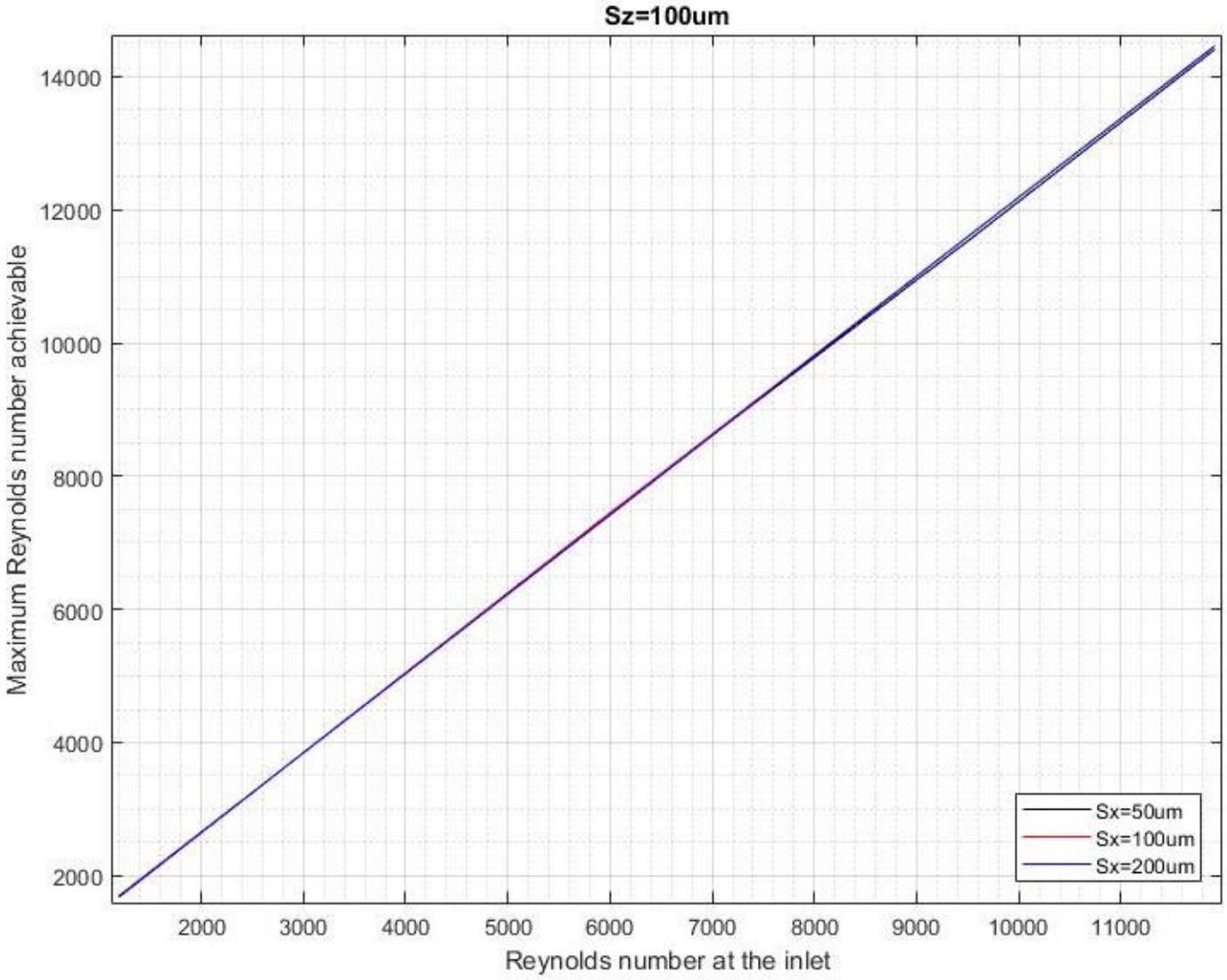

Figure 45. Comparison of maximum Re vs inlet Re for different values of Sx.

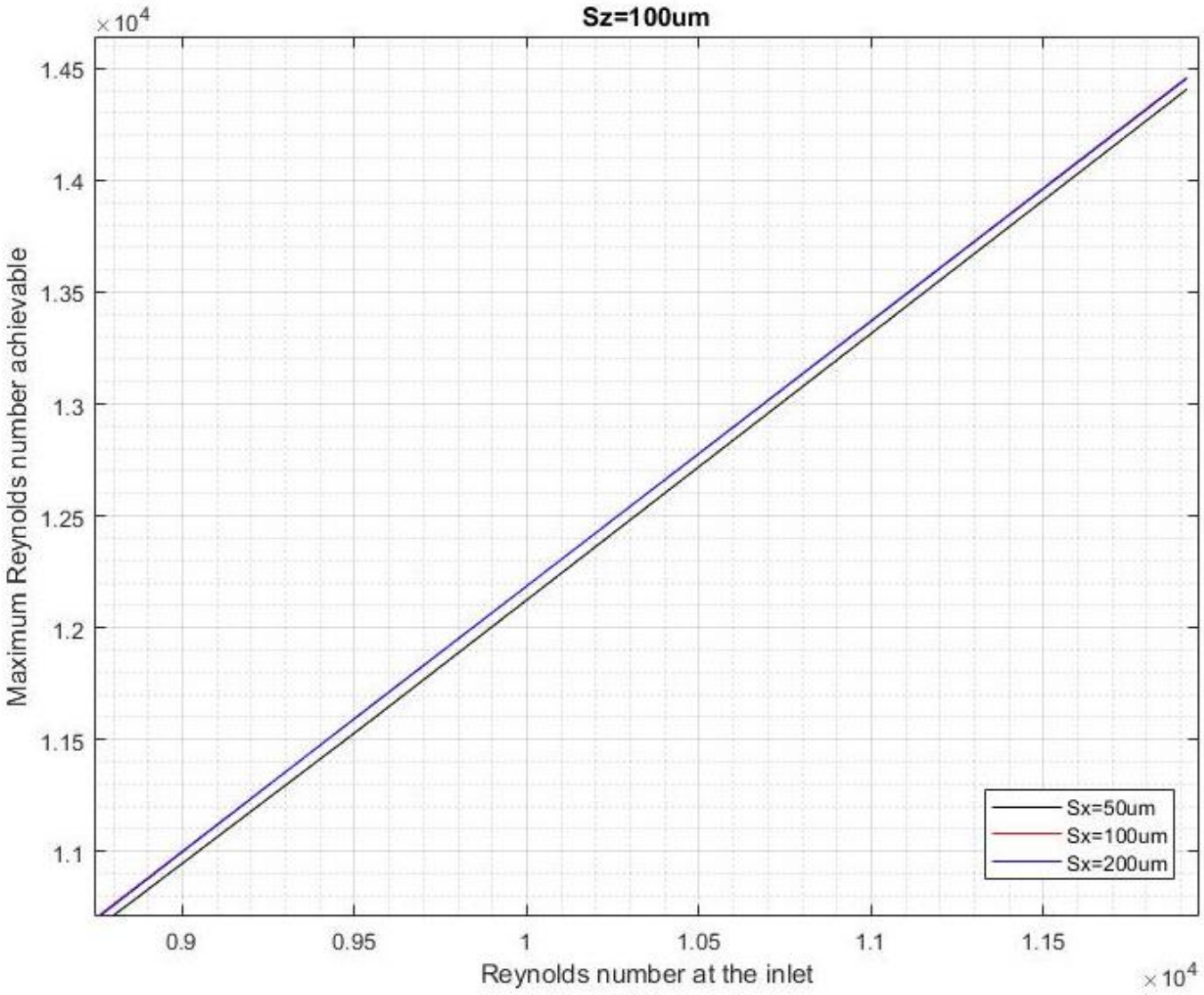

Figure 46. Comparison of maximum Re vs inlet Re for different values of Sx. (zoomed in for higher velocities)

Finally Sz=200 μm is analysed. Although for lower inlet velocities there is not any noticeable variation among different Sx, the difference becomes clearer for larger input velocities. The biggest value for the longitudinal separation among flaps (Sx=200 μm) achieved the largest achievable Re number (Figure 47).

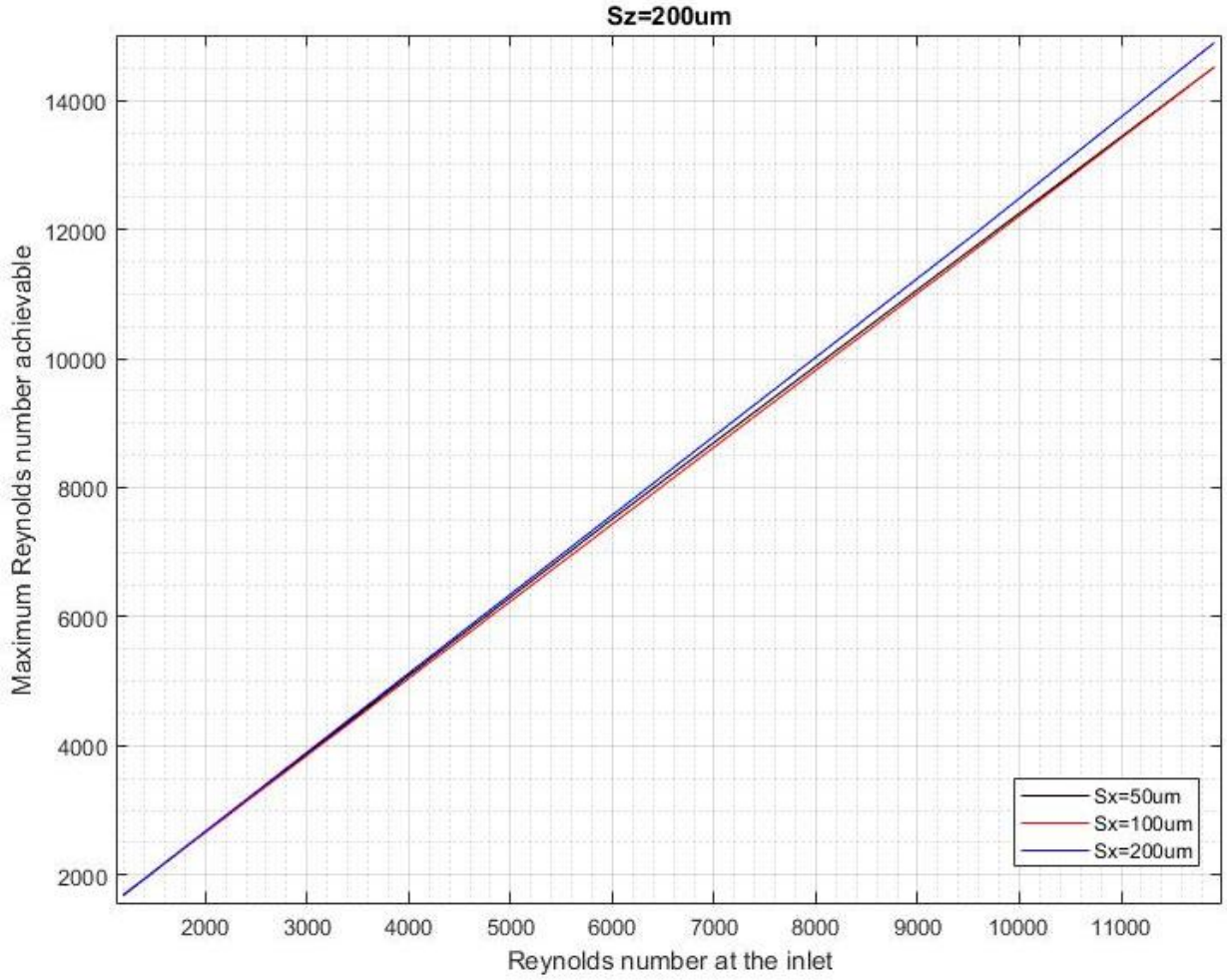

Figure 47. Comparison of maximum Re vs inlet Re for different values of Sx.

This dissimilarity can be clearer observed in figure 48 where the result in amplified for larger inlet velocities, that is the region where the differences become more noticeable. This combination, Sx=200 μm and Sz=200 μm, is the one achieving the best performance. Regarding the results obtained along this section, it can be appreciated how the fluid performance is increases as the separation between flaps is augmented.

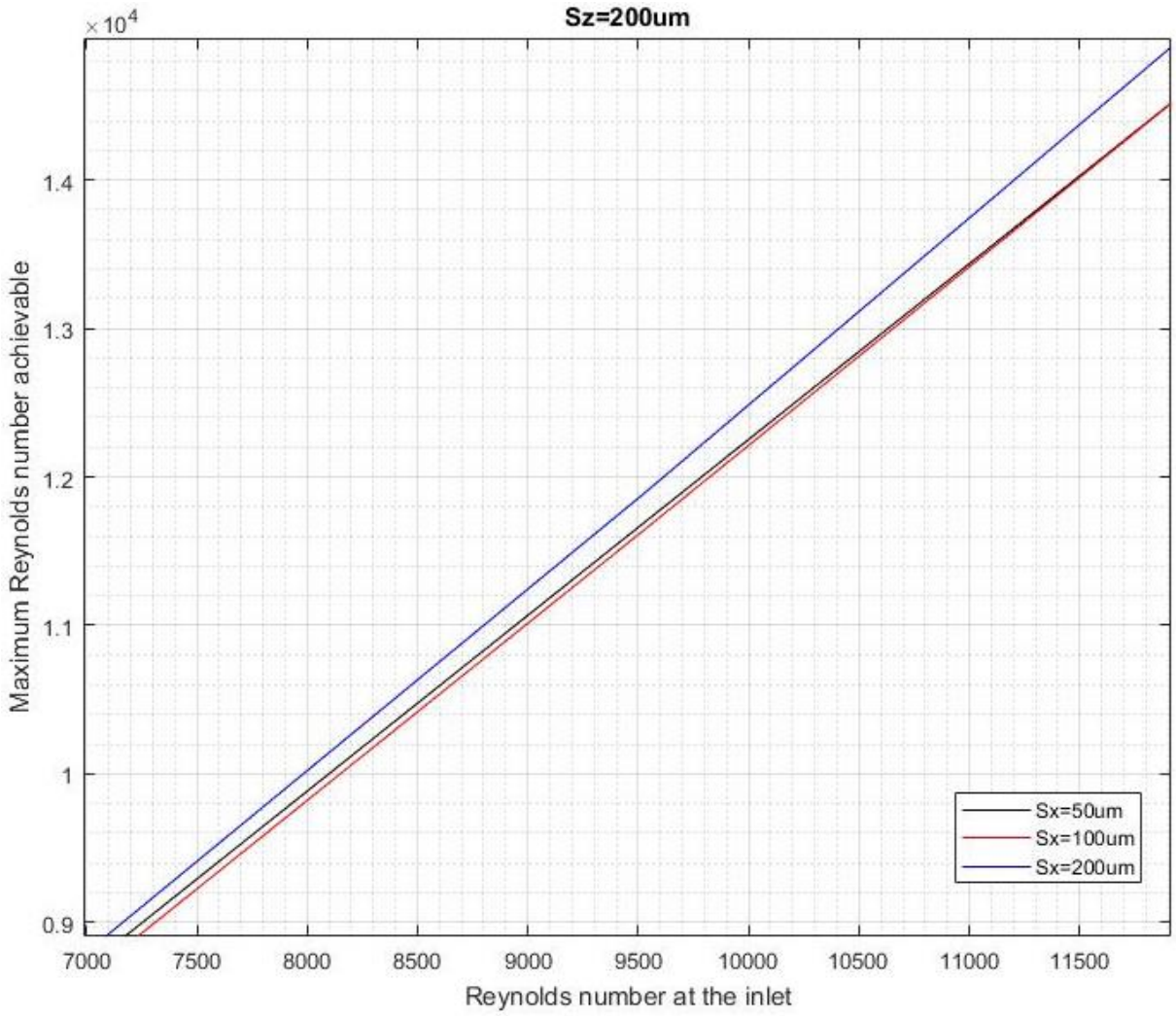

Figure 48. Comparison of maximum Re vs inlet Re for different values of Sx. (zoomed in)

4.2.2.1.3 Corners' shape

As discussed in '3.1.3.2.1', the last parameter optimized, regarding the geometry, was the shape of the flaps' corner. Using the best combination of flap dimensions and separation between flaps previously selected, three options were assessed: 90º, rounded corner with a radius equal to half the flap width and a rounded corner with a radius equal to quarter the flap width.

In figure 49 and 50 it is observed how the most optimal shape is using a 90º corner angle. As a clarification, the dimensions of the evaluated flaps are 200 μm high, width of 200 μm and thickness equal to 20 μm. The separations between them is Sx=200 μm and Sz=200 μm.

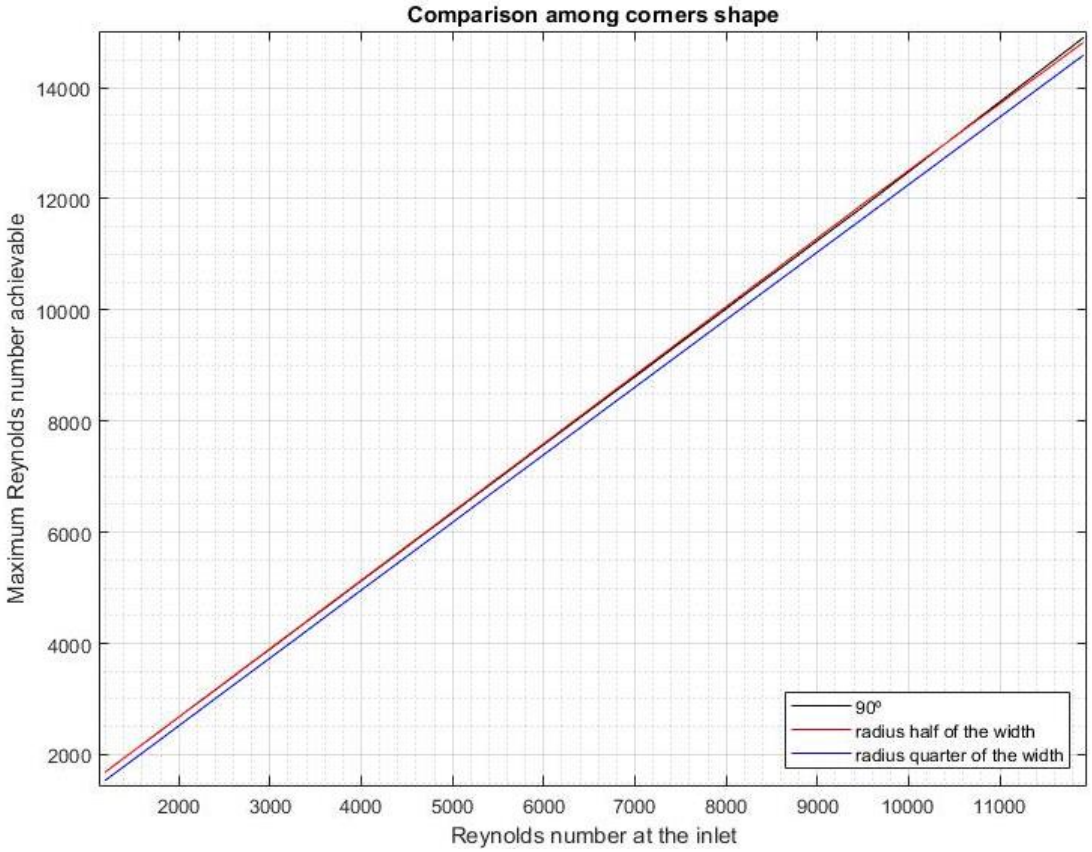

Figure 50. Comparison between different corners shapes.

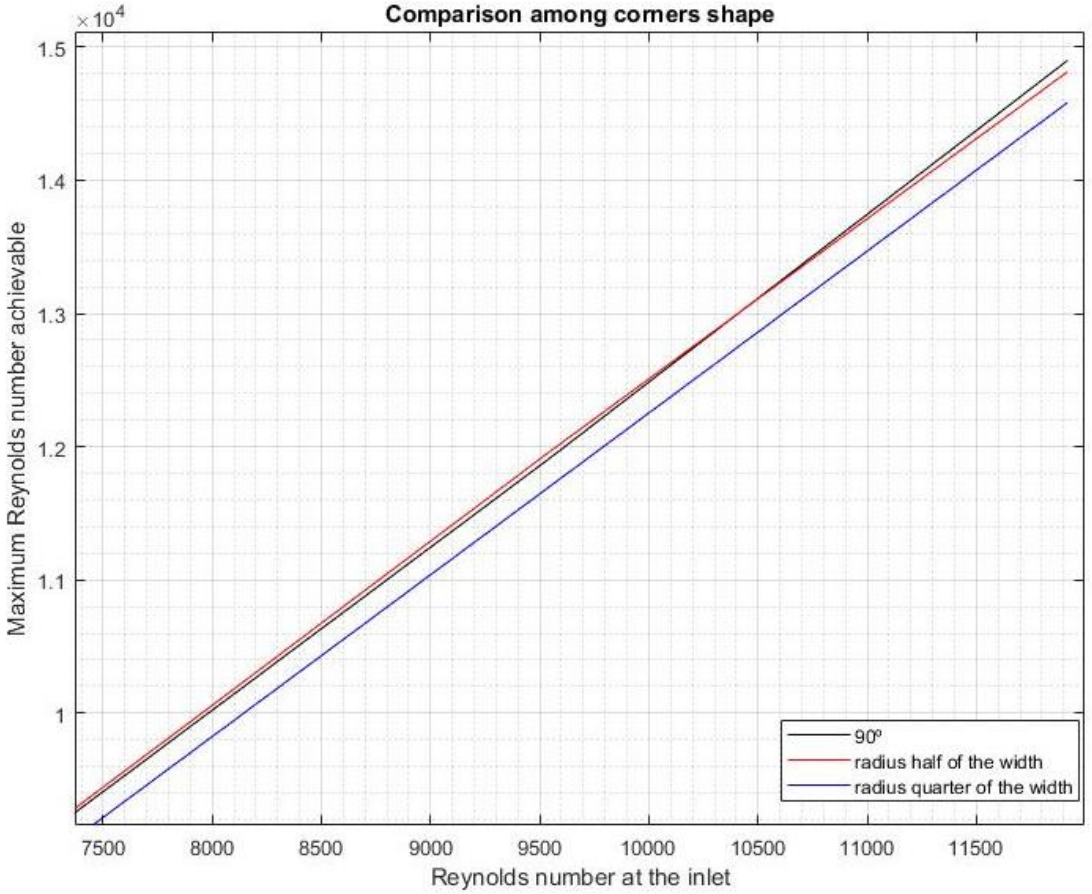

Figure 49. Comparison between different corners shapes. (Zoomed in)

4.2.2.2 Macroflaps

4.2.2.2.1 Geometry optimization

The followed procedure is identical to the previous one but increasing the order of magnitude from micrometres to millimetres. Also the shape of the working channel was modified in order to perform a more realistic comparison between experimental and simulated results. Again different combinations of flap dimensions were analysed.

The figure below (Figure 51) shows the height influence on the maximum achievable Re while keeping the thickness and width constants and equal to 0.5 mm and 10 mm, respectively. It is clearly perceptible that the best performance is obtained with the maximum analysed height.

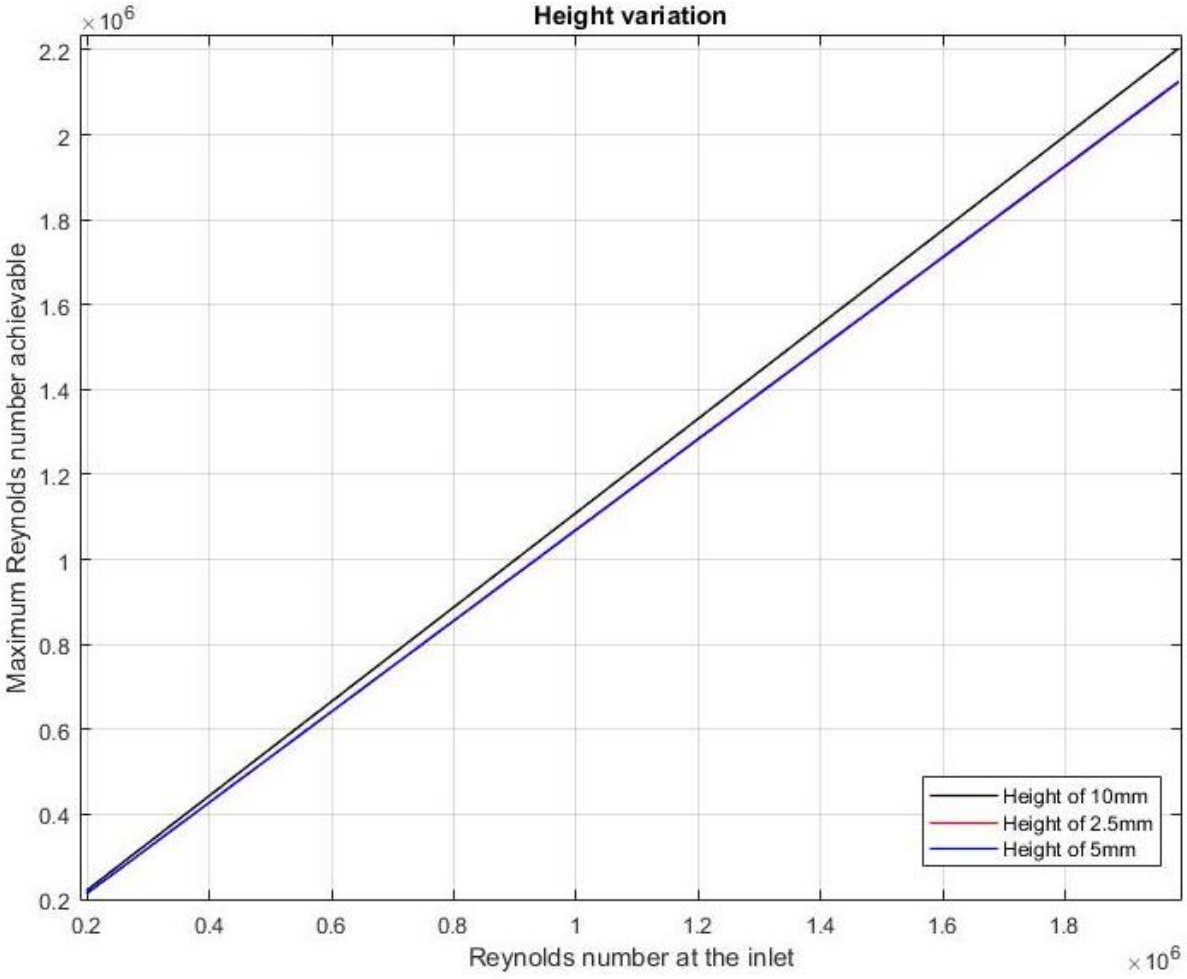

Figure 51. Height variation influence in maximum Re achievable.

When setting height and the thickness at constant values of 5mm and 0.5mm, respectively, the width influence can be observed. This effect is displayed in figure 52. Again, the most optimal width is the largest one, i.e. 20mm.

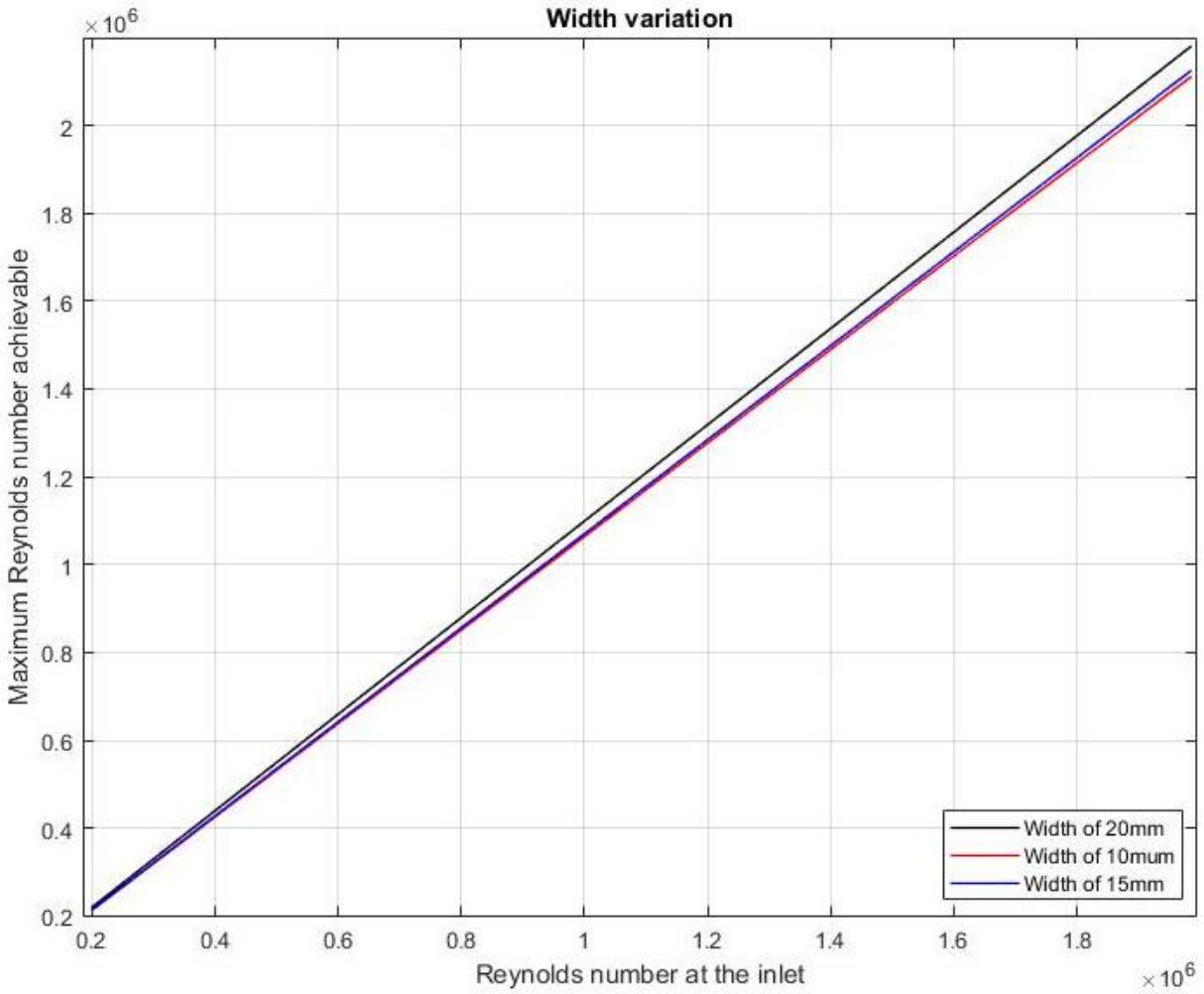

Figure 52. Width variation influence in maximum Re achievable.

Finally the thickness is evaluated. As seen in figure 53, the thickness variation does not have any perceptible influence in the fluid behaviour. Therefore, the parameters which have the highest impact of the fluid performance are the height and the width. The most optimal results were obtained using the highest dimensions assessed.

Regarding the preceding results, the dimensions selected to continue with the optimization process are a width of 20mm, a height of 10mm and a thickness of 1 mm.

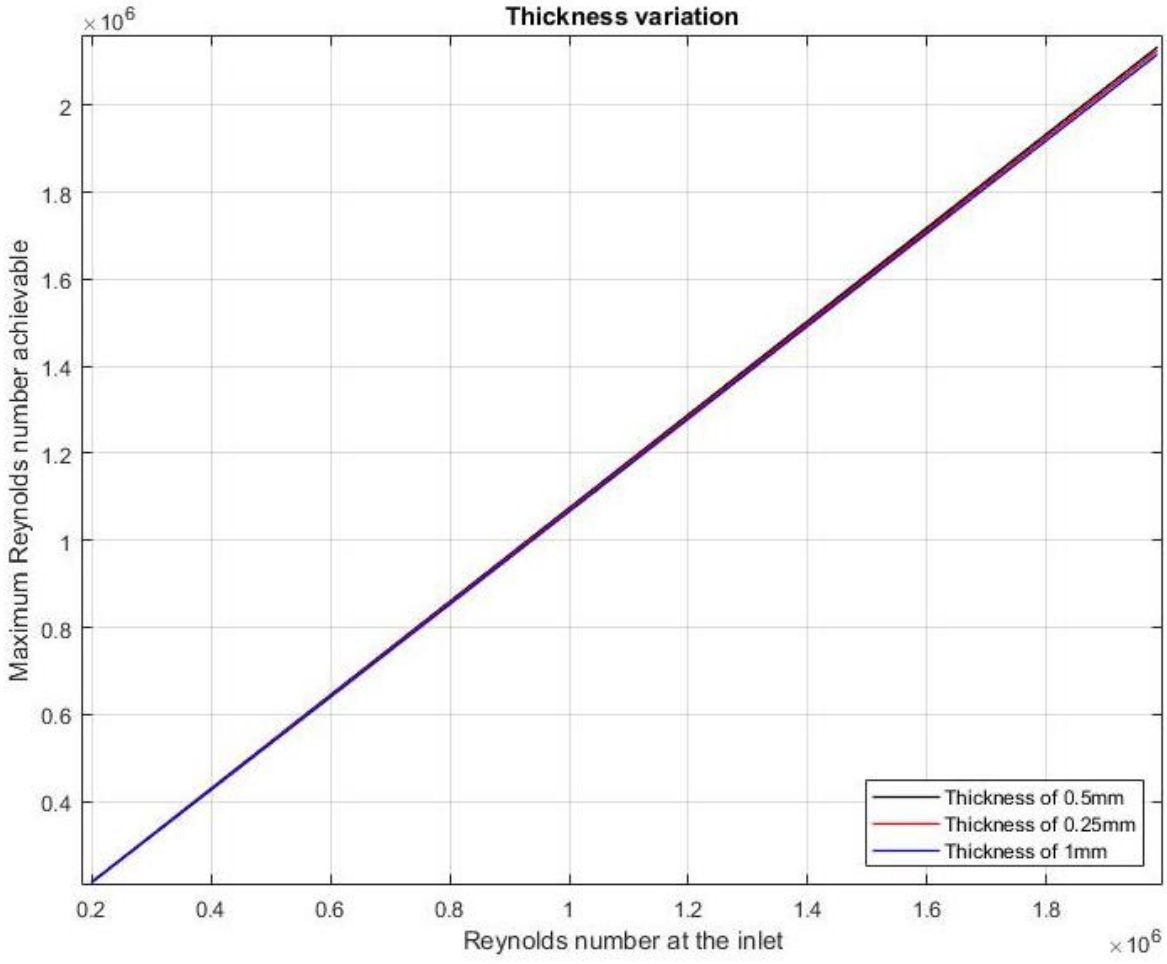

Figure 53.Thickness variation influence in maximum Re achievable.

4.2.2.2.2 Separation optimization

Following the same procedure as with the microflap, the best configuration selected from the preceding section is analysed together with other eight identical flaps. The aim is to figure out which is the best flaps disposition in order to obtain the best fluid performance.

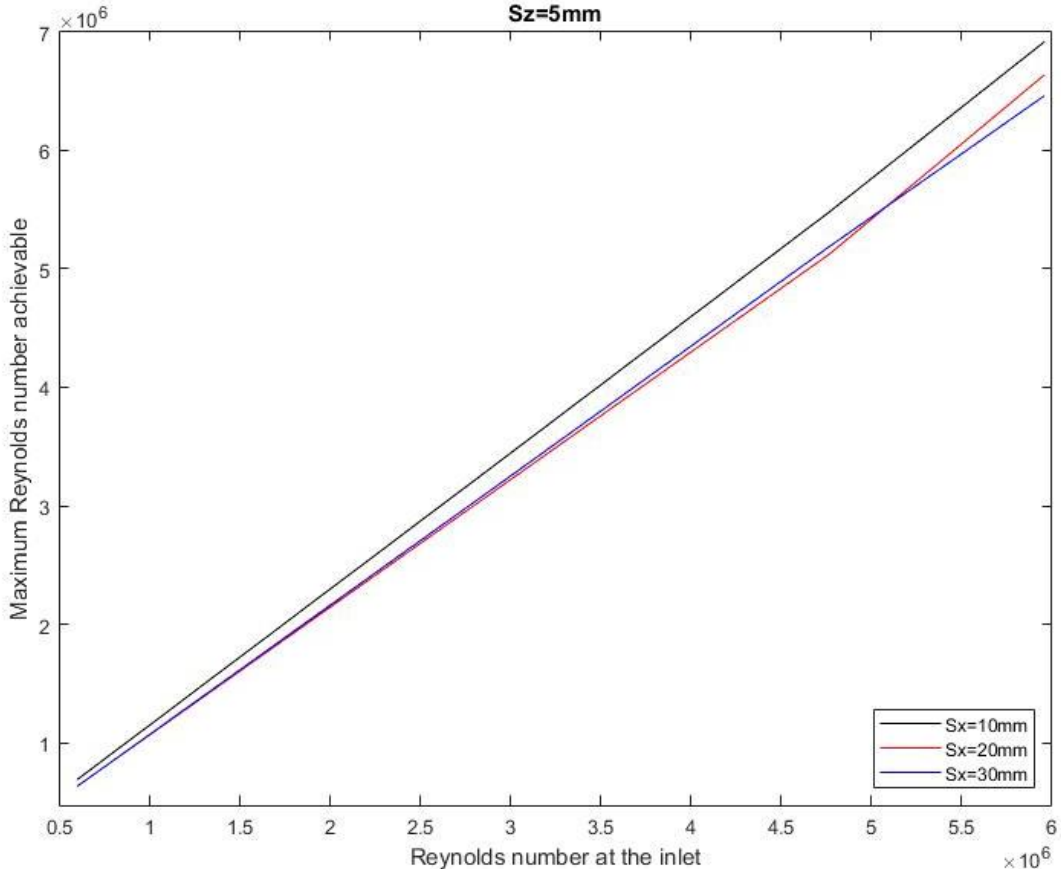

Figure 55. Sx influence on Re under constant Sz=5mm

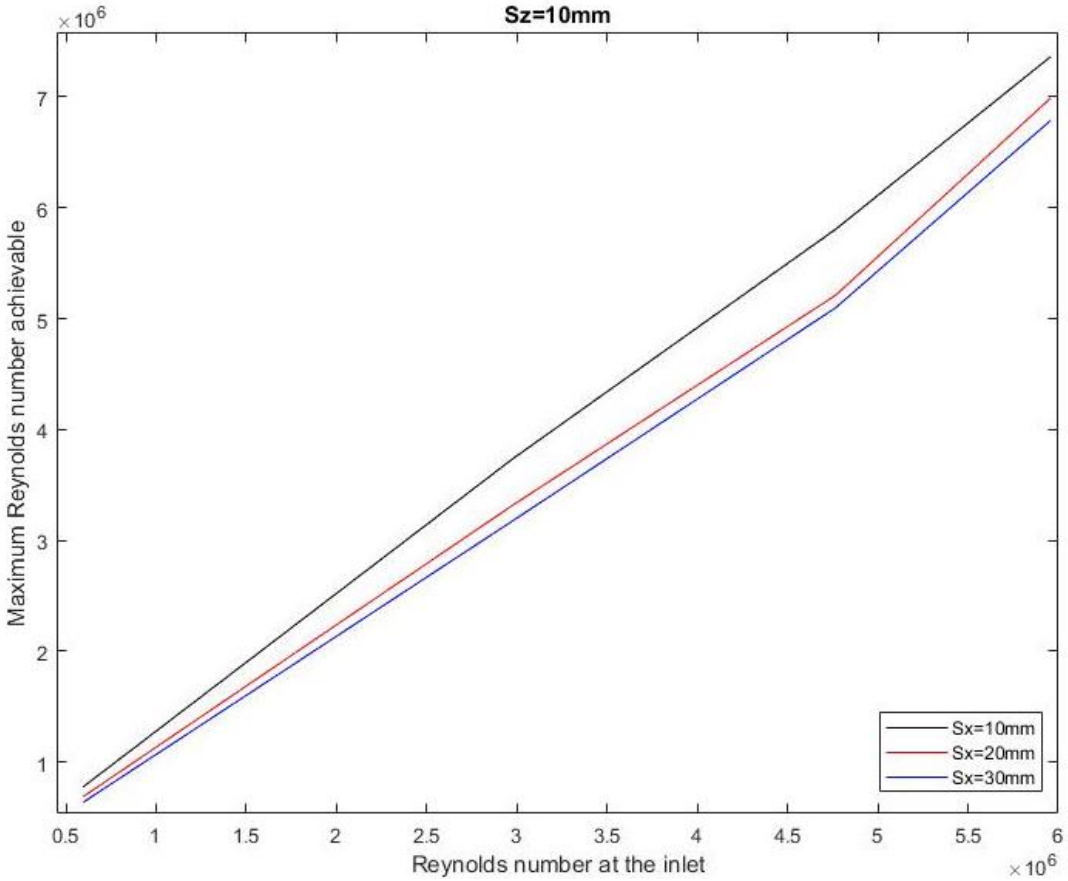

Figure 54. Sx influence on Re under constant Sz=10mm

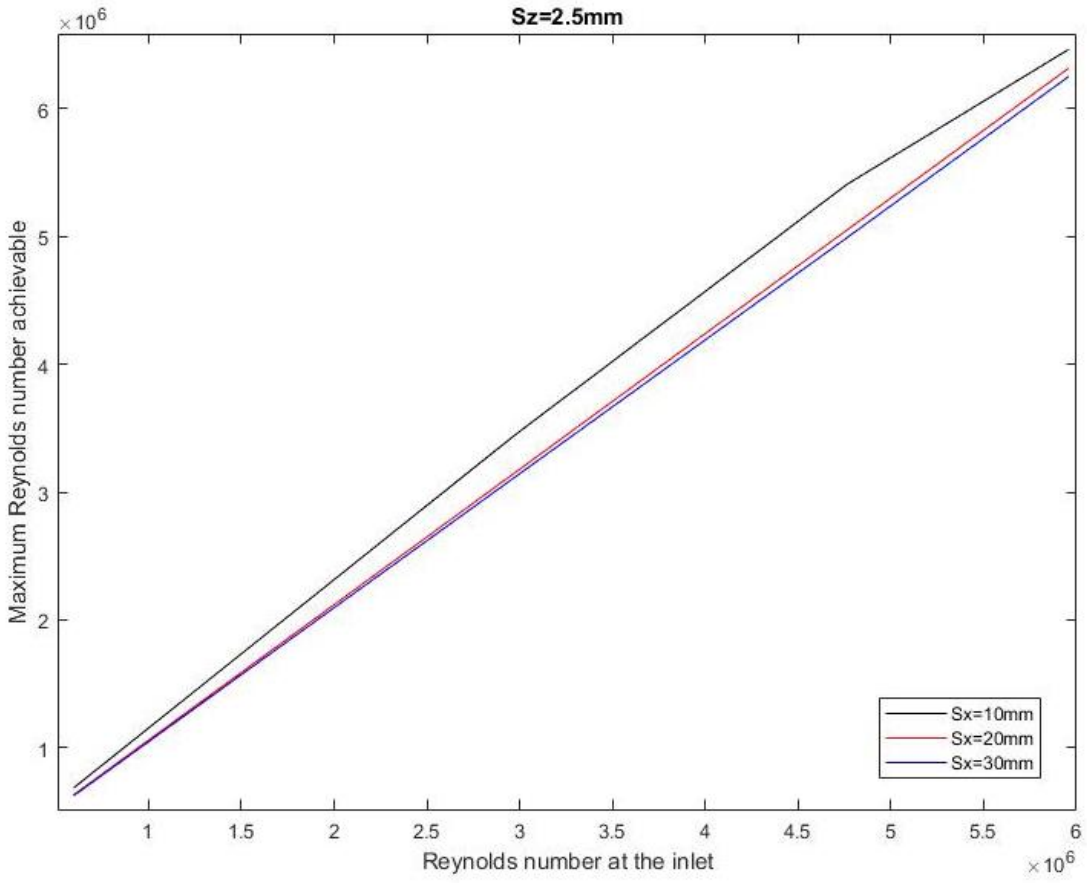

Figure 56. Sx influence on Re under constant Sz=2.5mm

From figures 54, 55 and 56 it can be seen that, in general, best results are obtained for larger values of Sz but together with smaller Sx. That is, the performance is increased when Sz is augmented but it decreases as Sx growths. Therefore, from the graphs above, the most optimal configuration among the analysed data is given by a longitudinal separation (Sx) of 10mm and a crosswise distance (Sz) of 10mm.

4.2.2.2.3 Corners' shape

Lastly, the corner's shape is assessed. From figure 57, it can be observed that, as in the previous case, the most optimal design is using squared corners with a 90º angle.

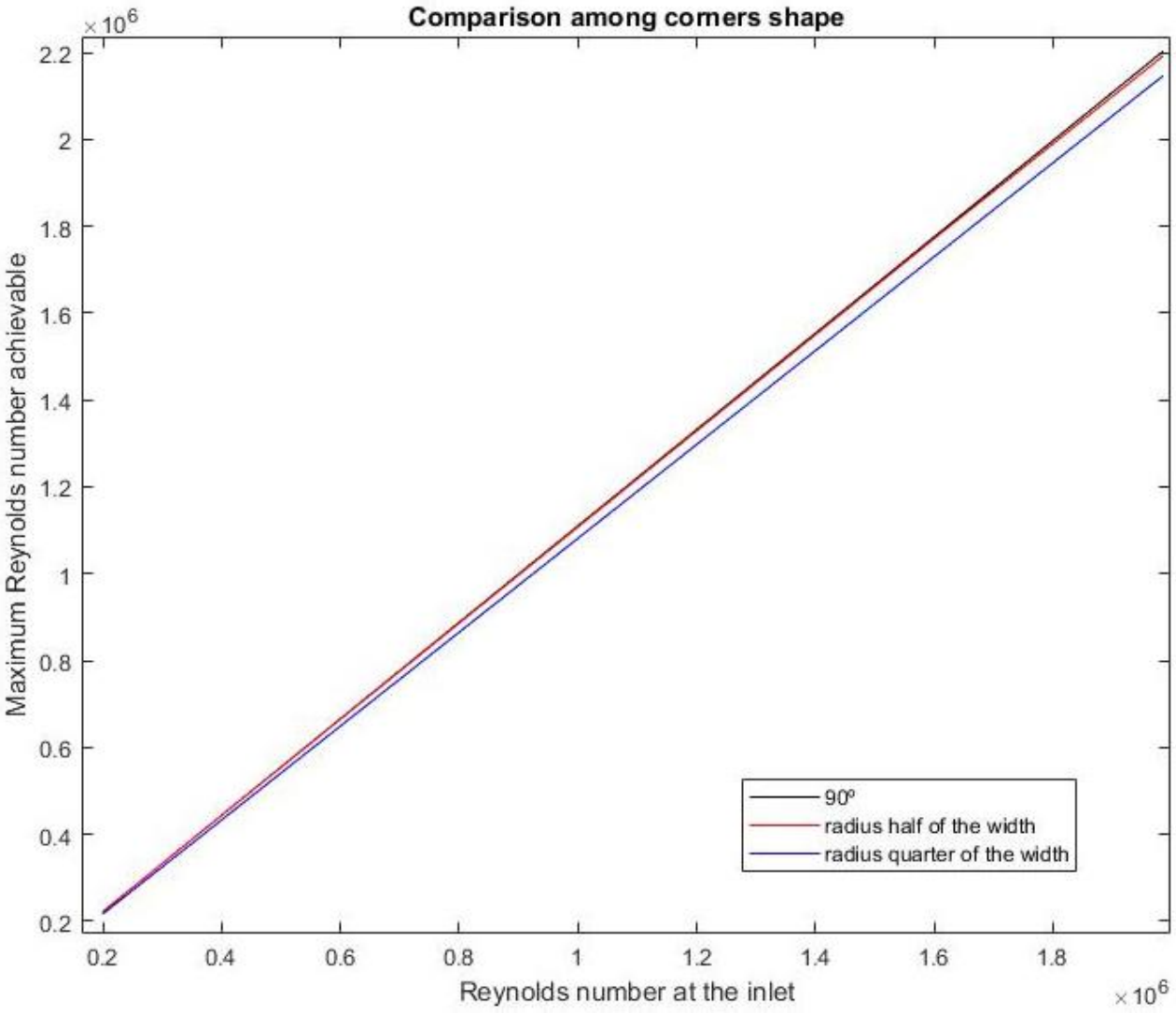

Figure 57. Corner's shape influence on Re.

4.2.3 Artificial roughness

4.2.3.1 Microflap

As explained, two different types of elements were analysed; conic and cylindrical elements. For the cones, a distinction was made between α=30º and α=40º. The results from this study are plotted below.

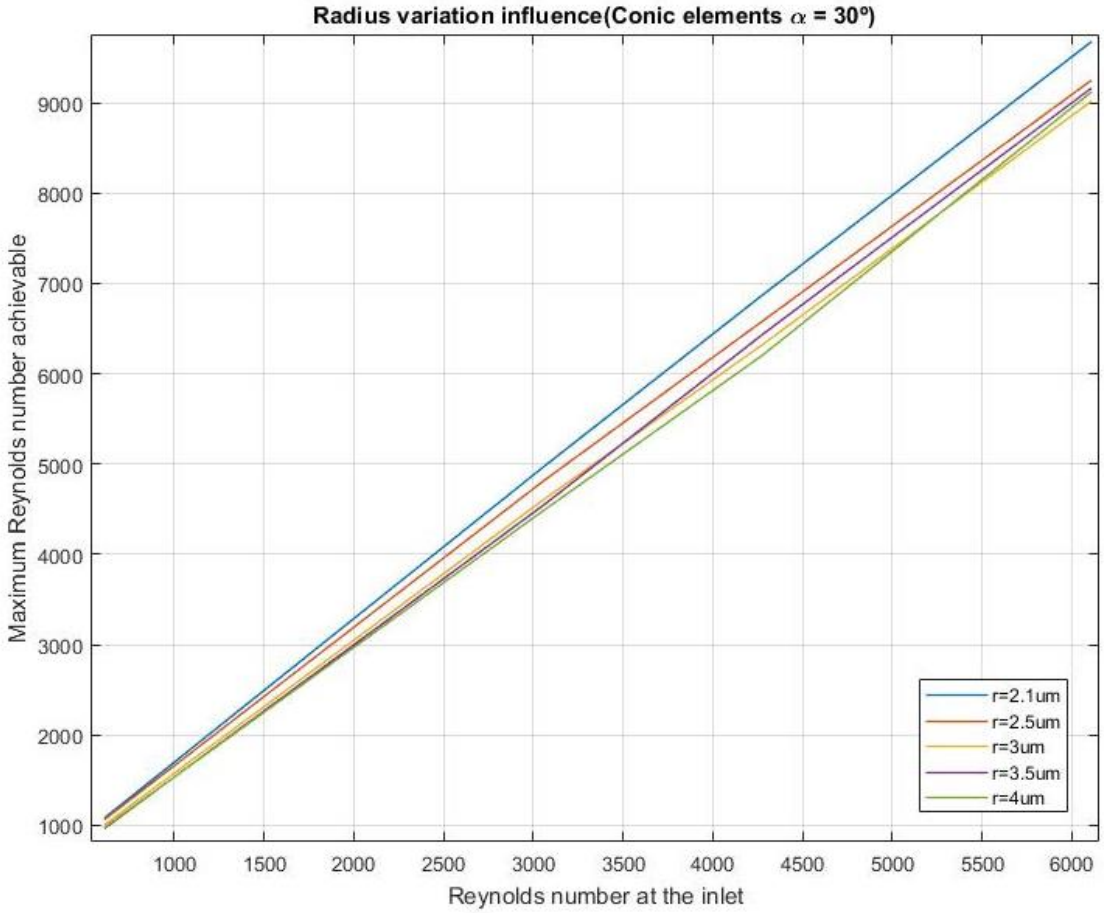

Figure 58. Radius influence on maximum Re for conic elements with α=30º

From figures 58, 59 and 60 it can be easily seen that the most optimal results are obtained with the lowest radius, for all the assessed cases. By comparing all the figures together, the best performance is obtained with a conic element (α=30º) and a radius of 2.1 μm.

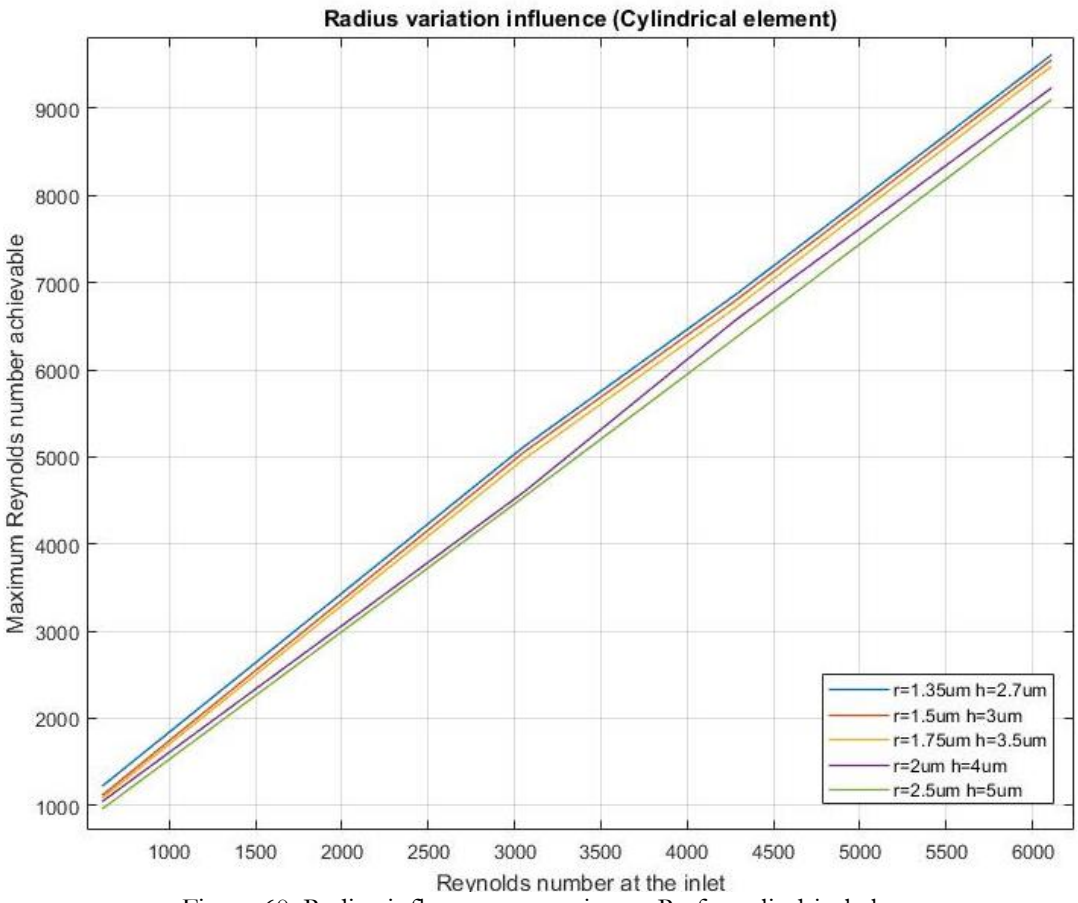

Figure 60. Radius influence on maximum Re for cylindrical elements

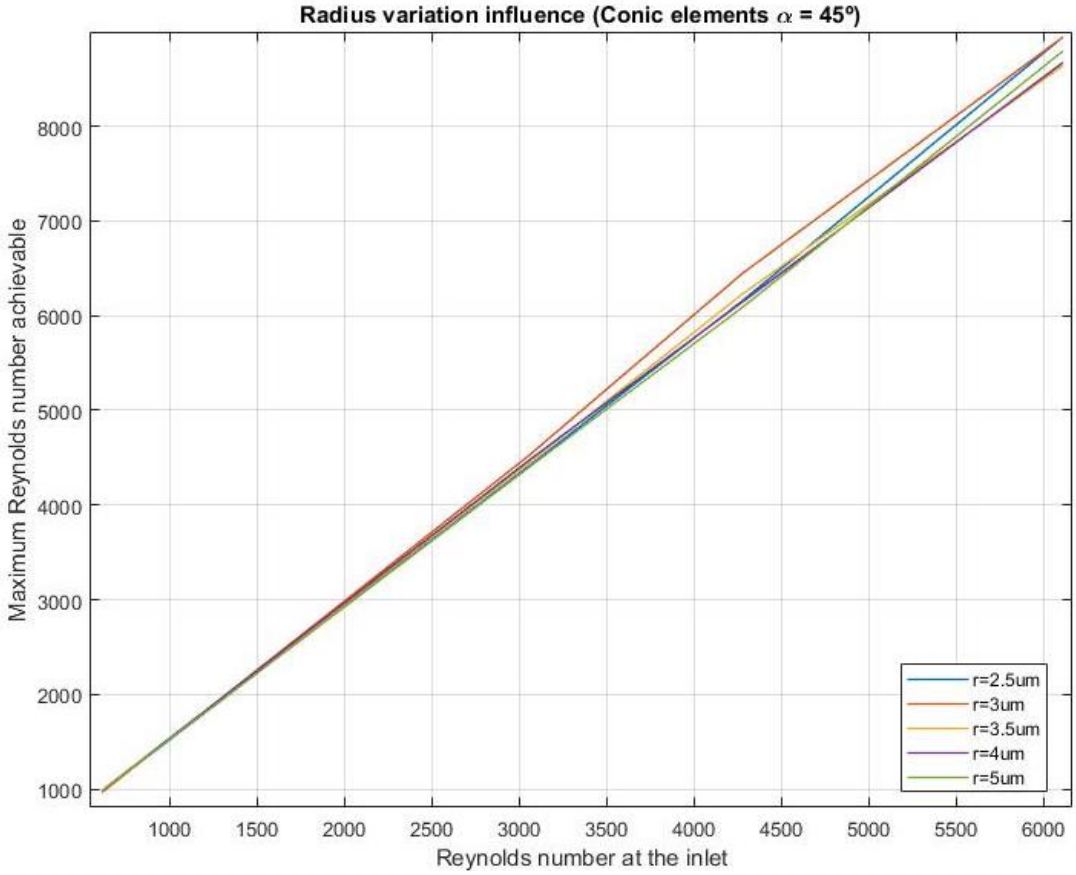

Figure 59. Radius influence on maximum Re for conic elements with α=45º

The general tendency might be that the best performance is obtained with larger elements imitating the roughness. However, it is remarkable the fact that, as the elements size is increased and since the weight is conserved, the number of elements must be decreased. From these results it can be stated that a large number of elements, even though the dimensions are smaller, is preferred rather than less element with larger sizes.

Finally, the last aim was to figure out which one was the preferred orientation. Using the previously selected roughness geometry two different simulations were performed. In one of them the rough side was facing the inlet and, in the other, the evaluated face faced the outlet.

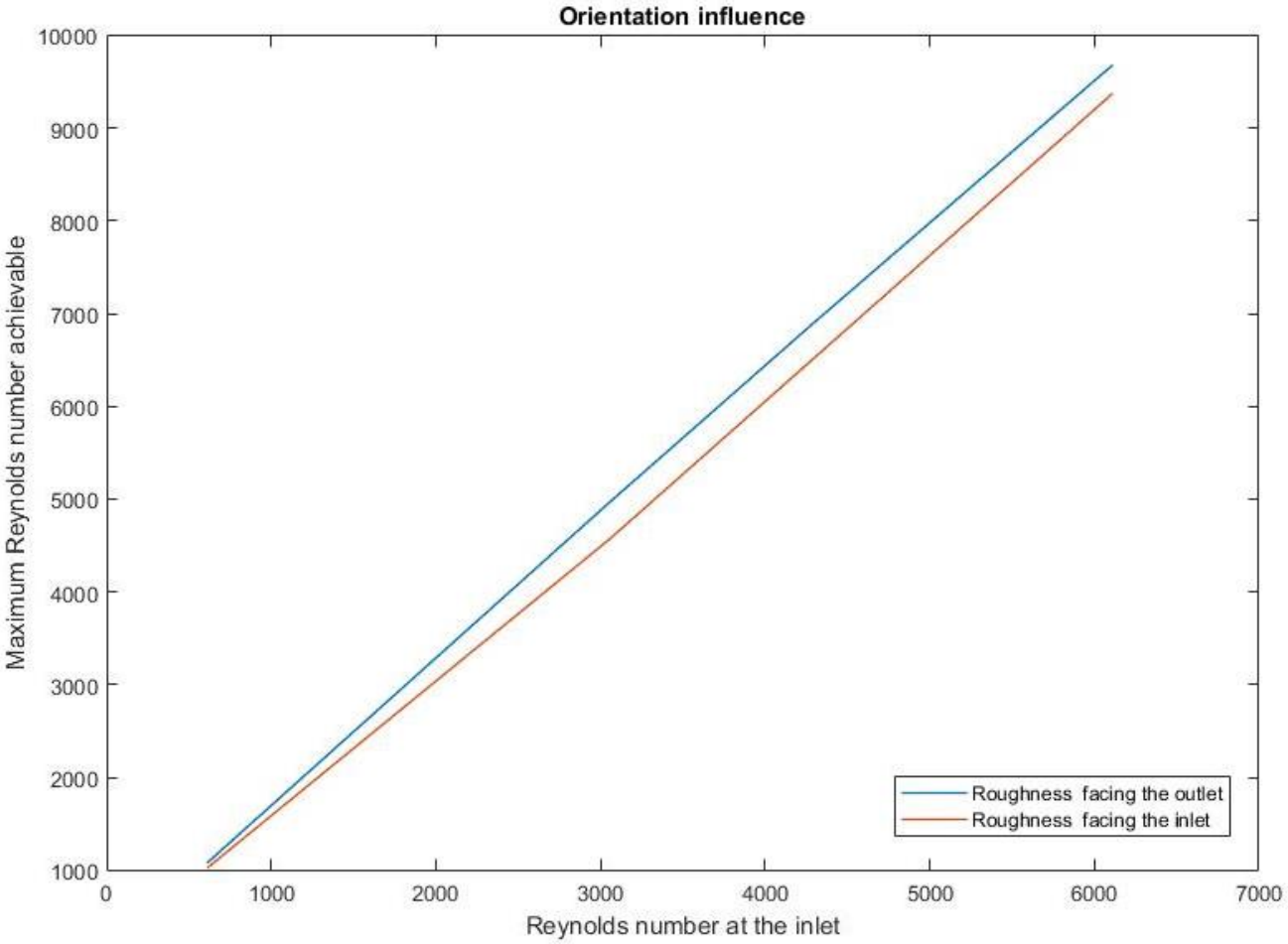

Figure 61. Roughness orientation influence.

Figure 61 displays the influence of the side in which the artificial roughness is located. It can be observed how the maximum achievable Re reached higher values when the roughness faced the outlet.

Summarizing, the most optimal arrangement for the microflap roughness is a set of 40 conical elements (with $\alpha=30^{o}$), with a radius of 2.1 μm and with the rough face facing the outlet.

4.2.3.2 Macroflap

The procedure followed for macroflap was exactly the same as in the preceding section. Different radius and altitudes were assessed for each of the elements' combinations.

The figures below display how every simulated radius affected the fluid performance. As in the microflap case, the best performance is obtained with lower radius.

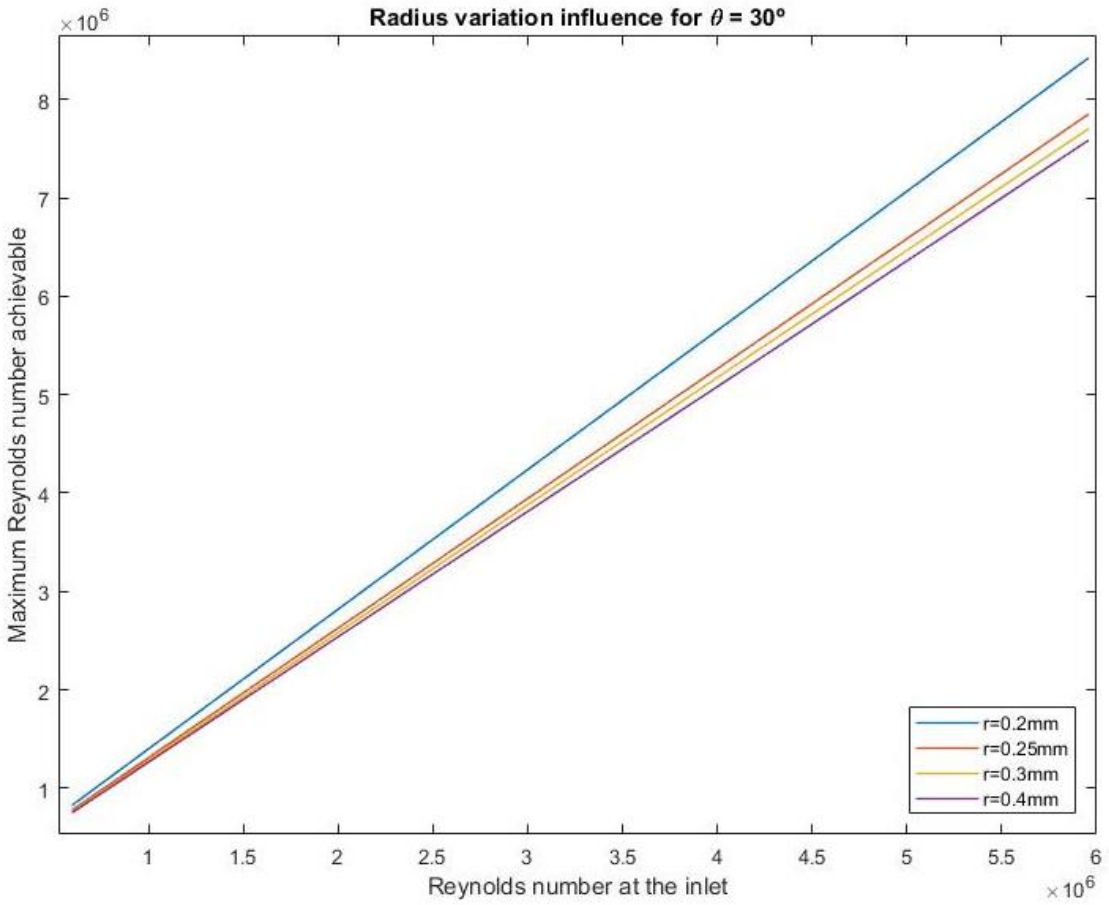

Figure 62. Radius influence on Re. Conic elements with α=30º

As it was previously mentioned, when increasing the radius (i.e. the size of every element), the number of elements has to be decreased in order to conserve the total weight. This may be one of the reasons why the efficiency is reduced while the elements size is enlarged.

The same results are obtained in figures 62, 63 and 64, the most optimal results are achieved with smallest radius.

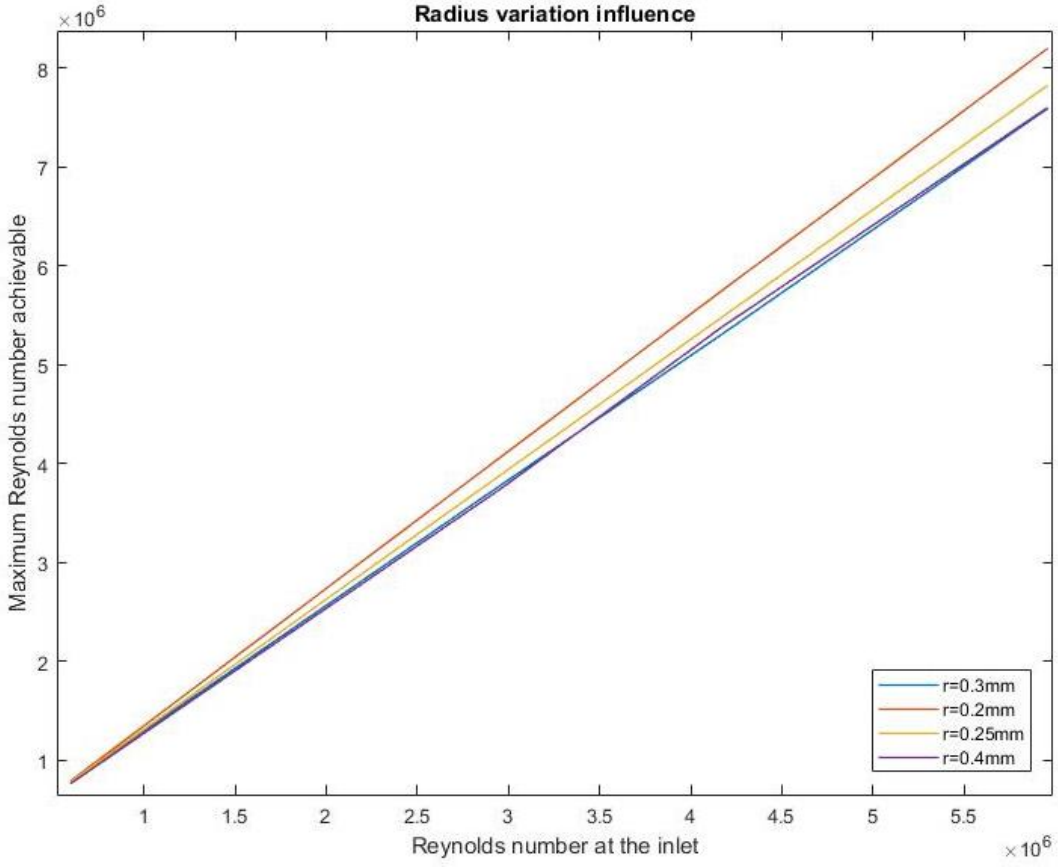

Figure 64. Radius influence on Re. Cylindrical elements

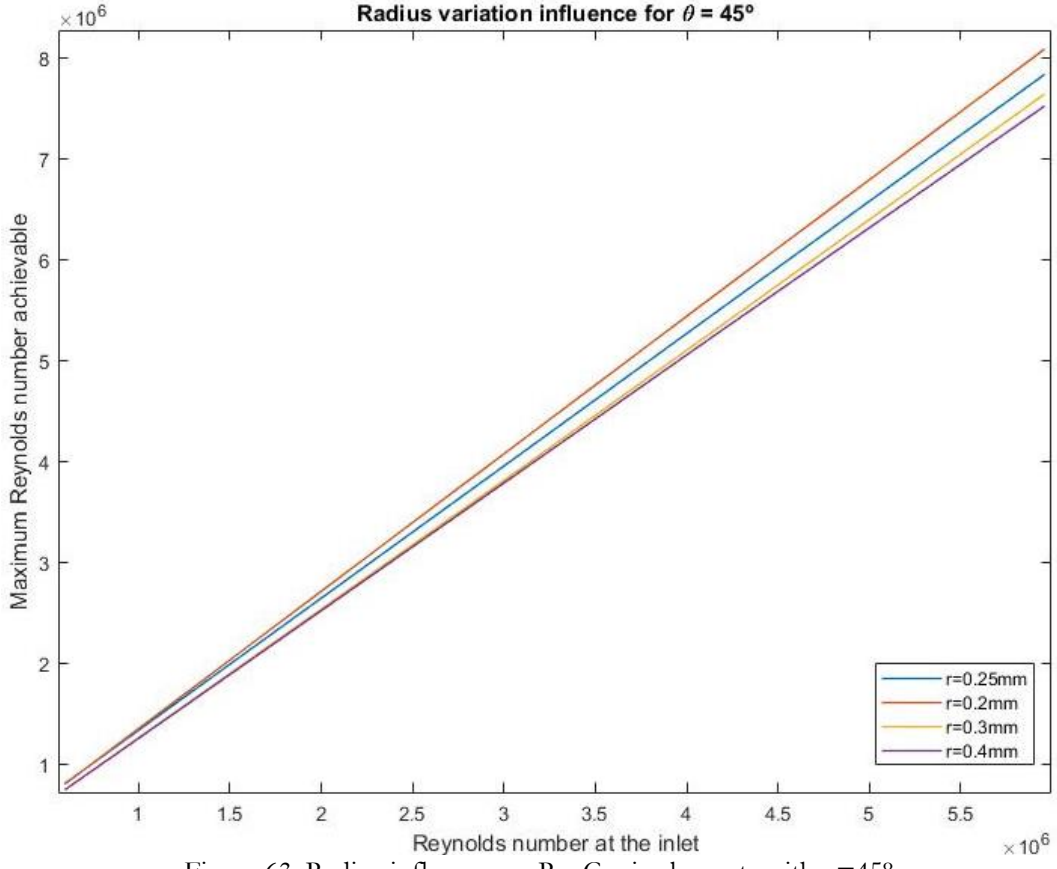

Figure 63. Radius influence on Re. Conic elements with α=45º

By comparing all the above graphs, it can be seen that the element geometry, together with its dimensions, which optimizes the fluid performance is the arrangement of conic elements with α=30º and a radius of 0.2mm.

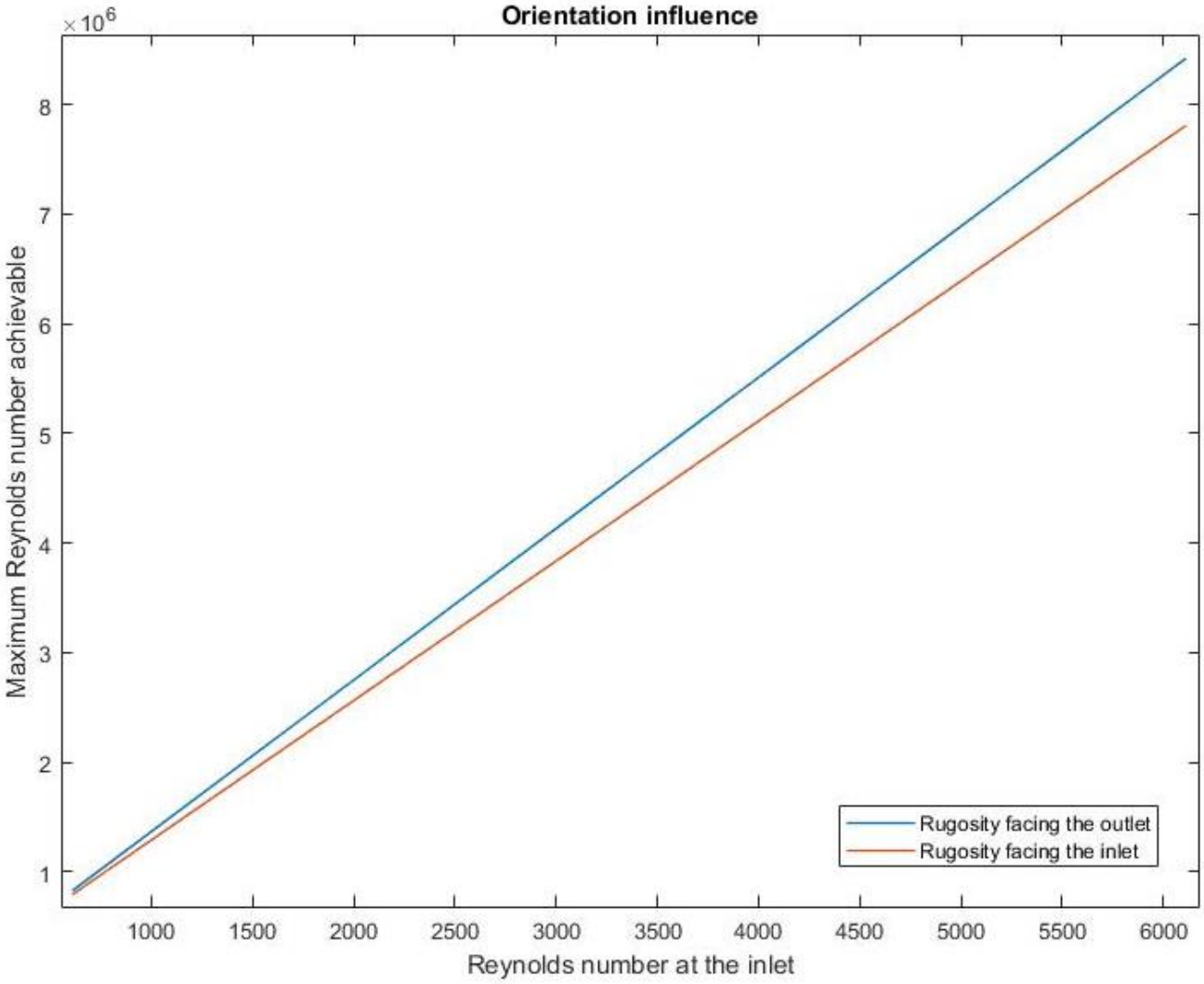

Figure 65. Roughness orientation influence.

This elements' set is used to evaluate which is the orientation of the roughness. Figure 65 shows the difference between facing the rough side to the input or to the output. As in the previous case, when the roughness is located on the rear side of the flap, higher Reynolds number are achieved.

Summing up, the best combination for the macroflap roughness is a set of 28 conical elements, with a radius of 0.2mm and with the rough face facing the outlet.

5. Conclusions

5.1 Micro

Figure below shows an overall comparison for the microflap (with and without roughness) and the column with the aim of having an overview of the micro filament shape and geometry that optimizes the performance. This graph (Figure 66) compares the best outcome obtained in each section. From it, it can be concluded that the most optimal configuration for this magnitude is a flap with dimensions 200x200x20 μm and with a rough face. The roughness is facing the outlet and it comprises 40 conical elements (with α=30º) with a radius of 2.1 μm.

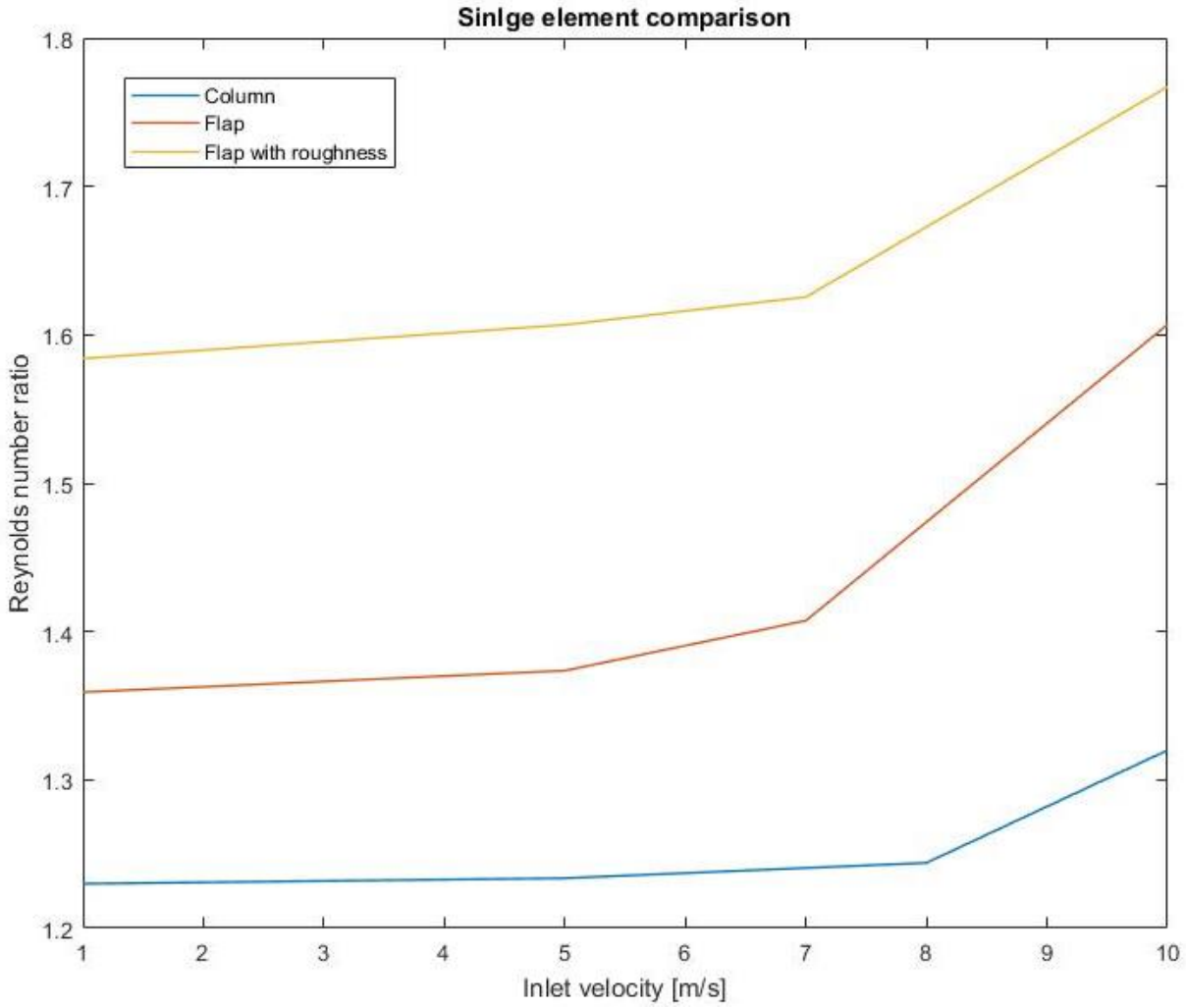

Figure 66. Re number vs inlet velocity. Final comparison for a single element.

The graph above only shows the result for a single element. As explained, the limitations of the academic version did not allow to add roughness in a set of element because it would exceed the maximum number of bodies.

Due to this fact, figure 67 displays a comparison between the most optimal set of columns and the most optimal set of flaps (without roughness) previously found.

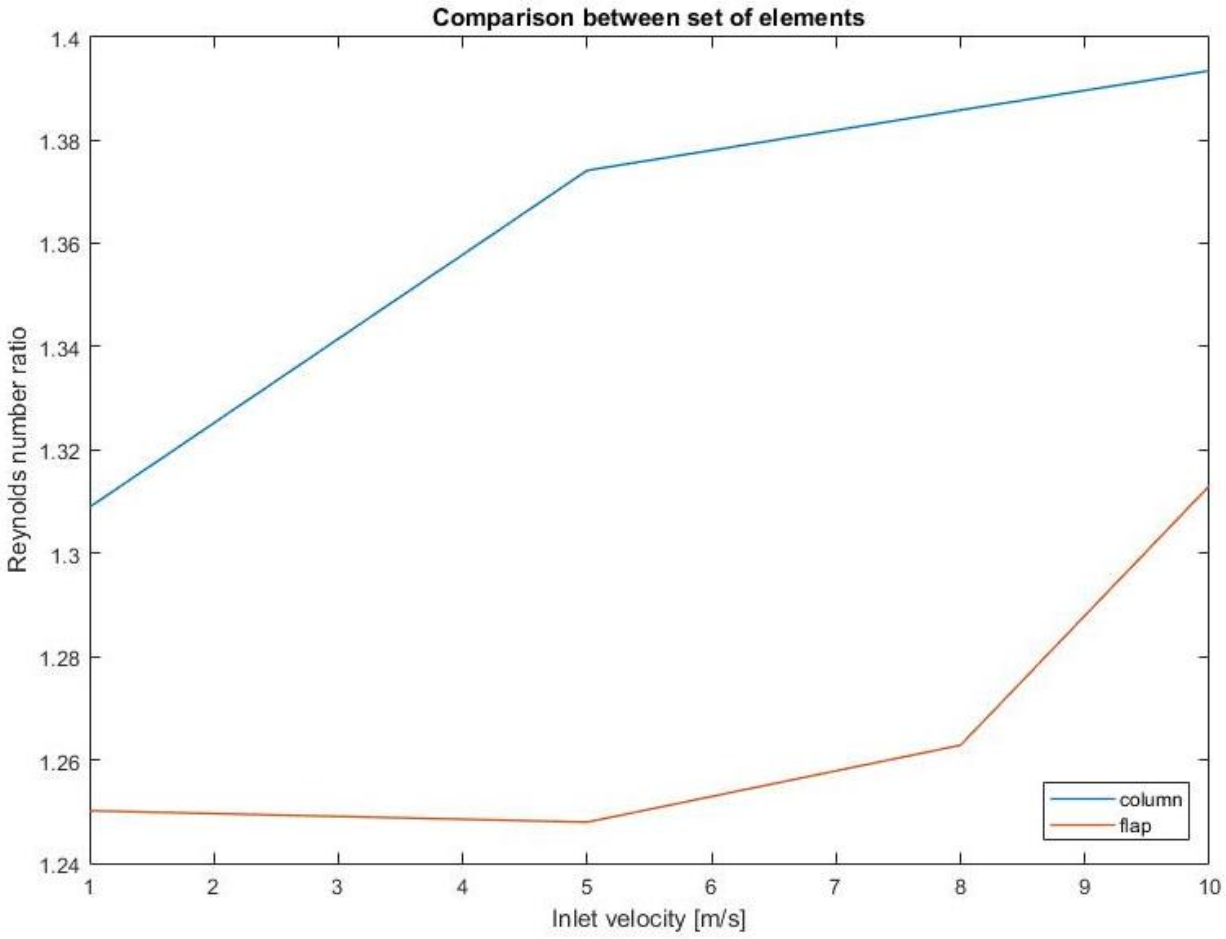

Figure 67. Re number vs inlet velocity. Final comparison for a set of elements.

Although flaps got better performances when dealing with a single element, when the set of elements are compared, the most optimal configuration is a group of nine columns. The crosswise separation between them is Sz=200um and the longitudinal distance is Sx=300um. This might happen due to the configuration of the space between elements. Flaps are wider and therefore, the separation between elements is larger. For both cases, in the result section, it was observed that the performance was increased as so did the separation between elements.

5.2 Macro

For this case columns were not analysed so the comparison is only among macroflaps. As it was shown along section 4.2, the performance of the flap was increased as so did the height and the width. However, the thickness was not an influent parameter since the outcomes did not change under its variation. The most optimal behaviour was achieved with a flap of 20mm width, a height of 10mm and a thickness of 1 mm. As stated, better performances are obtained when roughness is added so a rough face was included on the mentioned macroflap. The most optimal outcome was achieved with a rough face with 28 conical elements (radius of 0.2mm) facing the outlet.

Regarding the set of nine elements, the most optimal configuration was achieved with a longitudinal separation (Sx) of 10mm and a crosswise distance (Sz) of 10mm. In contrast to the previous case, the group performance was dropped as the separation between flaps increased.

6. Management

In this section it is included all the information related with the project organisation. It comprises the regulatory framework, the required budget, the project planning and future lines of study.

6.1 Legal

Regarding the legal framework, there were no many restrictions to take into account. Since it was a simulation procedure, there were no legal constrains or specific rules concerning its implementation or intellectual property.

The only applied legal issues are the licenses of the software that had been used along the whole procedure. However, the academic version was used. The academic version is free for any student from the university.

Regarding the information presented in section 3.2 about experimental results, this data was obtained from papers, articles and other sources of information. All the access to the original documents are included in the bibliography in order to respect the copyright. Copyright information regarding the Spanish legislation is included in the article 34 of the 'Real Decreto Legislativo 1/1996, de 12 de abril, por el que se aprueba el texto refundido de la Ley de Propiedad Intelectual, regularizando, aclarando y armonizando las disposiciones legales vigentes sobre la materia' published on the '«BOE» núm. 97, de 22 de abril de 1996, páginas 14369 a 14396 (28 págs.)'. [18]

6.2 Budget

The total cost of the project is mainly divided into direct and indirect cost. Direct costs comprise equipment costs, licenses, software, hardware and any overhead cost which can be directly attributed to the project. Indirect costs are those that cannot be directly accountable to specific cost objects such as telephone or internet expenses or any legal fees.

The following table summarizes and breaks down the costs of the project. Human resources are not applied for this case.

Author	Eva María Cancela Rodríguez			
Department	Bioengineering and aerospace department			
Project description				
Title	Fluidic simulation of a magneto-mechanical active surface			
Duration	6 months			
Direct costs				
Description	**Element**	**Cost (€)**	**Months used**	**Imputable cost (€)**
Hardware	Toshiba Satellite C55 (Core i5)	682	6	79.52
				79.52
Software	Matlab (academic license)	-	6	-
	Ansys (academic license)	-	6	-
	Windows 10 (operating system)	-	6	-
	Google Chrome (Browser)	-	6	-
	Firefox (Browser)	-	6	-
				0
Indirect costs				
Description	**Company**	**Cost (€)**	**Months used**	**Imputable cost (€)**
Internet	Vodafone	30€/month	6	180
				180
Total cost without IVA (€)				**259.52**
Total cost 21% IVA (€)				**314.0192**

Table 11. Budget.

Software total cost was 0€ due to the use of free software and academic licenses. Therefore, the total cost of the project is 314.02 €. This amount would be vastly increased in the case that the experiment was carried out also in the laboratory as it will be explained in section 6.4. In this case, material, salaries, and other measurement devices must be included.

Although along this project the analyses of the material behaviour under the influence of a magnetic field was not performed, this would be its main application. Future analyses to be executed under the influence of a magnetic are explained in the next section. This material could be implemented anywhere where the perfect mixture of two substances is required since, under the influence of a non-steady magnetic field, it would help in the process and

speed it up, as it was explained in the introduction. Another potential function would be its implementation in microchannel walls in order to accelerate the fluid flow.

Although it is already starting to be used on the development of lab-on-chip devices, where fluid need to be transported through microchannels, generalizing its use would have a big impact in many applications in terms of saving time and, therefore, money.

6.1 Planning

The planification of the project was constrained by the delivery dates stated by the university. In order to finish the proposed project within the due date, the planning shown on figure 68 was created.

As it can be seen, the simulation occupied most part of the time. The documentation process was carried out along the whole period, firstly starting with the introduction and the state of art and, once the outcomes had been obtained, with the results, discussions and conclusions. This planning is indicative since, due to lack of time, unexpected modifications and other issues, many adjustments were constantly being performed along the whole period.

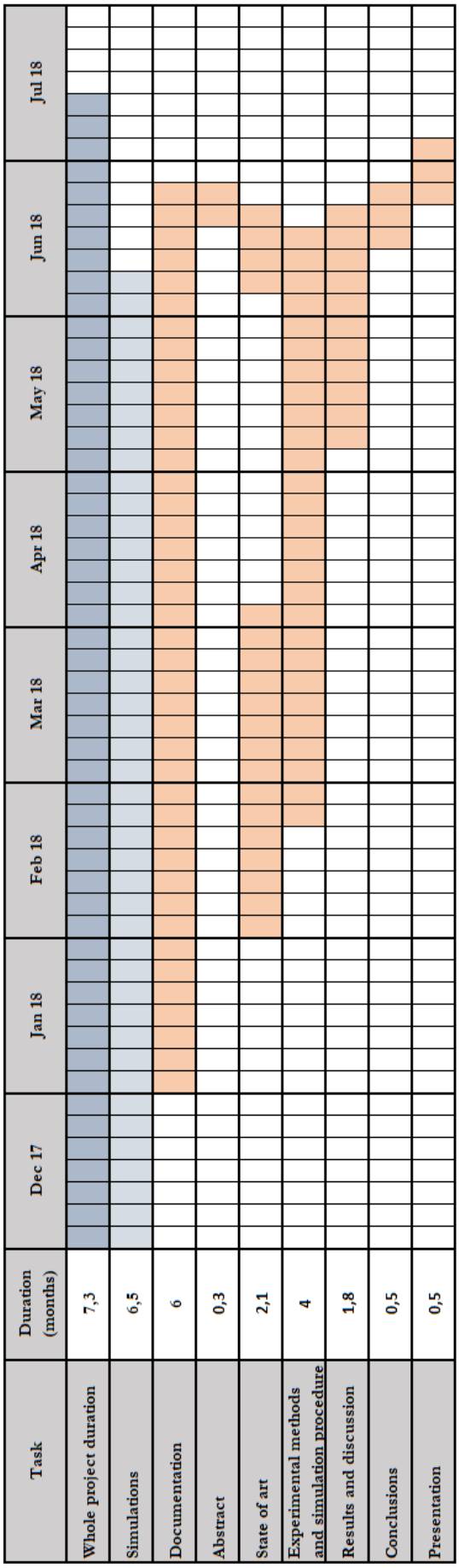

Figure 68. Project planning.

6.4 Future work

Comparison with experimental data has to be limited to the already published work, as it can be read in section 3.2. As future work remains the fabrication of microcilia by photolithography fabrication (figure 69) and the measurement of their performance inside of microfluidics channels. As first step, macrocilia, fabricated by pouring the nanocomposite mix into a mould (figure 70), would be used for the validation for simulation models. Once the validation is complete, a geometry for magnetic artificial cilia would be selected and it would be fabricated in the micrometre scale by means of the photolithography method.

Macro-scale simulations were designed to be used for comparison with the macrocilia (figure 70) inside of a glass channel. The channel would have a circular section with a flat base that allows to place the macroflap in the center. The fluid would be introduced through the inlet at a defined velocity while the outlet velocity would be measured in order to assess the fluid acceleration.

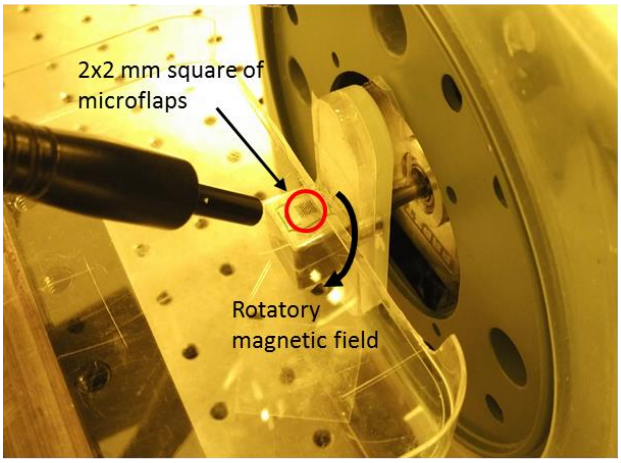

2x2 mm square of microflaps, 100 µm height, 20 µm thickness, 100 µm width.

	Design	Experimental
	[µm]	
Height	100	107.1 ± 3.5
Thickness	20	37.8 ± 3.2
Width	100	105.2 ± 3.0
Gap (S_y)	100	103.4 ± 3.4
Gap (S_x)	100	100.2 ± 4.5

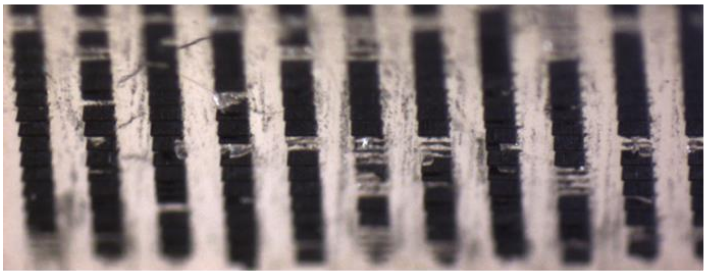

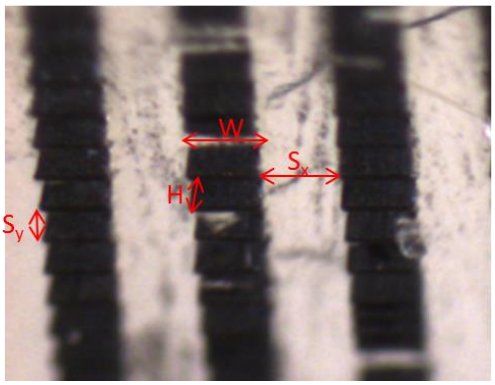

Figure 69.Magnetic microflaps fabricated by photolitography.

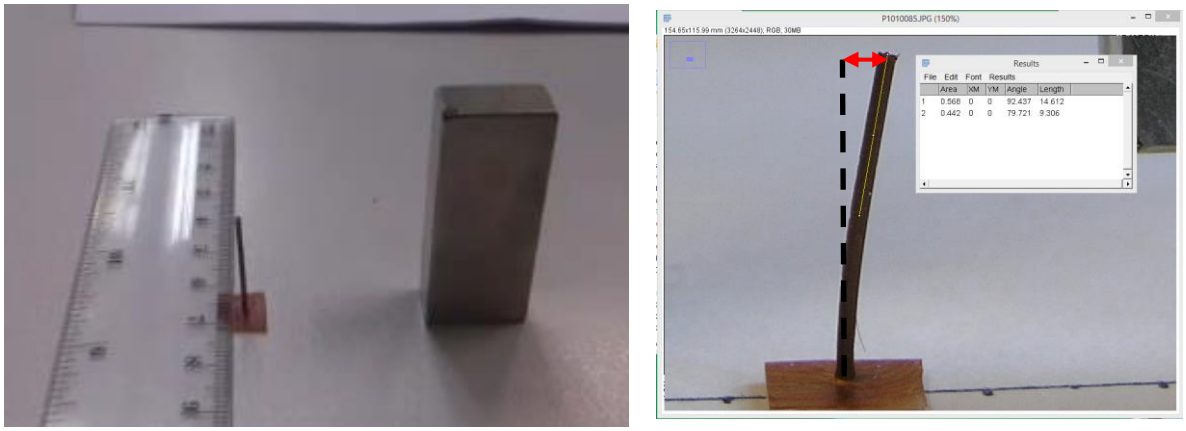

Figure 70.Magnetic macro columns fabricated by mould pouring.

The results from this experiment would judge the reliability of the all the accomplished simulations. In the probable case that the simulations were accurate enough, the simulation process vastly help in optimizing cost, time and resources. The most optimal configuration regarding the client requests would be previously virtually found and, afterwards, tested on the laboratory. Avoiding in this way unnecessary experiments. Obviously, including it in the project would increase the total cost on the previous section.

Another future line of improvement would be the use of a full version of the simulation software. Many limitations and restrictions were arisen during the whole project. Most of them could be avoided by using a full version and, without time constrains, many different new configurations and designs could be assessed.

As explained in section 3.2 and shown in [13], another way of amplifying the field of study would be to assess the orientation of the cilia columns inside the fluid.

The main proposed future line for this project would be to perform a 'system coupling' with the computational software Ansys. Two modules would be used (Fluent and Transient structural) in order to impose a magnetic field and see its influence of the cilia filament (filament deformation) and, simultaneously, the behaviour of the fluid due to this phenomena.

7. Bibliography

[1] "Paramecium: General Characters, Locomotion and nutrition " [Online]. Available: http://www.studyandscore.com/studymaterial-detail/paramecium-general-characters-locomotion-and-nutrition.

[2] Lodish H., Berk A., Zipursky SL, 'Section 19.4 Cilia and Flagella: Structure and Movement ', *Molecular Cell Biology. 4th edition., 2*000. [Online]. Available: https://www.ncbi.nlm.nih.gov/books/NBK21698/.

[3] "Biot Savart Law". [Online]. Available: https://en.wikipedia.org/wiki/Biot\OT1\textendashSavart_law.

[4] "Electromagnetism". [Online]. Available: https://es.wikipedia.org/wiki/Electromagnetismo.

[5] FEA Software. Mutliphysics Cyclopedia. [Online]. Available: «https://www.comsol.com/multiphysics/fea-software,» .

[6] FEM. Mutliphysics Cyclopedia. [Online]. Available: «https://www.comsol.com/multiphysics/finite-element-method,» .

[7] "Galerkin method," [Online]. Available: https://en.wikipedia.org/wiki/Galerkin_method.

[8] "Runge Kutta," [Online]. Available: https://es.wikipedia.org/wiki/M%C3%A9todo_de_Runge-Kutta.

[9] "The Origins of the Finite Element Method", 2013 [Online]. Available:https://www.colorado.edu/engineering/CAS/courses.d/IFEM.d/IFEM.AppO.d/IFEM.AppO.pdf.

[10] «FEM,» [En línea]. Available: https://wikivividly.com/wiki/Finite_element_method.

[11] Mark J, "Polymer Data Handbook", *Oxford Univ. Press, New York* , 1999. [Online]. Available: http://www.mit.edu/~6.777/matprops/pdms.htm.

[12] "Reynolds number," [Online]. Available: https://es.wikipedia.org/wiki/N%C3%BAmero_de_Reynolds.

[13] Xu S. J., Zhang W. G., Gan L., Li M. G., Zhou Y., " Experimental study of flow around polygon cylinders" *Journal of fluid mechanics,* 2017,812, pp. pp. 251-278.

[14] "Drag coefficient," [Online]. Available: https://en.wikipedia.org/wiki/Drag_coefficient.

[15] "Flow separation," [Online]. Available: https://en.wikipedia.org/wiki/Flow_separation.

[16] Silva G., Leal N, Semiao V., "Effect of wall roughness on fluid flow inside a microchannel", 14th *Int Symp on Applications of Laser Techniques to Fluid Mechanics*,2008.

[17] Taylor J. B, Carrano A. L, Kandlikar S. G., "Characterization of the effect of surface roughness and texture," *International Journal of Thermal Sciences 45 ,* 13 2 2006.

[18] Ministerio de cultura," I. Disposiciones generales", *BOE-A-1996-8930*, 1996, num. 97, pag from 14369 to 14396 [Online]. Available: https://www.boe.es/buscar/doc.php?id=BOE-A-1996-8930.

[19] "Stremlines and streaklines"[Online]. Available: https://en.wikipedia.org/wiki/Streamlines,_streaklines,_and_pathlines,.

[20] West J., "What Are the Main Functions of Cilia & Flagella?", *Sciencing*, 2018 [Online]. Available: https://sciencing.com/main-functions-cilia-flagella-10572.html,.

[21] "FEM", [Online]. Available: https://en.wikipedia.org/wiki/Finite_element_method,

[22] Onck R P., Den Toonder J. M. J., Artificial Cilia, *RSCPublishing*, 2013.

[23] Dai S. S., Younis B. A., Zhang H. Y., "Prediction of turbulent flow around a square cylinder with rounded corners," *Journal of Offshore Mechanics and Arctic Engineering,* 01 06 2017, 139(3).

[24] Wang C. Y., "Longitudinal flow past cylinders arranged in a triangular array", *Applied Mathematical Modelling,* 1999, volume 23, pages 219-230.

[25] Kundu P., Cohen I., Dowling D., *Fluid Mechanics 5th Edition,* 2011

[26] Nakayama Y., Boucher R. F.,*Introduction to Fluid Mechanics* , 2015